Numerical modeling of gas-particle flows inside fluidized beds

A Thesis Submitted to the
College of Graduate and Postdoctoral Studies
in Partial Fulfillment of the Requirements
for the degree of Doctor of Philosophy
in the Department of Mechanical Engineering
University of Saskatchewan
Saskatoon

By
Mohammad Reza Haghgoo

©Mohammad Reza Haghgoo, May, 2018. All rights reserved.

Permission to Use

In presenting this thesis in partial fulfilment of the requirements for a Postgraduate degree from the University of Saskatchewan, I agree that the Libraries of this University may make it freely available for inspection. I further agree that permission for copying of this thesis in any manner, in whole or in part, for scholarly purposes may be granted by the professor or professors who supervised my thesis work or, in their absence, by the Head of the Department or the Dean of the College in which my thesis work was done. It is understood that any copying or publication or use of this thesis or parts thereof for financial gain shall not be allowed without my written permission. It is also understood that due recognition shall be given to me and to the University of Saskatchewan in any scholarly use which may be made of any material in my thesis.

Requests for permission to copy or to make other use of material in this thesis in whole or in part should be addressed to:

Head of the Department of Mechanical Engineering
University of Saskatchewan
57 Campus Drive, Saskatoon, Saskatchewan S7N 5A9
Canada

OR

Dean
College of Graduate and Postdoctoral Studies
University of Saskatchewan
116 Thorvaldson Building, 110 Science Place
Saskatoon, Saskatchewan S7N 5C9
Canada

Abstract

Fluidized beds have widespread application in industry due to their increased rate of heat, mass, and momentum transfer. In order to effectively design fluidized beds at the industrial scale, it is essential to have an understanding of the complex hydrodynamic behavior of the dense gas-particle flows inside them. This thesis is focused on the bubbling fluidization of Geldart B particles. The Eulerian–Eulerian "Two-fluid model" (TFM) approach was used to simulate dense gas-particle flows inside two different three-dimensional (3D) bubbling beds. The numerical code Multiphase Flow with Interphase eXchanges (MFIX) was used to perform all the 3D simulations. The results were validated against published experimental data.

This manuscript-based thesis documents four different studies. The first study, Chapter 2, reports an in-depth investigation of two different models for the particle stress tensor in the elastic-inertial regime and assesses their ability to predict the hydrodynamics of a 3D cylindrical fluidized bed. Contours of inertial number, defined as the ratio of the inertial forces to the frictional forces, were used to visualize the flow properties. Analysis of the flow properties for a range of gas-particle regimes based on the inertial number enhances our insight into the flow behavior in such a complex system.

Chapter 3 reports a comprehensive study to assess the effect of three different particle-wall boundary conditions (BCs) on the structural features of a dense gas-particle flow inside a 3D thin bubbling bed. Accordingly, the effect of each wall model on the velocity field, 3D bubble statistics, gas-pressure fluctuations, and particle resolved-scale Reynolds stress were investigated. Also, the dominant mixing regions inside the bed were identified in order to quantitatively describe the bed performance.

Chapter 4 performs an in-depth systematic study that uses a particle energy budget analysis to investigate the dynamics of the bubbling bed discussed in Chapter 3. The budget analysis helps not only to quantify the relative importance of various terms contributing to the energy cascade, but also to identify the regions in the bed where most of the energy transfer takes place.

Chapter 5 applies state-of-the-art post-processing methodologies, namely, the Proper Orthogonal Decomposition (POD) and the swirling strength criterion to the fluctuating particle flow fields predicted by the TFM of a bubbling bed to identify and analyze the dominant spatio-temporal patterns of the particulate phase. The variation of the POD temporal coefficients associated with the particle volume fraction fluctuation field suggested the existence of a low-dimensional attractor and irregular periodicity in the flow. The particle vortical motions were characterized by their flat structure. POD was used to obtain a reduced-order reconstruction of the particle velocity and volume fraction fields using a subset of eigenmodes.

In summary, this thesis attempts to quantitatively describe some important features of bubbling beds dynamics that have received relatively little attention in the literature. To this end, it was observed that the use of inertial number, investigation of the energy cascade process, and studying particle vortical structures were helpful to quantitatively explore the underlying physics of bubbling beds. A major objective was also to identify a set of proper TFM parameters and particle-wall BC for high-fidelity simulation of bubbling beds.

Acknowledgements

First of all, I would like to thank my supervisors, Professor Bergstrom and Professor Spiteri, for all their wise guidance and mentorship. Their insights have helped shape my approach to challenges in research. I appreciate the time they spent to discuss the results of my research. Their deep knowledge has been pivotal in improving my understating of fluid mechanics through numerical modeling. I feel extremely fortunate to have had the opportunity to work with them and learn from their experiences.

It has also been a privilege to have an illustrious committee: Professor Bugg, Professor Noble, Professor Zhang, and Professor Szyszkowski. Their valuable comments helped me to improve the quality of my research work. I appreciate the help and support I receive from the faculty and staff at the Departments of Mechanical Engineering and Computer Science. Thank you to my good friends in the CFD and Numerical Simulation Laboratories. I also gratefully acknowledge the funding support of the Natural Sciences and Engineering Research Council (NSERC) of Canada.

None of this would have been possible without the unconditional support from my parents, Ahad and Rana and my sisters, Sanaz and Arezo. I understand that being apart from my family was truly difficult for all of us; more difficult for them than me. However, they have always been there to offer words of wisdom and support.

Finally, I would like to thank my wife, Maryam, for all her love and the motivation she brings to my life. You have supported me through thick and thin.

To my parents: *Ahad* and *Rana*,
and my wife: *Maryam*

Contents

List of Tables

List of Figures

Nomenclature

Ar	Archimedes number
E	energy
H_0	initial bed height
I_{2D}	second invariant of the deviator of the strain rate tensor
J	rate of dissipation of granular temperature per unit volume
N	frictional stress normal to the wall
P	pressure
Re	Reynolds number
$\mathcal{D}$	rate of dissipation of energy per unit area
$\mathcal{P}$	rate of production of energy per unit area
d	particle diameter
e	restitution coefficient
g_0	radial distribution function
q	granular energy flux
r	normalized slip velocity
t	time
u	velocity
x	position

Greek symbols

$\bar{\bar{\tau}}$	stress tensor
β	inter-phase momentum transfer coefficient
β_0	tangential restitution coefficient
Γ	production of granular temperature
κ	conductivity
λ_{ci}	imaginary part of the complex eigenvalue of the velocity gradient tensor
μ	friction coefficient
ϕ	specularity coefficient
ρ	density
θ	granular temperature
ε	volume fraction
φ	angle of internal friction

Subscripts and superscripts

min	minimum
c	collisional
$coll$	due to inelastic collisions
$drag$	due to drag
f	frictional
g	gas phase
h	internal
kc	kinetic-collisional
mf	minimum fluidization
p	particle phase
sl	slip at the wall
$slip$	due to slip velocity between phases
w	at the wall

List of Abbreviations

BC	Boundary Condition
CFB	Circulating Fluidized Bed
DIA	Digital Image Analysis
PIV	Particle Image Velocimetry
POD	Proper Orthogonal Decomposition
PSD	Power Spectral Density
ROM	Reduced-Order Model
SIMPLE	Semi-Implicit Method for Pressure Linked Equations
TFM	Two-Fluid Model
2D	Two Dimensional
3D	Three Dimensional

Chapter 1

Introduction

Fluidization refers to a process where solid particles are transformed into a fluid-like state through suspension in a gas (or liquid). This process, shown schematically in Figure 1.1, is initiated by the injection of a pressurized gas into a bed of particles. Figure 1.1 shows the variation of gas pressure drop (left vertical axis) and bed height (right vertical axis) with the superficial gas velocity. At low superficial gas velocities, i.e., lower than the velocity corresponding to point B in Figure 1.1, the pressure drop increases with the gas velocity to overcome the weight of the particles in the bed. The process from A to B is referred to as a fixed bed condition because the initial height of the bed remains unchanged. At point B, the intermeshed fixed-bed particles are unlocked and bed starts to expand. Point C corresponds to the condition where the drag force associated with the gas pressure drop counterbalances the apparent weight of the particles in the bed. The velocity corresponding to this point is referred to as the minimum fluidization velocity. By further increasing the superficial gas velocity the bed continues to expand, but the pressure drop remains approximately constant. Note that if the ABCD process is traced backward by gradually decreasing the superficial gas velocity, a new curve (DCA) is observed. This is due to the variation in the fixed-bed voidage.

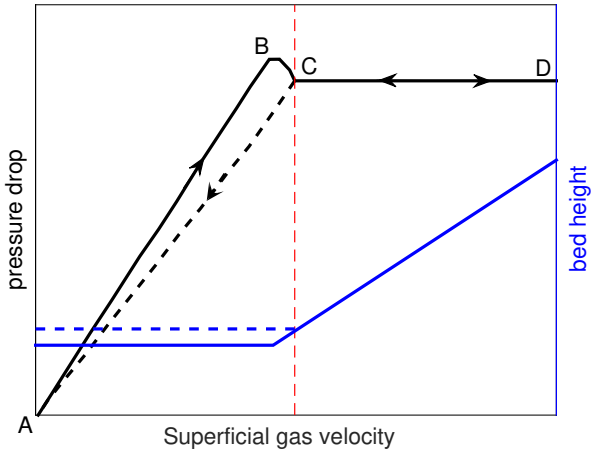

Figure 1.1: Variation of the gas pressure drop and bed height with the superficial gas velocity.

Geldart [3] classified the behavior of solid particles fluidized by gases into four clearly recognizable groups, characterized by the density difference $(\rho_p - \rho_g)$ and mean particle size. Here, ρ is the density and subscripts

p and g stand for the particle and gas phases, respectively. According to Geldart's classification, particles in group A exhibit dense phase expansion after minimum fluidization and prior to the bubble initiation. The group B particles give rise to bubble formation at the minimum fluidization. Group C contains extremely fine and mostly cohesive particles that are difficult to fluidize; and group D particles are characterized by their high density and can form stable spouted beds. Goossens [1] also distinguished different classes of fluidized particles based on the Archimedes (Ar) and Reynolds (Re) numbers:

$$Ar = \frac{d_p^3 \rho_g \left(\rho_p - \rho_g\right) g}{\mu_g^2}, \qquad Re = \frac{d_p \rho_g U}{\mu_g}, \tag{1.1}$$

where d, μ, U, and g (non-subscript) are the diameter, viscosity, superficial gas velocity, and gravitational acceleration, respectively. Figure 1.2 shows a general classification diagram plotted by Goossens [1], where he specified each type of Geldart group based on a range of Ar.

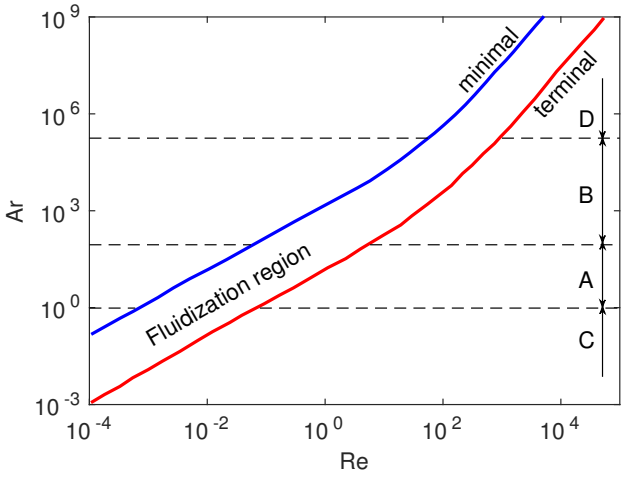

Figure 1.2: Classification diagram for fluidized particles [1].

Glicksman [4] determined the non-dimensional parameters governing the dynamics of fluidized beds, which include:

$$Ar,\ Re,\ Fr = \frac{U}{\sqrt{g d_p}},\ \frac{\beta d_p}{\rho_p U},\ \frac{\rho_p}{\rho_g},\ \frac{H_0}{D},\ \frac{D}{d_p}, \tag{1.2}$$

and particle size distribution and shape. Here Fr, β, H_0, and D indicate the Froude number, coefficient of the fluid-to-particle drag force per unit volume, initial height of the bed, and physical length-scale corresponding to the bed size, respectively. Following Goossens [1], Re can be empirically expressed as a function of Ar. Also, Glicksman et al. [5] indicated that Fr, and $\frac{\beta d_p}{\rho_p U}$ can be related to the other parameters for fluidization in air. Therefore, the governing non-dimensional parameters may be simplified to [5]:

$$Ar,\ \frac{\rho_p}{\rho_g},\ \frac{U}{U_{mf}},\ \frac{H_0}{D},\ \frac{D}{d_p}, \tag{1.3}$$

where U_{mf} refers to the minimum fluidization velocity. This thesis is focused on the bubbling fluidization of Geldart B particles, typically corresponding to $10^3 < Ar < 10^5$ and $2 < \frac{U}{U_{mf}} < 4$.

1.1 Motivation

Fluidized beds are widely employed in the petroleum, chemical, power-generation, and agricultural industries for processes involving drying, separation and mixing of particles, and chemical reactions [6]. Gas-particle fluidized beds have the distinct advantage of creating a highly suitable medium for heat and mass transfer and rapid mixing of particles. In order to effectively design fluidized beds at the industrial scale, it is essential to have an understanding of the complex hydrodynamic behavior of the dense gas-particle flows inside them. This understanding is achieved through theoretical and numerical models, and data collected from physical experiments.

In principle, the motion of an assembly of solid particles suspended in a fluid can be completely described by directly solving the Navier–Stokes equations for the interstitial fluid and Newton's equation of motion for each particle. These sets of equations are linked by the no-slip boundary condition between the solid and fluid on the surface of each particle. This fundamental level of description provides more information than is needed in practice. Moreover, this approach is computationally expensive for systems where a large number of particles is required, as for example in fluidized beds. Due to the difficulties associated with direct solutions, there have been various attempts to derive equations whose solutions determine the average properties of interest without resolving all details of the motion. In deriving these averaged equations, often referred to as the "two-fluid model" (TFM) formulation in the literature, Anderson and Jackson [7] used a weight function to calculate the spatial averages of the point variables over a spatial domain that is much smaller than the flow domain but larger than the particle spacing. In contrast, Ishii [8] used a phase indicator function and took the averages over a fixed volume. Using another approach, Drew [9] averaged at each point of space over an ensemble of macroscopically equivalent systems. Zhang and Prosperetti [10] also used an ensemble average method and derived a set of equations similar to that of [7]. We note that the basic assumption used to derive the averaged equations in the work of Anderson and Jackson, as stated above, is the condition of scale separation, i.e., the domain over which the average is taken is much larger than the size of a single particle but much smaller than the macroscopic length scale of the system. This implies that the shortest significant length scale of the motion that can be captured by this sort of averaging is larger than the particle spacing. Regardless of the method adopted for deriving the averaged equations, the process of averaging itself generates some undetermined terms, dependent on motions at the scale of the particles, that must be closed by specifying constitutive relations; specification of constitutive relations account for most of the differences between different theoretical approaches [11]. In this thesis, the Eulerian–Eulerian TFM, based on the locally averaged equations derived by Anderson and Jackson [7], is used to simulate dense gas-particle flows inside two different bubbling beds.

Overall, the TFM approach attempts to simplify the exact equations governing the dynamics of fluidized beds. However, there still exist complexity issues mostly in the details of particulate phase and related to the unsteadiness and challenging dynamics. These challenges are discussed in more detail in the following

section.

1.2 Challenges to numerical modeling of fluidized beds

The experimental study of inherently three-dimensional (3D) flows inside fluidized beds can be difficult and costly in terms of flow visualization and measurements. However, advanced computational models that provide realistic predictions of the gas-particle flows could be used to provide similar information. There are many published numerical and experimental studies of flows in dense fluidized beds; most of these are two-dimensional (2D) because they are less computationally expensive and simpler to perform [12]. Many researchers have simulated pseudo-2D fluidized beds, which have a small depth in comparison with their other dimensions, using 2D Cartesian coordinates [13, 14, 15]. However, several authors have reported significant discrepancies between experimentally measured particle velocities and their numerically predicted counterparts in 2D simulations [15, 16, 17]. In pseudo-2D systems, the particle movements are restricted by front and back walls, and the friction exerted by these walls can have a significant effect on the particles and the bubble rise velocity. Also, considerable flow disparities have been reported between 2D and 3D beds [18, 19]. Thus, using 2D simulations to predict the hydrodynamic behavior of fluidized beds is problematic.

One major challenge in performing high-fidelity simulations of the dynamics of fluidized beds, using the Eulerian–Eulerian approach, is deriving proper constitutive relations to close the governing equations. For example, in turbulent fluidized beds, where the interstitial fluid plays a significant role in the dynamics of the system, the major challenge is to model the complicated interaction of particles and the turbulence of the fluid. In such systems, the granular particles rarely reach a volume fraction $\varepsilon_p^{\min}$ where the friction between particles starts to play a role. Consequently, the particle stress tensor can be described by the kinetic theory of granular flows. However, in bubbling fluidized beds, where the turbulence of the fluid, if any, is damped by the inertia of the particles, not only does the particle volume fraction reach $\varepsilon_p^{\min}$, but it is also likely to exceed the packed bed limit, $\varepsilon_p^{\max}$. Therefore, in bubbling beds, in addition to the so-called rapid-flow regime, a quasi-static slow regime is likely to be present. Obviously, there are regions in the bed in which the granular flow undergoes a transitional intermediate regime that is neither rapid nor slow in nature. Accordingly, in modeling of bubbling beds, the main challenge is to have a comprehensive model that is able to distinguish the different behavior of the granular flow for each regime and appropriately describe the stresses.

Another challenge in realistic flow prediction of fluidized beds is specifying the appropriate particle-wall boundary condition. There are different particle-wall boundary conditions available in the literature to account for the particle slip velocity and the granular energy flux at the wall. However, it is not yet clear how these different wall boundary conditions affect the simulated flow behavior, nor is it clear which are the most realistic.

In order to be able to effectively design fluidized beds at the industrial scale, it is essential to have an understanding of the complex behavior of the gas-particle flows inside them. To gain deeper insight into

the complex dynamics of bubbling beds, it is helpful to perform a budget analysis on the particle energy equations, i.e., the fluctuating and mean kinetic energy equations, and visualize contours of different terms that appear in the energy equations. Note that less attention has been given to the investigation of energy cascade in a fluidized bed in the literature. Energy cascade, in this context, refers to energy exchange between various scales based on a variety of mechanisms. The energy budget analysis helps not only to quantify the relative importance of various terms contributing to the energy cascade but also to identify the regions in the bed where most of the energy cascade takes place.

Finally, most of the bubbling bed studies available in the literature have focused on the time-averaged features of the flow fields, whereas only a few studies have investigated the fluctuating flow fields. As a matter of fact, the particle flow fields inside bubbling beds exhibit unsteady structures accompanied by intense meso-scale fluctuations induced by the motion of the bubbles. Therefore, sophisticated post-processing methodologies are required to identify and analyze the dominant spatio-temporal patterns associated with the fluctuating fields. This will enable to quantitatively explore the significance of the fluctuating fields in the mixing dynamics of bubbling beds.

1.3 Objectives of the thesis

Considering the challenges recognized above, the present thesis has four objectives:

1. **A critical investigation of the closure relations:** Two different models for the particle stress tensor that use different constitutive equations in the elastic-inertial regime are examined to assess their ability to predict the dynamics of the bed. To understand how the particle stress models affect structural features of the flow, a quantitative analysis is performed on some important aspects of the mechanics of bubbling beds that have received relatively little attention in the literature. Accordingly, different flow regimes are identified in the context of fluidized beds through the dimensionless inertial number, and the main characteristics of each regime are discussed. In addition, the effects of the particle stress tensor on the bubble characteristics, natural frequency of the bed, and particle Reynolds stress are investigated.

2. **A comprehensive assessment of different particle-wall boundary conditions:** Three different particle-wall boundary conditions are examined to assess their ability to predict the dynamics of a dense gas-particle flow inside a three-dimensional bubbling bed, using the two-fluid model. The effect of each wall model on the velocity field, three-dimensional bubble statistics, gas-pressure fluctuations, and particle resolved-scale Reynolds stress are investigated. Also, the predicted dominant mixing regions inside the bed are identified and visualized in order to quantitatively describe the bed performance.

3. **Energy budget analysis:** An in-depth systematic study is performed that uses a particle energy budget analysis to examine the dynamics of a three-dimensional bubbling bed. The budget analysis

helps not only to quantify the relative importance of various terms contributing to the energy cascade but also to identify the regions in the bed where most of the energy cascade takes place.

4. **Identifying dominant spatio-temporal patterns and vortical structures:** State-of-the-art post-processing methodologies, namely the Proper Orthogonal Decomposition (POD) and the swirling strength criterion, are applied to the fluctuating particle flow fields predicted by the two-fluid model of a bubbling bed to identify and analyze the dominant spatio-temporal patterns of the particulate phase. The ability of the POD eigenmodes to reproduce the instantaneous fields is systematically assessed.

To achieve these objectives, the Eulerian–Eulerian TFM, based on the locally averaged equations derived by Anderson and Jackson [7], is used to simulate dense gas-particle flows inside two different 3D bubbling beds, namely a cylindrical, and a thin rectangular bubbling bed. The numerical code Multiphase Flow with Interphase eXchanges (MFIX) [11] is used to perform the simulations. Some additional FORTRAN subroutines are developed and integrated into the MFIX code to implement different particle-wall boundary conditions. The numerical model predicts such output properties as the particle volume fraction, gas pressure, the velocity components of each phase, and the granular temperature of the particle phase. Python subroutines are developed to post-process these properties and calculate spatially and time-averaged quantities of interest, such as the phasic velocity profiles, particle-flow patterns, 3D bubble characteristics, power spectral density of the gas pressure, and resolved-scale particle Reynolds stresses. Special Python subroutines are also developed to perform the energy budget analysis, POD analysis and to identify the particle vortex motions using the swirling strength method. Extensive 3D simulations are performed to obtain the model parameter values that compared most favorably with the experimental data. All simulations are performed in parallel using 60 cores on an architecture consisting of dual Hex Core Intel Xeon X5650 2.66 GHz with 12 GB of RAM each and running Red Hat Enterprise Linux Server 5.7.

This thesis adopts a manuscript-based format. In all studies reported in this thesis, the main author conducted the simulations, post-processed and analyzed the results, and prepared the first draft of each manuscript. He then worked with the co-authors to discuss the results and finalize the content and form of the manuscripts.

1.4 Structure of the thesis

The remainder of this manuscript-based thesis is structured into five chapters, as following.

Chapter 2 presents the numerical results of a dense gas-particle flow inside a cylindrical bubbling bed, where the effect of particle stress tensor on the flow behavior is assessed. The closure relations for a high fidelity simulation of bubbling beds are quantitatively explored. It starts with a literature review, followed by the governing/constitutive equations that are used throughout the thesis and an explanation of the simulation set-up. This study was published in "Particuology" in 2017 (Haghgoo et al.[20]).

In Chapter 3 the effect of different particle-wall boundary conditions on the simulation of a 3D thin bubbling bed is comprehensively investigated. It starts with a literature review, followed by the mathematical description of particle-wall boundary conditions, numerical methodology, grid study, and simulation set-up details. In this study, the boundary condition that produced most comparable results to the measured data was identified and used in the next two studies that make up the next two chapters of this thesis. This work was published in the "International Journal of Multiphase Flow" in 2017 (Haghgoo et al.[2]).

In Chapter 4 a particle energy budget analysis is performed to examine the dynamics of the same bed considered in Chapter 2. To this end, an equation for the kinetic energy of the mean particle flow is rigorously derived in the context of the TFM approach, and a particle energy budget analysis is performed. The physical implications of various terms in the energy equations are discussed, and their spatial distributions are plotted. A diagram is provided to summarize how the energy cascades in a dense gas-particle flow. The numerical simulation set-up and the values of physical parameters are discussed. In addition, the contribution of the wall to the energy cascade is quantitatively discussed. This study is still under review by the "Powder Technology"(Haghgoo et al.[21]).

Chapter 5 represents the application of the 3D POD technique to the particle flow fields predicted by a TFM of the same bed used in the previous two chapters to identify and analyze the dominant spatio-temporal patterns associated with the the meso-scale fluctuating particle flow fields. Also, the particle vortical structures in the bubbling bed are identified using a swirling strength criterion applied to the particle velocity gradient tensor. 3D POD is used to extract the dominant vortex motions and obtain a reduced-order reconstruction of the particle velocity and volume fraction fields using a subset of the energetic modes.

Note that these four chapters have strong ties with each other. Chapters 2 and 3 both attempt to determine a proper set of constitutive relations and boundary conditions necessary for high-fidelity simulation of fluidized beds. Based on the outcomes of these two chapters, a set of simulations was conducted, and the result was used to perform the energy budget and POD analyses presented in chapters 4 and 5. Overall, chapters 2 and 3 deal with the proper set of equations to build a realistic numerical model of bubbling beds, whereas chapters 4 and 5 utilize the results of this numerical model to throughly analyze the flow using state-of-the-art post-processing techniques.

Conclusions and recommendations for future extension are presented in Chapter 6.

Chapter 2

Effect of particle stress tensor in simulations of dense gas-particle flows in fluidized beds

A similar version of this chapter has been published as:

- M. R. Haghgoo, D. J. Bergstrom, and R. J. Spiteri. Effect of particle stress tensor in simulations of dense gas-particle flows in fluidized beds. *Particuology* 38 (2018) 31–43.

The first author conducted the simulations, post-processed and analyzed the results, and prepared the first draft of the manuscript. He then worked with the co-authors to discuss the results and finalize the content and form of the manuscript.

Preamble

The first step in a realistic "Two-fluid model" prediction of bubbling fluidized beds is to specify a proper set of constitutive relations to close the governing equations. It is well-established that in gas-particle bubbling beds, there exist three distinct flow regimes, namely, rapid-flow, transitional intermediate, and quasi-static slow regimes. In each of these specific regimes, the particle flow behaves differently, as does the particle stress dependency on its strain rate. Therefore, it is significant to understand how the particle stress models affect predicted features of the flow. To this end, a more in-depth study of two different models for the particle stress tensor in the transitional intermediate regime is conducted and their ability to predict the hydrodynamics of a 3D cylindrical fluidized bed is assessed.

A major contribution of this chapter is that different flow regimes are identified, in the context of fluidized beds, through the dimensionless inertial number, and the main characteristics of each regime are discussed. Analysis of the flow properties for a range of gas-particle regimes based on their inertial number enhances our understanding of the flow behavior in such a complex multiphase system. In addition, the effect of the particle stress tensor on bubble formation, bubble behavior, natural frequency of the bed, and particle Reynolds stress are investigated.

Abstract

A two-fluid model based on the kinetic theory of granular flow for the rapid-flow regime and the Coulomb friction law for the quasi-static regime is applied to predict the hydrodynamics of dense gas-particle flow in a three-dimensional fluidized bed. Two different models for the particle stress tensor that use different constitutive equations in the elastic-inertial regime are examined to assess their ability to predict the dynamics of the bed. To understand how the particle stress models affect structural features of the flow, a quantitative analysis is performed on some important aspects of the mechanics of bubbling beds that have received relatively little attention in the literature. Accordingly, different flow regimes are identified in the context of fluidized beds through the dimensionless inertial number, and the main characteristics of each regime are discussed. In addition, how the particle stress tensor manifests itself in the bubble characteristics, natural frequency of the bed, and particle Reynolds stress are investigated, all of which help to better understand the complex dynamics of the fluidized bed. The numerical results are validated against published experimental data and demonstrate the significant role of the stress tensor in the elastic-inertial regime.

2.1 Introduction

Successful prediction of the hydrodynamics of fluidized beds requires accurate modeling of particulate stress terms in the momentum equation. It is generally accepted to apply the kinetic theory of granular flow to model the kinetic-collisional stresses in dilute regions, corresponding to the rapid-flow regime, where the streaming of the individual particles and binary collisions between them are the dominant mechanisms of momentum transport, see e.g., Lun et al. [22], Savage [23] and van Wachem et al. [24]. However, there is no general consensus in modeling the frictional stresses in dense regions where there is sustained contact between particles. In their model, Johnson and Jackson [25] assumed that the total stresses acting on the particle phase are the sum of the kinetic stresses and the frictional stresses. Although the validity of this assumption is not assured, it is capable of capturing the two extrema of granular flows, i.e., viscous flow and plastic flow [26]. Syamlal et al. [11] proposed a model, referred to as the Schaeffer model, in which the effects of the frictional stresses are activated only at particle volume fractions higher than $\varepsilon_p^{\max}$, corresponding to the quasi-static slow regime. For frictional stresses, following Schaeffer [27], they assumed that the shear stress is proportional to the normal stress. In this model, there is a sharp transition between the rapid-flow and quasi-static regimes that could result in erroneous bubble shape and bed expansion [28]. Using the additive approach of Johnson and Jackson [25], Srivastava and Sundaresan [26] proposed another model for the particulate phase stresses, referred to as the Princeton model. In this model, the frictional stress is added to the kinetic-collisional stress tensor in the intermediate regime, referred to as the elastic-inertial regime [29]. In this model, the frictional stresses affect the granular flow at a minimum frictional particle volume fraction $\varepsilon_p^{\min}$.

Although there are other frictional stress models available, e.g., see Schneiderbauer et al. [30], the most pervasive ones for the simulation of bubbling beds are the Schaeffer and Princeton models. Therefore, it is relevant to determine which of these two models is more realistic, and this in turn requires a detailed knowledge of how these models affect the simulated flow structure of the gas-particle flows. These models have already been the subject of several studies that assessed their ability to predict the overall behavior of fluidized beds, e.g., see Benyahia [31], Passalacqua and Marmo [32], Reuge et al. [33], and Verma et al. [34]. Passalacqua and Marmo [32] performed a comparison of the frictional stress models applied to a two-dimensional (2D) fluidized bed and used the mean bubble diameter to interpret their numerical results. Reuge et al. [33] studied the effects of dissipation parameters on the dynamics of the bed with a focus on the bed expansion ratio and its fluctuation. Although these are undoubtedly useful parameters in the study of fluidized beds, the flow patterns were not discussed. In a more comprehensive study, Verma et al. [34] investigated the effect of several parameters on the numerical simulation of a three-dimensional (3D) bubbling fluidized bed and demonstrated the significance of the frictional models. Most of studies have only focused on a comparison of the model results. Relatively few studies have investigated how the particle stress models affect structural features such as flow regimes, flow patterns, velocity profiles, and bubble formation; such studies would advance our understanding of the complex behavior of these multiphase flows.

This paper reports a more in-depth study of two different models for the particle stress tensor in the elastic-inertial regime and assesses their ability to predict the hydrodynamics of a 3D cylindrical fluidized bed. A major objective is to gain insight into how these models modify the simulated flow structure. The paper attempts to quantitatively describe some important features of the mechanics of the bubbling/slugging beds that have received relatively little attention in the literature. To that end, different flow regimes are identified, in the context of fluidized beds, through the dimensionless inertial number, and the main characteristics of each regime are discussed. To the best of authors' knowledge, it is the first time that contours of inertial number are used to visualize the flow properties. Analysis of the flow properties for a range of gas-particle regimes based on their inertial number enhances our understanding of the flow behavior in such a complex multiphase system. In addition, the effect of the particle stress tensor on bubble formation, bubble behavior, natural frequency of the bed, and particle Reynolds stress are investigated. The numerical code Multiphase Flow with Interphase eXchanges (MFIX) is used to perform the simulations (Syamlal et al. [11]), using the Eulerian–Eulerian framework. The results are validated against published experimental data by Laverman et al. [35].

2.2 Mathematical modeling

The Eulerian–Eulerian two-fluid model, based on the locally averaged equations derived by Anderson and Jackson [7], is used to simulate an isothermal gas-particle system.

The governing equations, for phases m, m' (where $m, m' = g, p$ for gas or particles, respectively, and

$m \neq m'$), are conservation of mass

$$\frac{\partial\left(\varepsilon_m \rho_m\right)}{\partial t}+\frac{\partial\left(\varepsilon_m \rho_m u_{mi}\right)}{\partial x_i}=0, \tag{2.1}$$

and conservation of momentum

$$\frac{\partial\left(\varepsilon_m \rho_m u_{mi}\right)}{\partial t}+\frac{\partial\left(\varepsilon_m \rho_m u_{mj} u_{mi}\right)}{\partial x_j}=-\varepsilon_m \frac{\partial P_g}{\partial x_i}+\frac{\partial \tau_{mij}}{\partial x_j}-\gamma_m \frac{\partial P_p}{\partial x_i}+\beta\left(u_{m'i}-u_{mi}\right)+\varepsilon_m \rho_m g_i, \tag{2.2}$$

where $\gamma_m = 1$ if and only if $m = p$; otherwise, $\gamma_m = 0$. The gas phase (air) is modeled as an ideal gas so that ρ_g is calculated from P_g. Here ρ, ε, $\mathbf{u}$, P, $\overline{\overline{\tau}}$, β, and (non-subscript) g represent the density, volume fraction, velocity vector, pressure, stress tensor, inter-phase momentum transfer coefficient, and gravitational acceleration, respectively. Noting that $\varepsilon_p + \varepsilon_g = 1$, only ε_p is treated as an independent variable. The interfacial drag coefficient β is defined by

$$\beta = 18\varepsilon_g \varepsilon_p \mu \frac{F(\varepsilon_p, Re)}{d_p^2}, \tag{2.3}$$

where $F(\varepsilon_p, Re)$ and d_p are the dimensionless drag force and particle diameter, respectively, and μ is the gas viscosity. In this study, the drag force proposed by Beetstra et al. [36] is used; it is defined as

$$F(\varepsilon_p, Re)=\frac{10\varepsilon_p}{\left(1-\varepsilon_p\right)^2}+\left(1-\varepsilon_p\right)^2\left(1+1.5\sqrt{\varepsilon_p}\right)+\frac{0.413Re}{24\left(1-\varepsilon_p\right)^2}\times\left[\frac{\left(1-\varepsilon_p\right)^{-1}+3\varepsilon_p\left(1-\varepsilon_p\right)+8.4Re^{-0.343}}{1+10^{3\varepsilon_p}Re^{-(1+4\varepsilon_p)/2}}\right], \tag{2.4}$$

where $Re = d_p|\mathbf{u}_g - \mathbf{u}_p|\rho_g \varepsilon_g/\mu$ represents the particle Reynolds number.

To close Eq. 2.2 for the particle phase, an expression for the stress tensor is required. Following Johnson and Jackson [25], the particle stress tensor is assumed to be the sum of the kinetic-collisional stresses and the frictional stresses; i.e.,

$$\tau_{pij} = \tau_{pij}^{kc} + \tau_{pij}^{f}, \tag{2.5}$$

where the kinetic-collisional stress tensor, commonly modeled by the kinetic theory of granular flow, is given by

$$\tau_{pij}^{kc} = \left(\eta\mu_b \frac{\partial u_{pi}}{\partial x_i}\right)\delta_{ij} + 2\mu_p S_{pij}, \tag{2.6}$$

and the frictional stress tensor is given by

$$\tau_{pij}^{f} = 2\mu_f S_{pij}, \tag{2.7}$$

where δ_{ij} is the Kronecker delta,

$$\delta_{ij}=\begin{cases}1, & i=j,\\ 0, & \text{otherwise},\end{cases} \tag{2.8}$$

and the quantity η is defined by

$$\eta = \frac{1+e}{2}, \tag{2.9}$$

where e is the particle-particle coefficient of restitution. In this study, the value of e is 0.86.

The bulk viscosity is given by [22],

$$\mu_b = \frac{256}{5\pi}\mu' \varepsilon_p^2 g_0, \tag{2.10}$$

where

$$\mu' = \frac{5}{96}\rho_p d_p \sqrt{\pi \Theta_p}, \tag{2.11}$$

and g_0 is the radial distribution function taking into account the probability of collision of the particles.

The particle strain-rate tensor is given by

$$S_{pij} = \frac{1}{2}\left(\frac{\partial u_{pi}}{\partial x_j} + \frac{\partial u_{pj}}{\partial x_i}\right) - \frac{1}{3}\frac{\partial u_{pi}}{\partial x_i}. \tag{2.12}$$

Lun et al. [22] also proposed an expression for the particle viscosity. However, they did not consider the effect of the interstitial fluid. Following Ma and Ahmadi [37], the particle viscosity, in which the interstitial fluid effect is included, is given by

$$\mu_p = \left(\frac{2+\alpha}{3}\right)\left[\frac{\mu_p^*}{g_0\eta(2-\eta)}\left(1 + \frac{8}{5}\eta\varepsilon_p g_0\right)\left(1 + \frac{8}{5}\eta\left(3\eta - 2\right)\varepsilon_p g_0\right) + \frac{3}{5}\eta\mu_b\right], \tag{2.13}$$

with

$$\mu_p^* = \frac{\rho_p \varepsilon_p g_0 \Theta_p \mu'}{\rho_p \varepsilon_p g_0 \Theta_p + (2\beta\mu'/\rho_p\varepsilon_p)}, \tag{2.14}$$

where α is a dimensionless constant equal to 1.6 [25].

In Eq. 2.2, the particle pressure is given by

$$P_p = P_p^{kc} + P_f, \tag{2.15}$$

where, following Lun et al. [22], $P_p^{kc} = \varepsilon_p \rho_s \Theta_p [1 + 4\eta\varepsilon_p g_0]$ and P_f is the frictional pressure for the particle phase.

In these equations, Θ_p is the granular temperature, which is calculated by solving the granular energy transport equation,

$$\frac{3}{2}\varepsilon_p\rho_p\left[\frac{\partial\Theta_p}{\partial t} + u_{pj}\frac{\partial\Theta_p}{\partial x_j}\right] = \frac{\partial}{\partial x_i}\left(\kappa_p\frac{\partial\Theta_p}{\partial x_i}\right) - P_p^{kc}\frac{\partial u_{pi}}{\partial x_i} + \tau_{pij}^{kc}\frac{\partial u_{pi}}{\partial x_j} + \Pi_p - \varepsilon_p\rho_p J_p. \tag{2.16}$$

The first term on the right-hand side of Eq. 2.16 represents the conductive transport of the particle fluctuation energy. The particle conductivity of the granular energy, κ_p, is given by [22],

$$\kappa_p = \left(\frac{\kappa_p^*}{g_0}\right)\left[\left(1 + \frac{12}{5}\eta^2\left(4\eta - 3\right)\varepsilon_p g_0\right)\left(1 + \frac{12}{5}\eta\varepsilon_p g_0\right) + \frac{64}{25\pi}\left(41 - 33\eta\right)\eta^2\left(\varepsilon_p g_0\right)^2\right], \tag{2.17}$$

where

$$\kappa_p^* = \frac{\rho_p \varepsilon_p g_0 \Theta_p \kappa}{\rho_p \varepsilon_p g_0 \Theta_p + \left(\dfrac{6\beta\kappa}{5\rho_p\varepsilon_p}\right)} \tag{2.18}$$

and

$$\kappa = \frac{75\rho_p d_p\sqrt{\pi\Theta_p}}{48\eta\left(41 - 33\eta\right)}. \tag{2.19}$$

The second term on the right-hand side of Eq. 2.16 models the production of kinetic fluctuation energy by the particle stress tensor. The forth term is the exchange of fluctuation energy due to interphase momentum transport and is given by [11]

$$\Pi_p = -3\beta\Theta_p + \frac{81\varepsilon_p\mu_g^2|\mathbf{u}_g - \mathbf{u}_p|^2}{g_0 d_p^3 \rho_p \sqrt{\pi\Theta_p}}. \tag{2.20}$$

Unfortunately, there is no consensus on the form of this term in literature [38]. The final term in Eq. 2.16 is the dissipation of granular energy due to inelastic particle-particle interaction [22],

$$J_p = \frac{48}{\sqrt{\pi}}\eta\left(1-\eta\right)\frac{\varepsilon_p g_0}{d_p}\Theta_p^{3/2}. \tag{2.21}$$

For the dense regions of the bed where particles are flowing slowly with extended contact and hence frictional stresses are dominant, there are different approaches to calculate the frictional stress tensor. Syamlal et al. [11] proposed that frictional stresses need to be considered only for regions where the solid volume fraction is higher than the maximum packing limit, $\varepsilon_p^{\max}$. In this model, referred to as the Schaeffer model, the frictional parameters are expressed as

$$P_f = \begin{cases} 10^{25}\left(\varepsilon_p - \varepsilon_p^{\max}\right)^{10}, & \varepsilon_p > \varepsilon_p^{\max}, \\ 0, & \varepsilon_p \leq \varepsilon_p^{\max}, \end{cases} \tag{2.22}$$

$$\mu_f = \begin{cases} \dfrac{P_f \sin(\varphi)}{2\sqrt{\mathbf{I}_{2D}}}, & \varepsilon_p > \varepsilon_p^{\max}, \\ 0, & \varepsilon_p \leq \varepsilon_p^{\max}, \end{cases} \tag{2.23}$$

where $\mathbf{I}_{2D}$ represents the second invariant of the deviator of the strain rate tensor and φ is the angle of internal friction, taken to be 28 degrees, in agreement with Ocone et al. [39]. Srivastava and Sundaresan [26] proposed a particulate stress model to account for the strain rate fluctuations. This model, which has its roots in the model proposed by Schaeffer [27], is referred to as the Princeton model in the literature [11]. In this model, the frictional stresses affect the granular flow at a minimum frictional solid volume fraction $\varepsilon_p^{\min}$. The frictional pressure for the particle phase is given by

$$\frac{P_f}{P_c} = \left(1 - \frac{\nabla\cdot\mathbf{u}_p}{n\sqrt{2}\sin(\varphi)\sqrt{S_p : S_p + \Theta_p/d_p^2}}\right)^{n-1}, \tag{2.24}$$

where : indicates the scalar invariant of the tensor product and the critical state pressure is given by

$$P_c = \begin{cases} 10^{25}\left(\varepsilon_p - \varepsilon_p^{\max}\right)^{10}, & \varepsilon_p > \varepsilon_p^{\max}, \\ Fr\dfrac{\left(\varepsilon_p - \varepsilon_p^{\min}\right)^r}{\left(\varepsilon_p^{\max} - \varepsilon_p\right)^s}, & \varepsilon_p^{\min} \leq \varepsilon_p < \varepsilon_p^{\max}, \\ 0, & \varepsilon_p \leq \varepsilon_p^{\min}, \end{cases} \tag{2.25}$$

where the values for the empirical constants are chosen according to Ocone et al. [39], namely, $Fr = 0.05$ [N.m^{-2}], $r = 2$, $\varepsilon_p^{\min} = 0.5$, and $s = 3$. In this model, the frictional viscosity is expressed as

$$\mu_f = \frac{\sqrt{2}P_f\sin(\varphi)}{2\sqrt{S_p : S_p + \Theta_p/d_p^2}}\left\{n - (n-1)\left(\frac{P_f}{P_c}\right)^{1/(n-1)}\right\}. \tag{2.26}$$

The value of the coefficient n depends on whether the solid phase is undergoing dilatation or compaction; i.e.,

$$n = \begin{cases} \dfrac{\sqrt{3}}{2\sin(\varphi)}, & \nabla \cdot \mathbf{u}_p \geq 0, \\ 1.03, & \nabla \cdot \mathbf{u}_p < 0. \end{cases} \tag{2.27}$$

Note that both the Princeton and Schaeffer models use the same granular rheology for the rapid and slow regimes.

Following Rangarajan et al. [40], Passalacqua and Fox [41], Vikas et al. [42], and Huilin et al. [43], the radial distribution function derived by Carnahan and Starling [44] is used in the simulations,

$$g_0 = \frac{1 - 0.5\varepsilon_p}{(1-\varepsilon_p)^3}. \tag{2.28}$$

Its application is physically justified because in the vicinity of the packed bed region the flow behavior is dominated by friction, and it is the frictional pressure, Eqs. 2.22 and 2.25, that diverges for the closed packed regions and ensures an infinite particle pressure.

In the present study, the wall boundary conditions are those from Johnson and Jackson [25]; partial slip model for the particle phase and no-slip for the gas phase. With these boundary conditions, the particle-wall slip velocity, $\mathbf{u}_{sl}$, and granular energy at the wall can be expressed as

$$\frac{\mathbf{u}_{sl}.(\overline{\overline{\sigma}}_p).\hat{n}}{|\mathbf{u}_{sl}|} + \frac{\phi_w \pi \rho_p \varepsilon_p g_0 \sqrt{\Theta_p} |\mathbf{u}_{sl}|}{2\sqrt{3}\varepsilon_p^{\max}} + N_f \tan(\varphi_w) = 0 \tag{2.29}$$

and

$$\kappa_p \frac{\partial \Theta_p}{\partial \hat{n}} = \frac{\phi_w \pi |\mathbf{u}_{sl}|^2 \rho_p \varepsilon_p g_0 \sqrt{\Theta_p}}{2\sqrt{3}\varepsilon_p^{\max}} - \frac{\sqrt{3}\pi \rho_p \varepsilon_p g_0 (1-e_w^2)\sqrt{\Theta_p}}{4\varepsilon_p^{\max}} \Theta_p, \tag{2.30}$$

where $\hat{n}$, ϕ_w, and e_w are the normal direction to the wall surface, specularity coefficient at the wall, and particle-wall restitution coefficient, respectively. It has been reported that e_w plays a minor role in the overall performance of a fluidized bed, whereas ϕ_w is believed to be of significant importance in numerical simulation of fluidized beds [45, 46, 47]. Following Li and Benyahia [48], the values of ϕ_w and e_w are taken to be 0.5 and 1.0, respectively. In Eq. 2.29, $\overline{\overline{\sigma}}_p$ is the total particle stress tensor defined by, $\sigma_{pij} = -P_p\delta_{ij} + \tau_{pij}$. Also, N_f, is the component of frictional stress normal to the wall surface, and φ_w is the angle of internal friction for particles sliding over the wall. Note that in this study the governing equations are discretized and solved in a cylindrical coordinate system. Therefore, an axis boundary condition (at $r = 0$) is required. A free slip boundary condition, i.e., zero gradient, for the azimuthal and axial velocity components and a vanishing radial velocity component at the centerline were used in this study. Detailed discussion on the centerline boundary conditions can be found in [34].

2.3 Numerical methodology

The computational domain was taken to be a cylindrical fluidized bed. The height of the bed was 160 cm with an initial particle bed height of 45 cm. The diameter of the cylinder was 30.6 cm. The numerical code MFIX,

a set of open-source FORTRAN subroutines, was used to perform the simulations. The numerical results of this study have been compared with the experimental measurements of Laverman et al. [35]. Table 2.1 shows the simulation parameters based on the experimental set-up.

Table 2.1: Simulation parameters for comparison with experimental study.

Particle type	Glass
Particle diameter, d_p	0.5 mm
Particle density, ρ_p	2500 kg m^{-3}
Minimum fluidization velocity, u_{mf}	0.18 m s^{-1}
Superficial gas velocity, $u_{z,0}$	$3.5u_{mf}$

To produce realistic flow patterns in an efficient manner, the higher-order Superbee scheme was used as the spatial discretization scheme [49]. To enhance numerical stability, a deferred correction scheme was implemented. The time discretization was the backward Euler method with a variable time step [11]. The numerical technique is based on a modified SIMPLE algorithm for multiphase flows to solve the pressure and volume fraction correction equations [11]. All simulations were performed in parallel using 60 cores on an architecture consisting of dual Hex Core Intel Xeon X5650 2.66 GHz with 12 GB of RAM each and running Red Hat Enterprise Linux Server 5.7. The first 10 seconds of the fluidization process were simulated. The simulations using the Schaeffer and Princeton models required approximately 504 and 336 hours, respectively.

2.4 Results and discussion

It is reported that a grid-independent simulation requires a typical resolution of no lower than approximately 10 times the particle diameter (d_p) [50, 51]. Agrawal et al. [52], Andrews et al. [53], and Igci et al. [54] performed "highly resolved" simulations of a flow in a small periodic domain and found that a grid size of $8.3d_p$ was sufficient to capture all the spatiotemporal structures that they needed to develop sub-grid scale models. Wang [55] and [56] studied a 2D bed using a grid size of 7 and $8.3d_p$, respectively, to perform a "high-resolution Eulerian simulation".

Given the current state of the art described above, in this study, a grid of 45×470×30 cells was used in the radial, axial, and azimuthal directions, respectively. This resolution, which was approximately $6.8d_p$, was found sufficient to capture the meso-scale structures, without any sub-grid scale model, and qualitatively reflected the experimental data. We note that further refinement of the grid size led to convergence issues and required time steps on the order of 10^{-7} s, which in turn, resulted in unacceptably long run times.

2.4.1 Effects of the stress models on the bed dynamics

In order to assess the validity of the two-fluid model, the numerical results were compared with the experimental measurements of Laverman et al. [35]. To calculate the azimuthally and time-averaged axial velocity,

the following calculation was performed [34]:

$$u_{z,p}^{\text{avg}} = \frac{\overline{\langle \varepsilon_p u_{z,p} \rangle}}{\overline{\langle \varepsilon_p \rangle}},$$

where $\langle \cdot \rangle$ and $\bar{\cdot}$ indicate azimuthal-averaging and time-averaging, respectively. The variables were time-averaged over the 10 seconds of the simulation after the first second so as to minimize any transient start-up effects.

Figure 2.1 presents the azimuthally and time-averaged axial velocity profile for the particles at three different heights. This figure shows the experimental data of Laverman et al. [35] and the numerical results of 3D simulations using both the the Schaeffer and Princeton stress models. At the height of 11 cm (Figure 2.1a), the results using the Schaeffer model are in poor agreement with the measured data compared with the results using the Princeton model. At the height of 21 cm (Figure 2.1b), the results using the Schaeffer model disagree with the experimental data in the region near the center by predicting a downward particle flow. At the height of 31 cm (Figure 2.1c), in contrast to both the experimental data and results predicted by the Princeton model, the Schaeffer model predicts a local maximum and minimum near the center. Note that the larger discrepancy in the velocity profile in the central region at the height of 31 cm should not be entirely attributed to the local dynamics of the bed at that location. Instead, it also depends on the predicted behavior of the bed in the lower region. For example, it is suggested that the formation of larger-structure bubbles at the higher heights is due to the coalescence of small bubbles being formed near the inlet. Therefore, the formation frequency of small bubbles near the inlet can have a significant effect on the velocity profile at higher heights. Also note that reducing the effect of friction, by increasing $\varepsilon_p^{\min}$ from 0.5 to 0.6, did not improve the velocity profile in the central region at the height of 31 cm.

To understand the differences between the results predicted by each model, it is helpful to look at the overall averaged-velocity distribution inside the bed. Figure 2.2 shows the azimuthally and time-averaged particle flow structure from experimental observation and as predicted by both stress models. The circulation pattern is mainly governed by the interaction of the moving bubbles with the particulate phase, giving rise to the formation of two main vortices above each other in the bed. Recall from Figure 2.1, near the bottom of the bed, i.e., at a height of 11 cm, there is an overall downward flow of the particles near the center and a small upward flow in the near-wall region. The particle flow behavior near the top, i.e., at a height of 31 cm, is opposite with upward flow near the center and downward flow near the wall. This contrasting behavior is explained by the formation of the two main vortices of opposite sign. It appears that the lower vortex predicted by the Schaeffer model, Figure 2.2b, is more extended than the experimental observation, resulting in a different flow pattern in the region between the two vortices. Therefore, it seems that the differences between the numerical results in Figure 2.1 are due to the extent of the lower vortex predicted by each model. Accordingly, it is appropriate to explore the mechanism that results in one vortex being more extensive than the other. After examining several factors, it was determined that the extent of the lower vortex is mainly governed by the inertia of the particles and the friction between them. The dimensionless

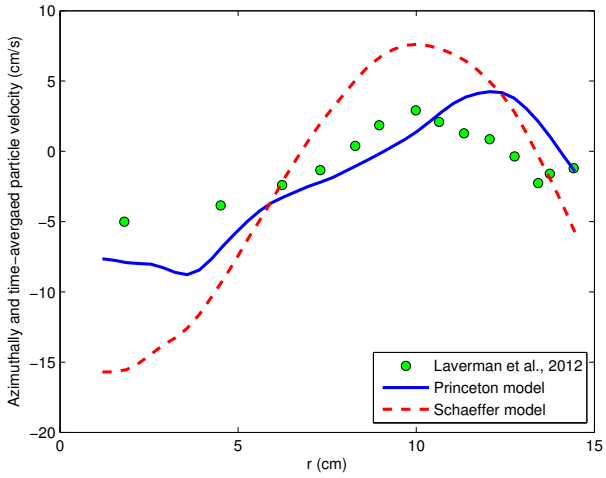

(a) $z = 11$ cm.

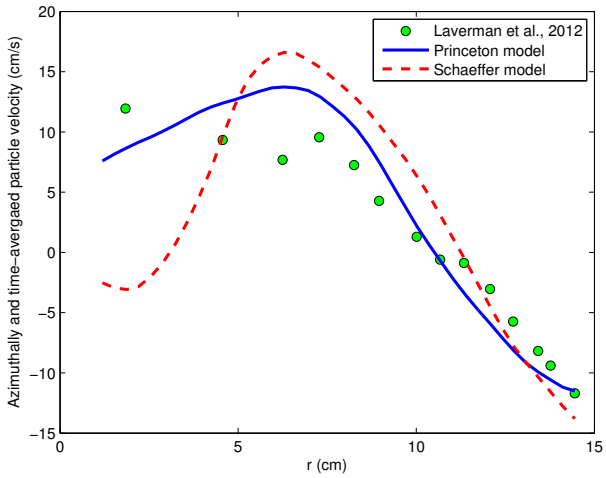

(b) $z = 21$ cm.

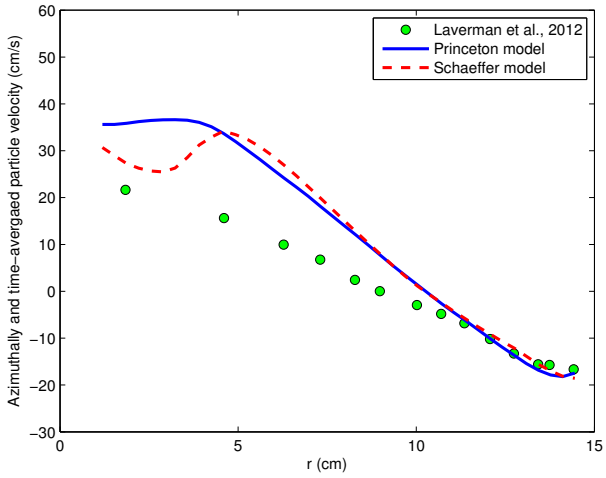

(c) $z = 31$ cm.

Figure 2.1: Radial profiles of azimuthally and time-averaged axial particle-velocity profiles at three different heights.

inertial number, $I = |\dot{\gamma}_p| d_p / \sqrt{P_p / \rho_p}$, is defined to be the ratio of the inertial forces to the frictional forces [57]. Here, $|\dot{\gamma}_p|$ is the second invariant of the deviator of the particle strain rate tensor. Figure 2.3 shows the azimuthally and time-averaged inertial number predicted by each stress model. For clarity, only the values between $2.0 \leq I \leq 6.0$ and $0.1 \leq I \leq 0.7$ are plotted for the Schaeffer and Princeton models, respectively. Comparing Figures 2.2 and 2.3 reveals that for the circulation pattern predicted by the Schaeffer model, Figure 2.2b, the inertial number for the upward particle stream of the lower vortex in the region near the wall, i.e., $z = 2$ to 15 cm and $r \geq 10$ cm, is greater than unity and an order of magnitude greater than its corresponding value for the same region as predicted by using the Princeton model. This indicates that for this region, the upward stream of particles predicted by the Schaeffer model has higher inertia and is less affected by friction, which in turn tends to elongate the lower vortex, whereas in the corresponding stream of particles predicted by the Princeton model the inertia of the particles is damped by the inter-particle friction and hence the vortex remains more compact. The reason that the Schaeffer model predicts regions with higher inertia is discussed shortly. We recall from Figure 2.1a that the results from the Schaeffer model show a stronger downward flow in the region near the center that can be attributed to the predicted high inertia of the particles and the fact that the overall momentum transport mechanism is due to the streaming of the individual particles and instantaneous collisions between them. On the other hand, the Princeton model improves the prediction of the averaged velocity by considering the inter-particle friction as a momentum transport mechanism in addition to the kinetic and collisional parts. In summary, the discrepancy in the results predicted by the Schaeffer model in Figure 2.1b is due to the predicted size of the lower vortex. After examining various terms in the momentum equation, it was found that the strong unrealistic inflection of the averaged axial velocity predicted by the Schaeffer model, as shown in Figure 2.1c, can be attributed to the extent of the lower vortex.

From Figure 2.2, the Schaeffer and Princeton models also predict different flow patterns for the region above the upper principal vortex. In order to estimate the significance of this difference in flow pattern on the bed operation, it is helpful to consider the azimuthally and time-averaged particle volume fraction contours. As shown in Figure 2.4, the region above the upper principal vortex is a dilute region with a particle volume fraction less than 0.1. Consequently, the different flow structures predicted by the Schaeffer and Princeton models for this region may not have a significant effect on the overall operation of the bed due to the fact that, on average, there are relatively few particles in this region. Figure 2.4 also shows that the region near the wall, up to $z = 45$ cm, and near the center, up to $z = 20$ cm, are the densest regions of the bed. The formation of these high-density regions at these relative locations may be considered as a typical characteristic of bubbling fluidized beds.

Note the experimental data of Laverman et al. [35], that is used to validate the numerical results, did not provide any information about the gas holdup. Therefore, to assess the validity of the current computational model in predicting the gas holdup, another case-study is considered. In this case-study a gas-particle fluidized bed that was experimentally studied by Taghipour et al. [58] is numerically simulated. Figure 2.5 shows,

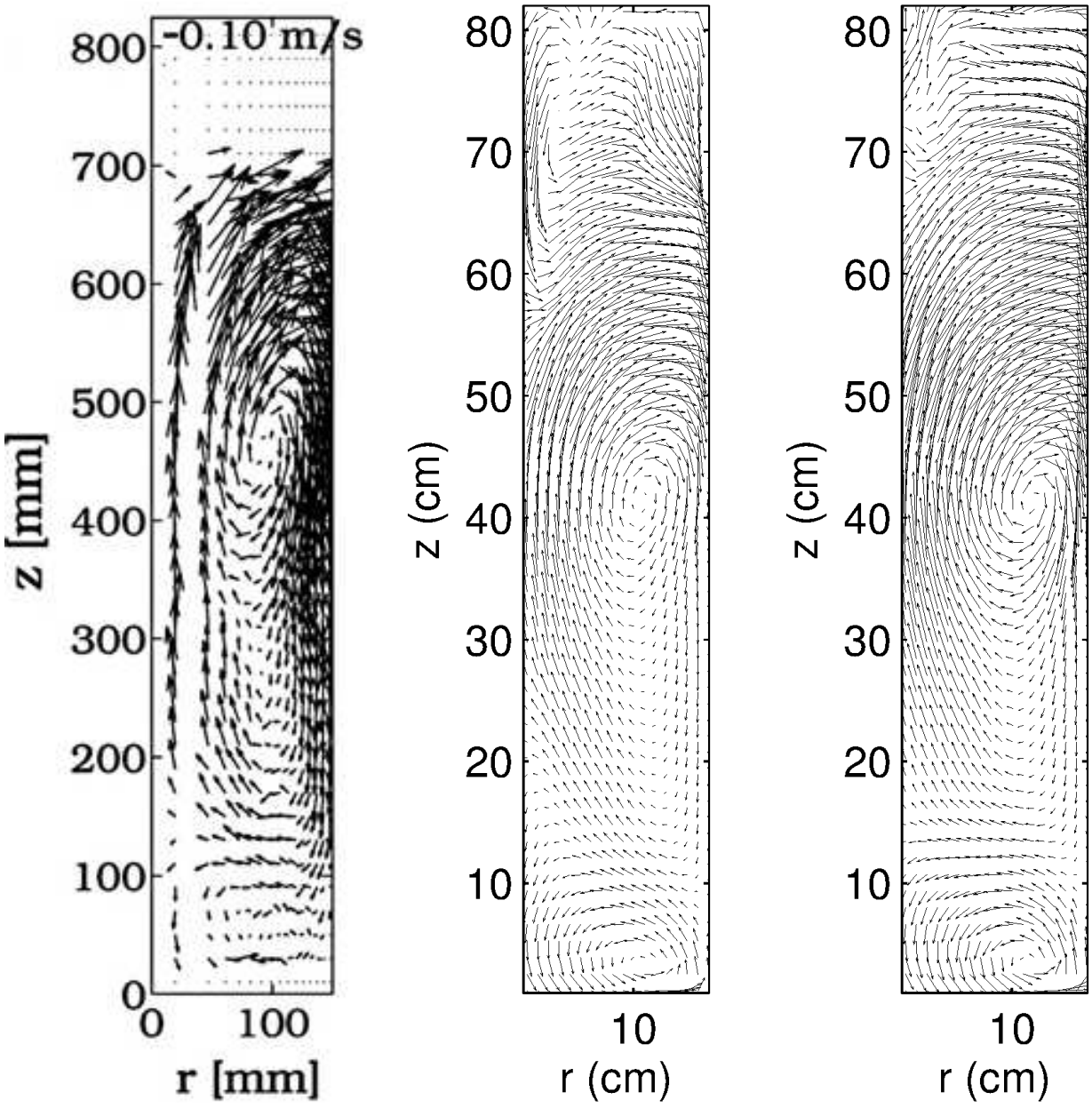

(a) Laverman et al. [35]. **(b)** Schaeffer model. **(c)** Princeton model.

Figure 2.2: Azimuthally and time-averaged particle flow structure.

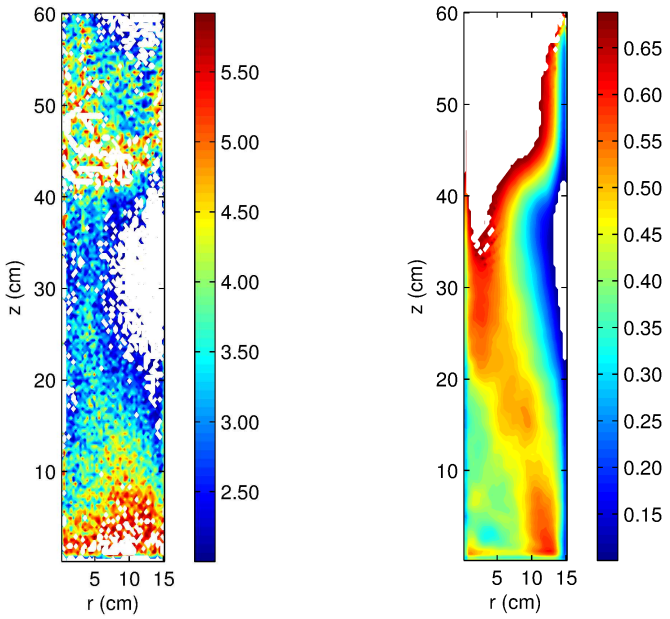

(a) Schaeffer model. **(b)** Princeton model.

Figure 2.3: Azimuthally and time-averaged inertial number.

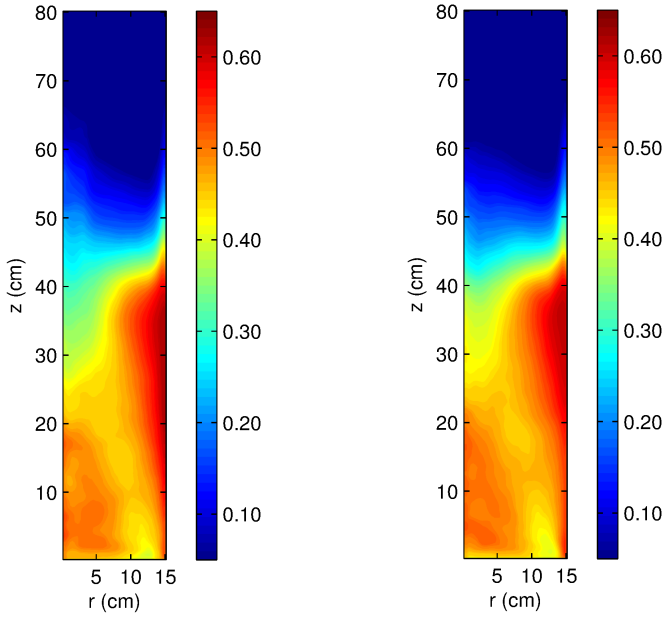

(a) Schaeffer model. **(b)** Princeton model.

Figure 2.4: Azimuthally and time-averaged particle volume fraction.

at a specific height in the bed, the measured gas holdup versus the profiles predicted by the simulations performed by Taghipour et al. [58], and the Schaeffer and Princeton models used in the present study. This figure indicates that the present computational model predicts values of the gas holdup that are in better agreement with the experimental data than the numerical result of [58]. As shown in Figures 2.4 and 2.5, overall, the difference in the values of gas holdup predicted by the Schaeffer and Princeton models is minimal.

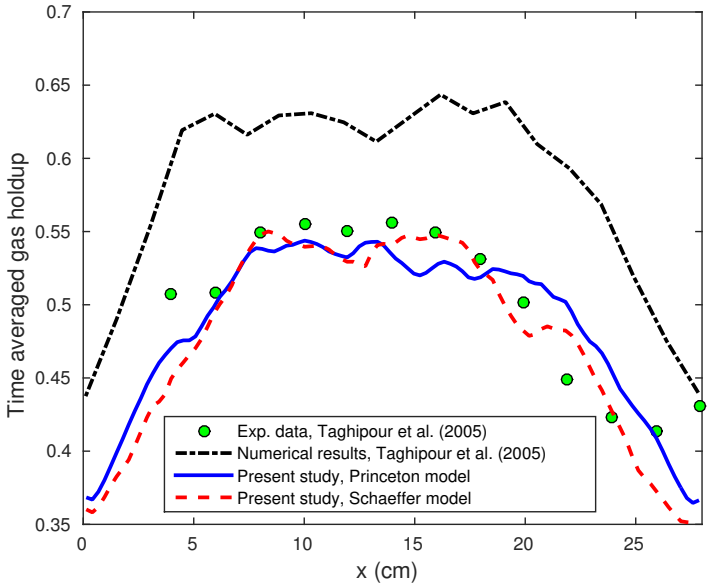

Figure 2.5: Experimentally measured and model predicted profiles of gas holdup across the bed.

2.4.2 Effects of the stress models on the prediction of flow regimes

To understand the differences between the results predicted by each model, it is helpful to note the behavior of the granular materials under different circumstances. At a large applied stress, particles deform at the contact point(s) and are compressed into the vacant inter-particle space. In this quasi-static regime, the particle pressure and shear stresses are independent of the strain rate. In contrast, at high shear strain rates for the rapid-flow regime, the momentum transport is due to the instantaneous binary collisions as well as the inertia of the inter-particle motions. Therefore, in this regime, the rheology of the particles is described by the coefficient of restitution and granular temperature and P_p, $\tau_p \sim \dot{\gamma}_p^2$. Between these two asymptotic regimes is the so-called intermediate or elastic-inertial regime, where P_p, $\tau_p \sim \dot{\gamma}_p^n$, with $0.5 \leq n \leq 1$ [59]. In the rapid-flow regime, the collisions are assumed to be infinitely rigid. However, once a particle is in multiple contact with surrounding particles, the elastic forces do play a role in the momentum transport, and the force chains [60] emerge to be a distinguished structural feature of this elastic-inertial regime. We note that the above relations for the dependence of P_p and τ_p on $\dot{\gamma}_p$ is valid for dry granular flows. These relations show more complicated behaviors when the effect of the interstitial fluid is introduced into the constitutive

equations.

To understand and quantify the dynamics of dense gas-particle flows, it is helpful to look at the local inertial number, as introduced above, whose value can be used to identify the regime of the flow. We note that the inertial number, which is the square root of the Savage number [23], can be interpreted as the ratio of the inertial timescale to the macroscopic deformation timescale. For the rapid or inertial regime, I has large values on the order of unity, whereas for the quasi-static regime, I has small values in the order of 10^{-3}; values in between correspond to the elastic-inertial regime. Figure 2.6 shows instantaneous values of the particle volume fraction, the inertial number, and the particle viscosity in a single plane. We note that three consecutive planes in the azimuthal direction are chosen to calculate $|\dot{\gamma}|$ on the middle plane. Both models predict that the flows inside the bubbles and free-board have the largest value of I corresponding to the rapid-flow regime and the lowest value of the particle viscosity. For the regions around and between the bubbles, I has moderate values, mapping the flow to the elastic-inertial regime. In these regions, the values of viscosity are also moderate. The regions of dark blue in the inertial number contour plot indicate a slow flow corresponding to the highest values of viscosity. Overall, based on Figure 2.4, the slow-flow regime predicted by both models is mostly located near the wall region. We note that regions in which the flow is elastic-inertia are extensive. However, the Schaeffer model treats these regions as a rapid flow, whereas the the Princeton model tries to improve their treatment by adding a frictional stress to the kinetic stresses. We recall from Figure 2.3 that the overall values of I predicted by the Schaeffer model are an order of magnitude greater than their counterparts predicted by the Princeton model. This is due to the fact that the Schaeffer model does not differentiate between the rapid-flow regime, corresponding to $I \sim 1.0$, and the intermediate regime, corresponding to $I \sim 10^{-1}$, and applies the same constitutive equations for both regimes.

Figure 2.7 shows instantaneous values of the second invariant of the total particle stress tensor as well as the frictional and kinetic/collisional contributions in the same plane used in Figure 2.6. Figure 2.7a clearly shows that there is an abrupt transition between the values of frictional and kinetic/collision stresses. The contours suggest that for the Schaeffer model the stress tensor in a specific region is dominated by either the frictional or kinetic/collisional counterparts. There is no region where both mechanisms are of the same significance. In contrast, Figure 2.7b illustrates that for the Princeton model there are extended regions in the bed where both frictional and kinetic/collisional stresses are of the same order of magnitude. For other regions where friction is dominant the changes in the values of the frictional and kinetic/collisional stresses are smoother compared to those in Figure 2.7a.

2.4.3 Effects of the stress models on the bubble characteristics

The inlet gas velocity in the present study is 3.5 times the minimum fluidization velocity, and the flow corresponds to the bubbling and/or slugging regime. Here, a bubble is understood to be a localized region of gas, typically moving as an entity through the particulate phase.

Figure 2.8 shows the instantaneous gas fraction in the vertical mid-plane of the fluidized bed, together

with a 3D visualization of the instantaneous bubble structures at four consecutive times. Here, red and blue contours indicate gas and particle phases, respectively. Although there is no precise criterion for defining the extent of a bubble, for the current study, a gas fraction of 0.8 has been used as the threshold value to determine the bubble boundary as has been used in, e.g., Verma et al. [34], Li et al. [45], and Passalacqua [32]. Figure 2.8 illustrates that the larger bubbles tend to become elongated due to wall effects and create a core-annular flow structure that consists of a core region in which the bubbles carry the particles up and an annular region where the particles descend along the wall. From Figure 2.8, it can be seen that the formation of large bubble structures occurs due to the coalescence of small bubbles that originate in the bottom and near-wall regions of the bed. Also, it can be observed that as the bubbles rise, they tend to migrate towards the centerline due to the lower resistance in the central region [6]. Eventually, the bubbles burst at the surface of the bed, and the particles, being carried by the bubbles, fall toward the walls, leading to fluctuations in the bed surface. We note that Figure 2.8 shows only the results from using the Princeton model for frictional stresses.

In order to assess the bubble characteristics quantitatively, the equivalent bubble diameter and average number of bubbles have been calculated for a transverse cross-section at different heights. Assuming that individual bubbles detected in a given cross-section (in the $r\theta$-plane) have a circular shape, the equivalent bubble diameter, D_e, is first calculated and then time-averaged based on the following expressions [61]:

$$D_e = \frac{1}{N_b} \sum_{i=1}^{N_b} D_{b,i},$$

where

$$D_{b,i} = \sqrt{\frac{4A_{b,i}}{\pi}},$$

N_b is the number of detected bubbles, and $A_{b,i}$ and $D_{b,i}$ are the area and equivalent bubble diameter of bubble i, respectively, at each transverse cross-section.

In this study, the predicted equivalent bubble diameters are compared with the correlations proposed by Hilligardt and Werther [62], Darton et al. [63], and Cai et al. [64] given in Table 2.2. Here z is the height of the bubble above the distributor plate, and $u_{z,0} - u_{mf}$ is the excess gas velocity, i.e., the difference between the superficial gas velocity at the inlet and minimum fluidization velocity. Figures 2.9a and 2.9b show the time-averaged equivalent bubble diameter and the average number of bubbles as a function of height. This figure illustrates the fact that there are fewer but relatively larger bubbles (as a result of the coalescence process) with increasing height in this region of the bed. Figure 2.9a indicates that the numerically predicted values by both the Schaeffer and Princeton models are much closer to the Hilligardt and Werther correlation than that of Darton et al. and Cai et al. The discrepancy between values calculated based on the numerical simulations and the correlation of Darton et al. has also been reported by Verma et al. [61]. Based on Figure 2.9a, comparing the equivalent bubble diameter predicted by both frictional stress models indicates that the values associated with the Princeton model are in better agreement with the Hilligardt and Werther correlation. It is worth noting that in the calculation of the equivalent bubble diameter and average number

of bubbles, it is assumed that the bubbles have a spherical shape, whereas their actual shape is not spherical. In other words, the equivalent bubble size and average number of bubbles are useful tools to study the general trend of bubble formation; however, the actual bubble field is significantly more complex. According to Hilligardt and Werther [62], bubble growth is affected by both coalescence and splitting mechanisms. Therefore, in order to describe the bubble growth more accurately, it is essential to consider the relevant physical mechanisms. However, there is no splitting mechanism in the bubble growth correlation of Darton et al. Figure 2.10 considers a different location in the bed where the rate of bubble growth decreases with height and the average number of bubbles begins to increase, indicating the dominance of bubble splitting and breakage in this region of the bed.

Table 2.2: Correlations for equivalent bubble diameter.

Author(s)	Correlation	Particle type	Bed Geometry	D_0
Hilligardt and Werther (1986)	$D_e = D_0(1 + 27(u_{z,0} - u_{mf}))^{1/3}(1 + 6.84z)^{1.2}$	Geldart A, B, and D	3D	0.0061
				0.0085
				0.0123
Darton et al. (1977)	$D_e = 0.54(u_{z,0} - u_{mf})^{0.4}(z + 4\sqrt{A_0})^{0.8}g^{-0.2}$	Geldart B	2D	—
	$4\sqrt{A_0} = 0.03$ m (Porous plate)			
Cai et al. (1994)	$D_e = 0.38h^{0.8}(u_{z,0} - u_{mf}))^{0.42}exp(0.25(u_{z,0} - u_{mf})^2 - 0.1(u_{z,0} - u_{mf}))$	Geldart A, B, and D	3D	—

2.4.4 Effects of the stress models on the gas pressure fluctuations

It is evident from Figure 2.8 that the dynamics of the bed is highly influenced by the bubbles moving up through the bed. The chaotic motion of the bubbles is reminiscent of large-scale eddies in single-phase turbulent flows. To gain a better understanding of such an unsteady flow, it is helpful to look at the Power Spectral Density (PSD) of gas pressure field. In order to do this, two probes were placed at the center of the bed at heights of $z = 31$ cm and 32 cm to measure the gas pressure. Figure 2.11 plots the difference between the pressure values at these heights for the period from 3 to 5 s. In order to interpret the signal fluctuations depicted in Figure 2.11, it is helpful to look at the instantaneous snapshots of the bubble contours in the 3D bed, as depicted in Figure 2.8. These snapshots correspond to the four successive time instants marked in Figure 2.11, arranged sequentially, from left to right. In the left-most snapshot of Figure 2.8, the bubble is approaching the probes (represented by two white points), leading to an increase in the gas pressure difference as illustrated in Figure 2.11. This pressure difference starts to decrease from Point 1 to a minimum at Point 3 due to the fact that the bubble is traversing the probes. Eventually, the pressure difference recovers and reaches a second peak right after the bubble has passed both probes, as can be seen in the right-most snapshot in Figure 2.8. Figure 2.12 explains why the pressure difference reaches its minimum value when both probes are located within the bubble. This figure shows the gas pressure and particle volume fraction at the times corresponding to points 1 and 3 in Figure 2.11, respectively. According to Figure 2.12a, the higher probe experiences a lower pressure than the lower probe as the bubble approaches. However, as shown in Figure 2.12b, once both probes are located within the same bubble, they experience approximately

the same pressure field, resulting in a minimum pressure difference.

It has been suggested that the pressure difference signals carry local information, whereas the absolute pressure signals are more reflective of the global behavior [65]. Therefore, in order to investigate the global behavior of bubbles predicted by each stress model it is helpful to look at the PSD of the pressure field. Figure 2.13 shows the PSD of the pressure signals at a height of 10 cm for both the Schaeffer and Princeton models in the frequency domain. In bubbling beds, the low frequencies may be associated with the movement of the bulk particle flow, i.e., bubbling motions [66], whereas the high frequencies may be related to the gas interaction with the particles. Also, the dominant frequency is attributed to the natural frequency of the bed fluctuations [65]. Figure 2.13 indicates that the the Schaeffer model predicts a stronger intensity in the gas pressure fluctuations, suggesting more vigorous bubbles compared to the results predicted using the Princeton model. This is because the Schaeffer model does not consider the friction between particles in the elastic-inertia regime. Consequently, the gas inside the bubbles experiences a smaller pressure drop while carrying the particles across the bed. Due to the more vigorous bubbles predicted by the Schaeffer model, a higher natural frequency of the system is also obtained. The PSD analysis shows that the natural frequencies predicted by the Schaeffer and Princeton models are 3.5 Hz and 2.75 Hz, respectively. More vigorous bubbles may also be coupled to a larger particle Reynolds stress, discussed in the following section.

2.4.5 Effect of the stress models on the "resolved-scale" particle Reynolds stress

There are two types of granular temperature in fluidization [67], namely, the particle granular temperature, originating from the random oscillation of individual particles, and a granular temperature due to the motion of bubbles, referred to as the turbulent granular temperature by Gidaspow et al. [67]. We note that the term "turbulent granular temperature" may be misleading because there is a clear distinction between the small-scale molecular fluctuations and resolved-scale fluctuations. Therefore, to avoid any misunderstanding, the terminology "resolved-scale fluctuations" is used. The resolved-scale fluctuations due to the motion of bubbles can be calculated by taking the variance of the particle velocity predicted by the two-fluid model. Following Gidaspow et al. [67], the particle Reynolds stress per unit bulk density is defined as:

$$\overline{u_i' u_{j\,(x)}'} = \frac{1}{T}\int_{t_0}^{t_0+T} (u_{i(x)} - \overline{u_i}_{(x)})(u_{j\,(x)} - \overline{u_j}_{(x)})\, dt, \tag{2.31}$$

$$\overline{u_i}_{(x)} = \frac{1}{T}\int_{t_0}^{t_0+T} u_{i(x,t)}\, dt. \tag{2.32}$$

Similar to the definition of the particle granular temperature, the resolved-scale fluctuations is defined as [67]:

$$\theta_{\text{bubble}(x)} = \frac{1}{3}\overline{u_i' u_{i(x)}'} \tag{2.33}$$

Figure 2.14 shows the time-averaged profiles of the granular temperature and the resolved-scale fluctuations for each stress model at a height of 21 cm. This figure illustrates that the resolved-scale particle Reynolds stress, is much larger than the particle granular temperature indicating that the particle oscillations associated

with clusters dominate the individual particle oscillations. Figure 2.14 also indicates that the resolved-scale fluctuations predicted by the Schaeffer model are larger than those predicted by the Princeton model. As discussed in the previous section, the larger resolved-scale particle Reynolds stress is a result of the more vigorous bubble activity predicted by the Schaeffer model. To understand why the Schaeffer model predicts an overall higher granular temperature at this height, it is helpful to look at the production and dissipation terms in the granular energy Eq. 2.16. Figure 2.15a, which shows the azimuthally and time-averaged value of the production term at the height of 21 cm, indicates that the Princeton model predicts higher values for the production of granular temperature. We note that the granular temperature can be produced in both the rapid-flow and intermediate regimes. In the intermediate regime, because particles are in longer contact compared to the rapid-flow regime, it is also expected that the production of granular temperature would be higher due to both shear and normal stresses. Because the intermediate regime is captured by the Princeton model, a greater overall production of granular temperature is expected to be predicted. Longer contacts in this regime also imply greater dissipation of granular energy. The level of the granular temperature depends on the net production, i.e., the production less the dissipation term, and is presented in Figure 2.15b. The Schaeffer model predicts higher values of the net production, which in turn leads the Schaeffer model to predict higher values of the granular temperature. The effect of the interphase exchange term was found to be negligible compared to production and dissipation terms. We note that the value of granular temperature is not solely determined by these source terms because unsteady and convection/diffusion effects are also present.

2.5 Conclusion

This study demonstrates the significant role of the particle stress tensor in the prediction of dense gas-particle flows using a two-fluid model. The model, which is based on the kinetic theory of granular flow for the rapid-flow regime and the Coulomb friction law for the slow-plastic regime, was applied to predict the hydrodynamics of dense gas-particle flow in a 3D fluidized bed.

Although both the Schaeffer and Princeton models have already been the subject of several studies that assessed their ability to predict the overall behavior of fluidized beds, the main focus of this study was on how these models modified the simulated flow structures. To that end, a dimensionless inertial number was used to identify different flow regimes corresponding to different particle stress behaviors. It appears that this is the first time that contours of inertial number have been used to visualize the flow properties. Analysis of the flow properties for a range of gas-particle regimes based on the inertial number enhances our insight into the flow behavior in such a complex multiphase system. The paper quantitatively explains some important features of the mechanics of bubbling/slugging beds that have received relatively little attention in the literature. For example, the effects of two different stress models on the circulation patterns, velocity profiles, bubble characteristics, natural frequency of the bed and "resolved-scale" particle Reynolds stress

were investigated in detail.

The results using the Princeton stress model were found to be closer to the experimental data for the axial particle velocity and flow circulation pattern than those based on the Schaeffer model. This was because, unlike the Schaeffer model, the Princeton model differentiates between the rapid-flow regime and the intermediate elastic-inertia regime and applies different constitutive equations for each regime.

The Schaeffer model predicted a higher natural frequency for the bed and more vigorous bubble activity compared to that predicted by the Princeton model. The particulate phase showed turbulent-like behavior partly due to the motion of bubble structures in the bed. The Reynolds stress associated with this turbulent-like behavior was calculated from the resolved-scale fluctuations and found to be much larger than the fluctuations associated with the particle granular temperature. Comparing the results of the two stress models indicated that the Schaeffer model predicted a larger particle Reynolds stress; this behavior was attributed to the prediction of more vigorous bubbles. We also note also that the use of the Princeton model results in a faster algorithm that is less prone to divergence. Finally, the Schaeffer model was found to predict a higher level for the granular temperature that was explained on the basis of the enhanced level of the net production term in the transport equation.

Looking forward, the results of this study indicate that a particle stress model that uses an inertial number dependent rheology would be an especially promising approach for predicting the flow dynamics in bubbling fluidized beds.

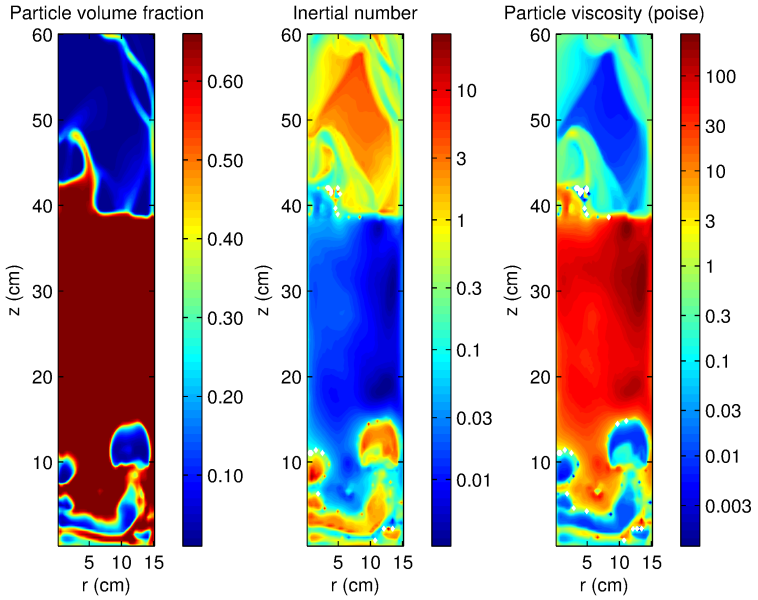

(a) Schaeffer model.

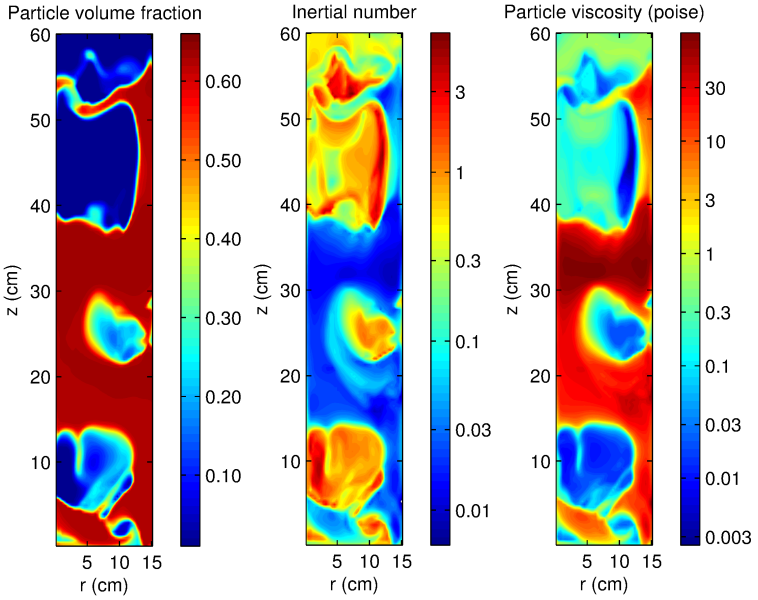

(b) Princeton model.

Figure 2.6: Distributions of particle volume fraction, inertial number, and particle viscosity at $t = 4$ s.

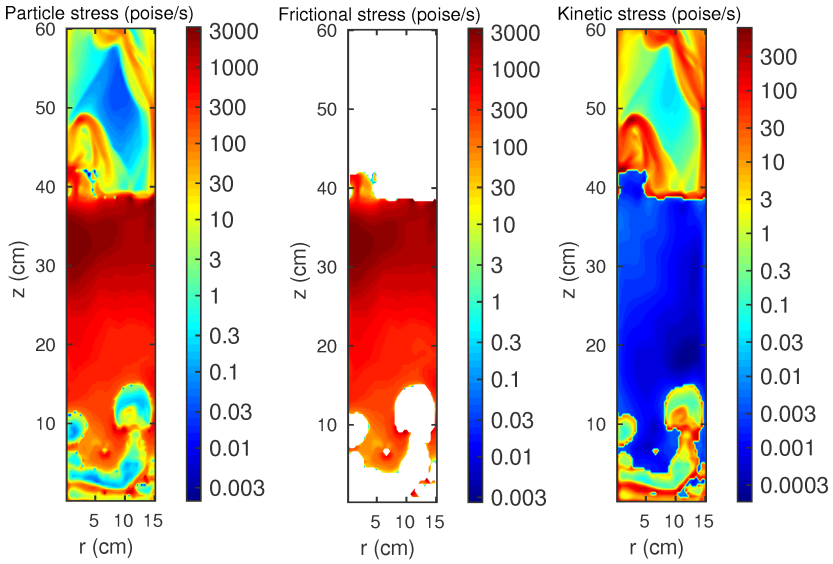

(a) Schaeffer model.

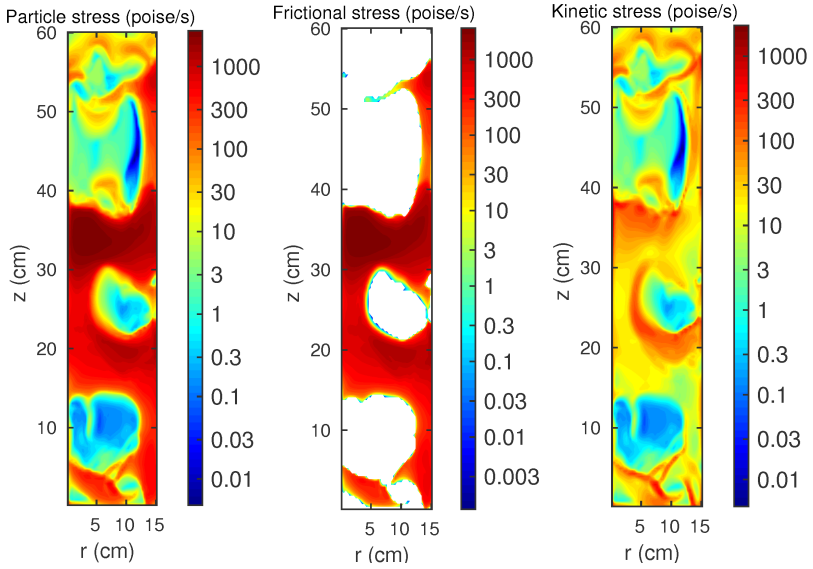

(b) Princeton model.

Figure 2.7: Distributions of total particle stress and frictional and kinetic/collisional contributions at $t = 4$ s. White regions indicate no contribution.

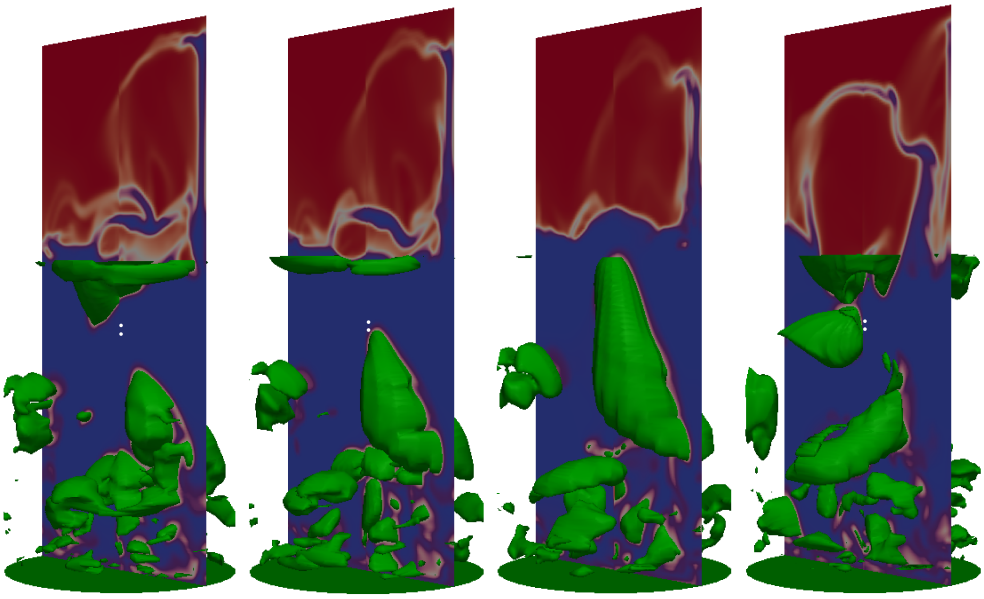

Figure 2.8: Instantaneous snapshots of green bubble contours in the mid-plane for four successive instants of $t = 4.40, 4.43, 4.47$, and 4.60 s from left to right (Princeton model), respectively. Red and blue contours in the mid-plane indicate gas and particle phases, respectively.

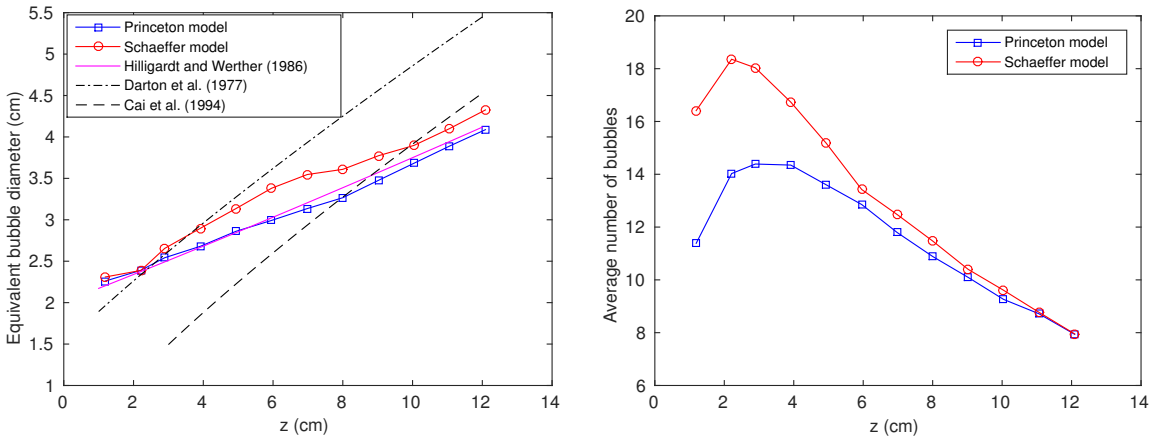

(a) Average bubble size. **(b)** Average number of bubbles.

Figure 2.9: Comparison between Schaeffer and Princeton frictional models. (a) Average bubble size and (b) Average number of bubbles vs. height z.

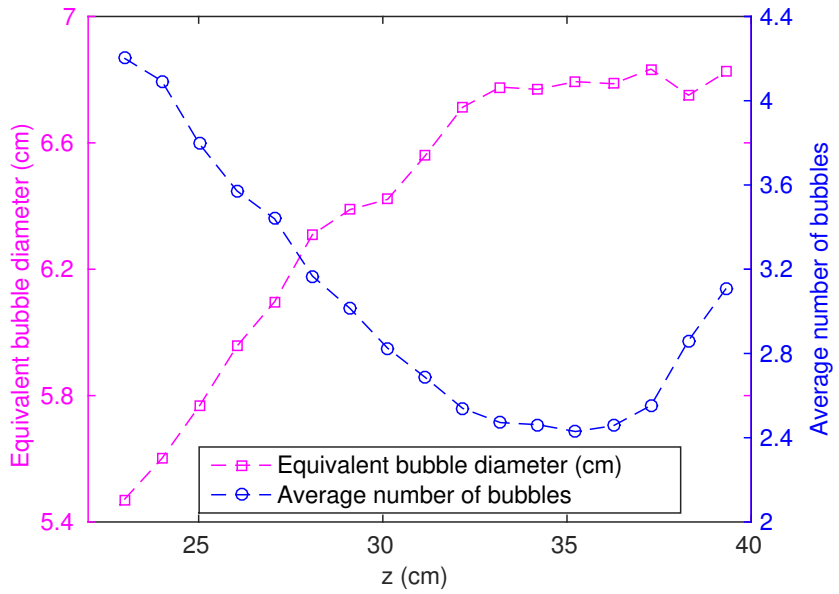

Figure 2.10: Average bubble size and number of bubbles as a function of z (Princeton model).

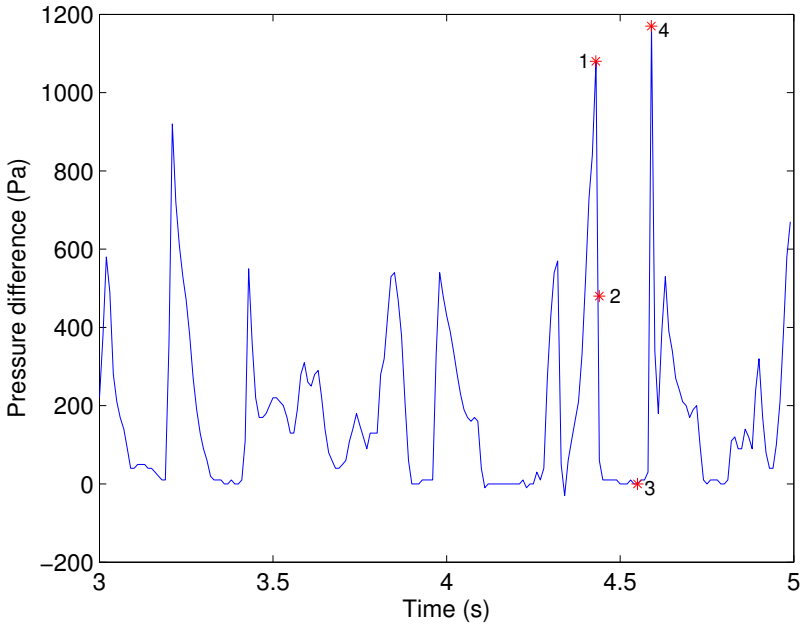

Figure 2.11: Pressure difference calculated from the pressure values at $z = 31$ cm and 32 cm.

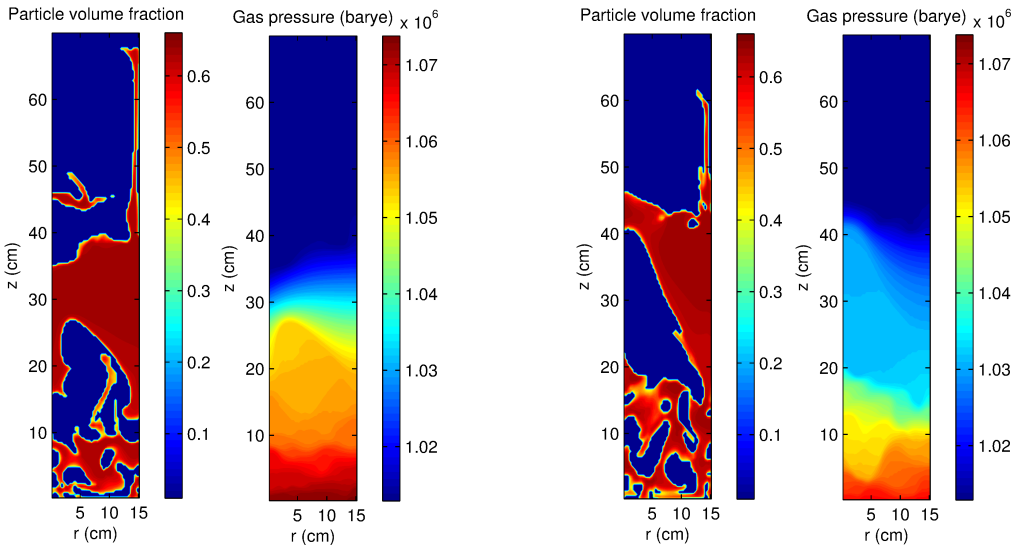

Figure 2.12: Gas pressure and particle volume fraction contours corresponding to (a) point 1 and (b) point 3, respectively, in Figure 2.11. Probes are located at $z = 31$ cm and 32 cm.

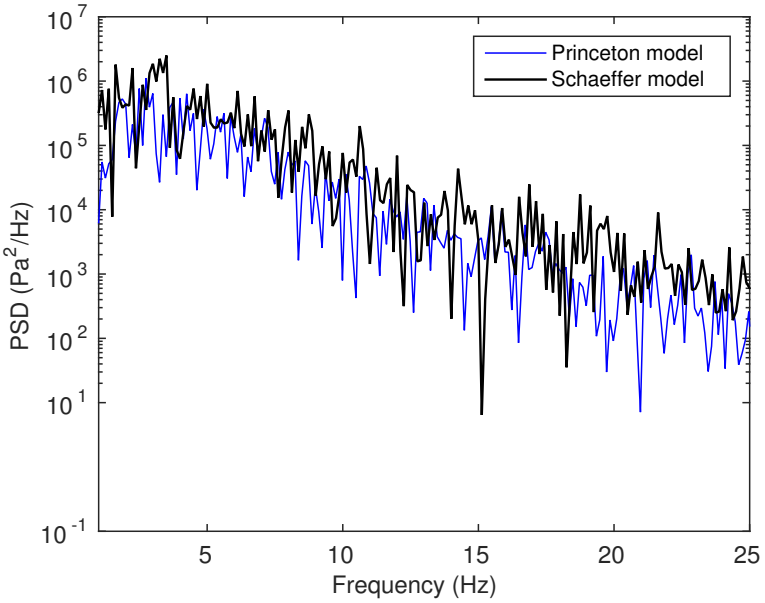

Figure 2.13: Power Spectral Density of pressure signals at $z = 10$ cm.

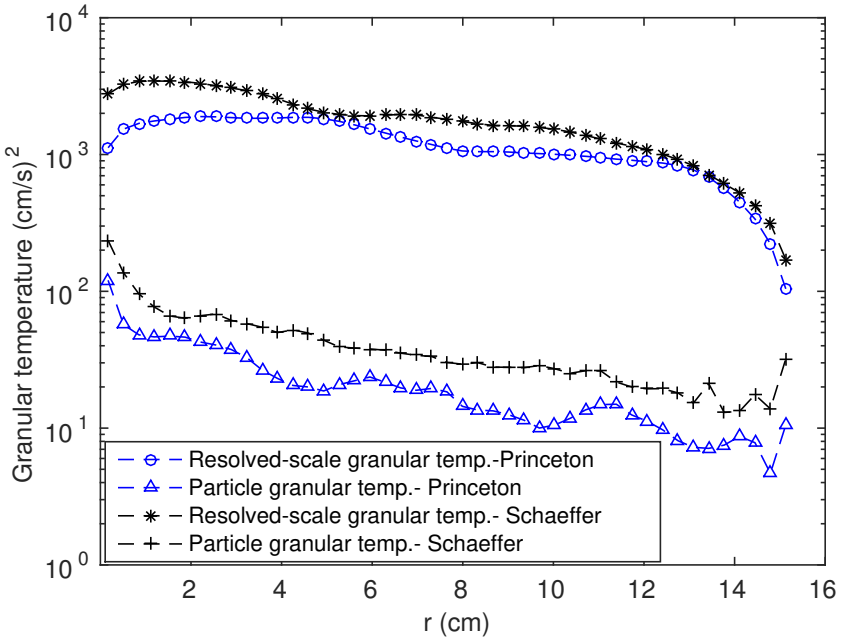

Figure 2.14: Comparison between the time-averaged profiles of the granular temperature and the resolved-scale fluctuations predicted by the Schaeffer and Princeton models at $z = 21$ cm.

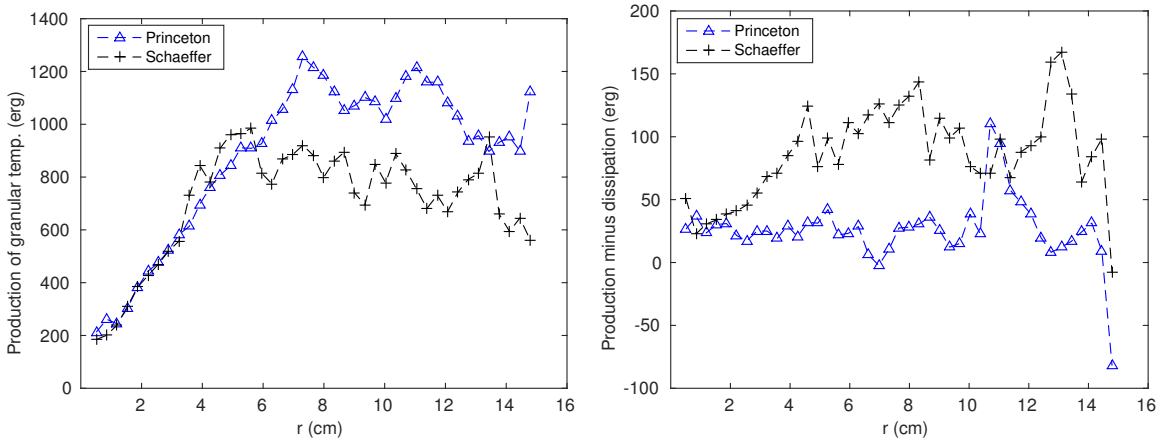

(a) Production of granular energy.

(b) Production minus dissipation of granular energy.

Figure 2.15: Azimuthally and time-averaged values of source terms in the granular energy equation at $z = 21$ cm.

Chapter 3

A comprehensive assessment of different wall boundary conditions on the simulation of bubbling fluidized beds

A similar version of this chapter has been published as:

- M. R. Haghgoo, D. J. Bergstrom, and R. J. Spiteri. A comprehensive assessment of different wall boundary conditions on the simulation of bubbling fluidized beds. *Int. J. Multiphase Flow* 99 (2018) 500–511.

The first author conducted the simulations, post-processed and analyzed the results, and prepared the first draft of the manuscript. He then worked with the co-authors to discuss the results and finalize the content and form of the manuscript.

Preamble

In addition to the closure relations discussed in the previous chapter, to perform a realistic prediction of fluidized beds, it is also significant to determine a proper set of boundary conditions for the particle-wall interaction. To this end, three different particle-wall boundary conditions are examined to assess their ability to predict the dynamics of a dense gas-particle flow inside a three-dimensional thin bubbling bed.

One contribution of this chapter is that it quantitatively explores the effect of each particular boundary condition on the predicted flow behavior through a comprehensive study and determines the boundary condition that predicts better agreement with the measured data. Another contribution of this chapter is that, for the first time, the contours of particle Reynolds stress are used to identify the dominant mixing regions inside the bed.

Abstract

There are different particle-wall boundary conditions available in the literature to account for the particle slip velocity and the granular energy flux at the wall. However, it is not yet clear how these different wall boundary conditions affect the simulated flow behavior, nor is it clear which are the most realistic. To this end, three different particle-wall boundary conditions are examined to assess their ability to predict the dynamics of a dense gas-particle flow inside a three-dimensional bubbling bed, using the two-fluid model. To understand how the wall models affect structural features of the flow, a quantitative analysis is performed on some important aspects of the mechanics of bubbling beds that have received relatively little attention in the literature. Accordingly, the effect of each wall model on the velocity field, three-dimensional bubble statistics, gas-pressure fluctuations, and particle resolved-scale Reynolds stress are investigated. Also, the predicted dominant mixing regions inside the bed are identified and visualized in order to quantitatively describe the bed performance. It is found that the more energetic bubbles result in a lower level of granular temperature, a less-expanded bed, and more extensive mixing regions inside the bed. It is also observed that, in the case of bubbling beds, the mixing caused by the Reynolds normal stress is much stronger than that caused by the Reynolds shear stress. Overall, the flows predicted by the three wall models are structurally similar. However, some specific features can differ in a systematic way that can be tracked to the effect of wall boundary condition on the bubble behavior. The numerical results are validated against published experimental data and demonstrate the significant role of the particle-wall boundary condition.

3.1 Introduction

A great deal of work has been performed in the attempt to derive an accurate and computationally efficient set of governing/closure equations to numerically predict fluid-particle flows. To this end, Anderson and Jackson [7], among other researchers, derived a set of locally averaged equations to describe both the particle and fluid phases as inter-penetrating continua. This Eulerian–Eulerian description is the most widely used approach to simulate large-scale fluid-particle flows in various applications, e.g., fluidized beds. Despite numerous efforts to improve this method, e.g., the so-called "two-fluid model" (TFM), less attention has been given to the corresponding wall boundary conditions (BCs) in the literature. In general, specifying an appropriate BC is as important as the set of governing/closure equations for realistic flow prediction.

There is a general consensus to apply a no-slip wall boundary condition on the fluid phase in the numerical study of fluid-particle flows. Regardless of the modeling approach, e.g., in the "Direct Numerical Simulation" of fluid-particle flows or in the TFM approach, applying a no-slip boundary condition to the fluid phase seems realistic because all of its velocity components vanish at the wall. As a result, the fluid's turbulence kinetic energy and its gradient, if any, should also vanish at the wall. Accordingly, a no-slip wall BC can be applied for the fluid phase in a TFM prediction of dense fluid-particle flows, where the turbulence of the carrier

phase, if any, is damped by the inertia of the particles.

Generally, three types of wall BC can be applied on the particle phase, i.e., no-slip, free-slip, and partial-slip BCs. Among these three BCs, the partial-slip one appears most realistic compared to the other two because particles, being a discrete phase, tend to slip over the wall. However, no-slip and free-slip BCs are used in some numerical studies of dense and dilute gas-particle flows, respectively, e.g.,Lu et al. [68] and Bahramian et al. [69]. There are various wall BCs proposed in the literature to account for the partial slip of the particles, namely, the BC of Johnson and Jackson [25], a revised form of the Johnson and Jackson BC by Li and Benyahia [70], the Jenkins BC [71], a revised form of the Jenkins BC by Jenkins and Louge [72], the BC of Schneiderbauer et al. [73], the BC of Zhao et al. [74] that takes into account the effect of rotation of particles at the wall, and the BC of Yang et al. [75].

In the heuristic model of Johnson and Jackson [25], the effect of momentum and energy transfer of the colliding particles is characterized by a specularity coefficient, and the momentum transfer of the sliding particles is characterized by a friction coefficient. The specularity coefficient value varies between zero for perfectly specular collisions and unity for perfectly diffuse collisions. The main challenge with the Johnson–Jackson model is that the value of the specularity coefficient must be specified by the user. In this sense, the specularity coefficient is not a measurable physical parameter but a tuning parameter. Accordingly, its value should be adjusted to achieve the best agreement with the measured data. In a seminal study, Fede et al. [76] investigated the effect of specularity coefficient on the predicted flow behavior in a three-dimensional (3D) bubbling bed. Also, Altantzis et al. [46] and Bakshi et al. [47] analyzed different flow patterns resulting from different values of the specularity coefficient. Regardless of the issue of determining a proper value for specularity coefficient, because of its relatively simple form, the Johnson–Jackson model is the most pervasively used BC in the literature. For example, Igci and Sundaresan [77], Passalacqua and Fox [78], Verma et al. [34], and Rangarajan [40] are a few recent works that used this particle-wall model. Li and Benyahia [70] revised the Johnson and Jackson BC and suggested an analytical expression for the specularity coefficient as a function of the measurable collision properties, i.e., the particle-wall restitution coefficient, the frictional coefficient, and the normalized slip velocity at the wall. Their work, however, did not include any modification to the original equation of the Johnson–Jackson model for flux of granular energy. Inspired by the the work of Li and Benyahia [70], Zhao et al. [79] also proposed a semi-analytical and flow-dependent model for the specularity coefficient.

Jenkins [71], on the other hand, distinguished between sticking and sliding collisions and calculated analytical expressions for the two extremes of flow behavior, where in one case all collisions involve sliding and in the other case friction is so large that particles do not slide. He called these asymptotic cases “small friction/all sliding” and “large friction/no sliding”, respectively [71]. He assumed that flows between these two limits can be captured by interpolating between the two extremes. Louge [80], however, using computer simulations, showed that Jenkins’s model greatly over predicted the flux of fluctuating energy. Jenkins and Louge [72] refined Jenkins’s calculations, proposed some corrections, and connected the two limits.

Schneiderbauer et al. [73] proposed a model to include the sliding and sticking collisions in one expression. Moreover, this model was derived to account for an unsteady condition of moving walls by considering the compression and expansion of the granular flow. Soleimani et al. [81] compared the wall shear stress and granular energy flux calculated by the model of Schneiderbauer et al. with the discrete element simulations of Louge [80] and observed fairly good agreement. Cloete et al. [82] performed a study to compare the predicted results of the Schneiderbauer et al. model with the Johnson–Jackson model in a 2D riser.

It is not yet clear how these different wall boundary conditions affect the simulated flow behavior, nor is it clear which are the most realistic. To this end, a comprehensive study is performed to assess the effect of three different wall BCs on the flow characteristics of a dense gas-particle flow inside a 3D bubbling bed. The wall BCs considered in this study include the Johnson–Jackson model [25], the Jenkins–Louge model [72], and the Schneiderbauer et al. model [73]. The BC of Li and Benyahia [70] was not included in this study because, as mentioned above, no improvement was suggested for the original wall granular temperature equation in the Johnson–Jackson model. The BC proposed by Zhao et al. [74] and Yang et al. [75] take into account the effect of particle rotation at the wall and require solving two extra conservation equations for the particle rotational momentum and rotational granular temperature and hence render them beyond the scope of this study. Although each of the three wall models mentioned above has already been the subject of several studies, this is the first time, to the best of authors' knowledge, that an in-depth systematic study is performed to assess and compare their abilities in the prediction of the hydrodynamics of a 3D bubbling bed. The paper attempts to quantitatively describe some important features of the mechanics of the bubbling beds that have received relatively little attention in the literature. For example, the effect of wall BC on the velocity field, 3D bubble statistics, gas-pressure fluctuations, and particle resolved-scale Reynolds stress are investigated. Also, to the best of our knowledge, it is the first time that contours of particle Reynolds stress are used to identify the dominant mixing regions inside the bed. The numerical code Multiphase Flow with Interphase eXchanges (MFIX) [11] was used to perform the simulations, using the Eulerian–Eulerian framework. Some additional subroutines were developed and integrated into the MFIX code to implement the BCs of Jenkins and Louge [72] and Schneiderbauer et al. [73]. The results were validated against published experimental data by Laverman et al.[83].

3.2 Mathematical modeling

The Eulerian–Eulerian TFM, based on the locally averaged equations derived by Anderson and Jackson [7], is used to simulate a dense gas-particle flow inside a 3D thin fluidized bed. All the governing/constitutive equations can be found in our previous study [20], except that in the current study the drag model of Gidaspow [84] is used. Haghgoo et al. [20] previously showed that the frictional stress proposed by Srivastava and Sundaresan [26] predicted more realistic results than the one proposed by Schaeffer [27]. Therefore, in this study the former frictional model was used to account for the longer-lasting multiple-particle contacts

with the frictional stress initiating at a particle volume fraction of $\varepsilon_p^{\min} = 0.6$.

In the present study, the effects of three different particle-wall boundary conditions on the simulated flow structure are investigated. The first one used is the Johnson–Jackson wall BC [25]. The particle-wall shear stress, $\vec{\tau}_w$, and granular energy flux, q_w, at the wall can be expressed as

$$\vec{\tau}_w = -\frac{\phi_w \pi \rho_p \varepsilon_p g_0 \sqrt{\Theta_p}}{2\sqrt{3}\varepsilon_p^{\max}} \vec{u}_{sl} - \mu_w N_f \frac{\vec{u}_{sl}}{|\vec{u}_{sl}|} \tag{3.1}$$

and

$$q_w = \frac{\phi_w \pi |\vec{u}_{sl}|^2 \rho_p \varepsilon_p g_0 \sqrt{\Theta_p}}{2\sqrt{3}\varepsilon_p^{\max}} - \frac{\sqrt{3}\pi \rho_p \varepsilon_p g_0 (1 - e_w^2)\sqrt{\Theta_p}}{4\varepsilon_p^{\max}} \Theta_p, \tag{3.2}$$

where $\vec{u}_{sl}$, ϕ_w, and e_w are the particle-wall slip velocity, specularity coefficient at the wall, and particle-wall restitution coefficient, respectively. Here, ρ_p, ε_p, g_0, Θ_p, $\varepsilon_p^{\max}$, and κ_p are the particle density, particle volume fraction, radial distribution function, granular temperature, packed bed particle volume fraction, and particle conductivity of the granular energy, respectively. Also, N_f is the component of frictional stress normal to the wall surface, and μ_w is the wall friction coefficient.

For the Jenkins–Louge BC [72], the wall shear stress is obtained from

$$\frac{\vec{\tau}_w}{N} = -\frac{\mu_w}{\overline{\mu}_0}\mathbf{R}\frac{\vec{u}_{sl}}{|\vec{u}_{sl}|} - \mu_w \frac{N_f}{N}\frac{\vec{u}_{sl}}{|\vec{u}_{sl}|}, \qquad \mathbf{R} = \begin{cases} \dfrac{3}{2}r & r \le \dfrac{2\overline{\mu}_0}{3}; \quad \text{large friction/no sliding,} \\ \overline{\mu}_0 & r > \dfrac{2\overline{\mu}_0}{3}; \quad \text{small friction/all sliding.} \end{cases} \tag{3.3}$$

Following Schneiderbauer et al. [73], the wall normal stress is calculated by $N = \frac{1}{2}(1 + e_w)\rho_p \varepsilon_p g_0 \Theta_p$. In Eq. 3.3, $\overline{\mu}_0 \equiv \dfrac{\mu_0}{1 + \beta_0}$ and $\mu_0 \equiv \frac{7}{2}(1 + e_w)\mu_w$, where β_0 is the tangential restitution coefficient. Here, the normalized slip velocity is defined by $r = \dfrac{|\vec{u}_{sl}|}{\sqrt{3\Theta_p}}$. The granular energy flux is calculated by

$$\begin{aligned} \frac{q_w}{N\sqrt{3\Theta_p}} = -\sqrt{\frac{\pi}{6}}\Bigg\{ & \frac{2}{\pi}(1 - e_w) + \frac{\mu_w}{\overline{\mu}_0}\sin^4\phi_0 \left[(1 - \beta_0)\left(1 - 2r^2\cos 2\phi_0\right) - 4r^2\right] \\ & + \frac{\mu_w}{2}\left[(\pi - 2\phi_0 + \sin 2\phi_0 \cos 2\phi_0)\left(1 - r^2\right) + 2r^2\sin^3 2\phi_0\right] \\ & - \mu_w \overline{\mu}_0 (1 + \beta_0)\cos^4\phi_0 \left(1 + 3r^2\sin^2\phi_0\right)\Bigg\}, \end{aligned} \tag{3.4a}$$

$$\frac{q_w}{N\sqrt{3\Theta_p}} = \frac{2}{(1 + e_w)}\sqrt{\frac{2}{3\pi}}\left[\frac{1}{7}\mu_0^2 - \frac{1}{2}\left(1 - e_w^2\right) - \mu_w \mu_0 e_w \left(\frac{1 + e_w}{e_w + \frac{2}{e}}\right)\right]. \tag{3.4b}$$

In Eq. 3.4, $\phi_0 = \arctan(\overline{\mu}_0)$, and e is the particle-particle restitution coefficient. Following Jenkins and Louge [72], for a given value of r, a minimum of granular energy flux between the values calculated by the small sliding curve Eq. 3.4a and the all-sliding limit Eq. 3.4b is implemented at the wall.

For the model of Schneiderbauer et al. [73], the wall shear stress is calculated by

$$\frac{\vec{\tau}_w}{N} = \mu_w \mathrm{erf}\left(\sqrt{\frac{3}{2}}\frac{r}{\overline{\mu}_0}\right)\frac{\vec{u}_{sl}}{|\vec{u}_{sl}|} - \mu_w \frac{N_f}{N}\frac{\vec{u}_{sl}}{|\vec{u}_{sl}|}, \tag{3.5}$$

and the particle fluctuating energy flux is expressed by

$$\frac{q_w}{N\sqrt{3\Theta_p}} = \frac{1}{\sqrt{6\pi}}\Bigg\{2\left(e_w-1\right)+3\mu_w^2\left(1+e_w\right)+\frac{\mu_w^2}{\overline{\mu}_0^2}\exp\left(-\overline{u}^2\right)\Bigg[6r^2\left(1+e_w-\overline{\mu}_0\right)+ \\ 7\left(1+e_w\right)-4\frac{\overline{\mu}_0}{\mu_w}\left(1+\mu_w\right)-3\overline{\mu}_0^2\left(1+e_w\right)\Bigg]\Bigg\}, \tag{3.6}$$

where $\overline{u} \equiv \sqrt{\frac{3}{2}}\frac{r}{\overline{\mu}_0}$. Detailed discussions on the derivation of these BCs are available in the original papers referenced above.

3.3 Numerical simulation

Using the TFM approach of Anderson and Jackson [7], 3D simulations of a thin fluidized bed were performed to assess the effect of particle-wall BC on the numerical prediction of the bed dynamics. The numerical code MFIX, a set of open-source FORTRAN subroutines, was used to perform the simulations. The MFIX code did not originally include the wall BCs proposed by Jenkins and Louge [72] and Schneiderbauer et al. [73]. Therefore, additional subroutines were developed to implement these wall BCs. The numerical results of this study were compared with the experimental measurements of Laverman et al. [83]. Table 3.1 shows the simulation parameters based on the experimental set-up.

Table 3.1: Simulation parameters for comparison with experimental study

Property	Value
Fluidized bed height	70 cm
Fluidized bed width	30 cm
Fluidized bed thickness	1.5 cm
Initial bed height	30 cm
Particle diameter, d_p	0.485 mm
Particle density, ρ_p	2500 kg m^{-3}
Minimum fluidization velocity, u_{mf}	18 cm s^{-1}
Superficial gas velocity	$2.5u_{mf}$

3.3.1 Numerical methodology

The governing equations are discretized using the finite volume method, resulting in a set of linear algebraic equations in the form of a septa-diagonal matrix of unknown variables. At each interior control volume, there are nine unknowns to be solved for, including three phasic velocity components, a pressure correction for the gas phase, a volume correction for the particle phase, and a granular temperature. An iterative method using a biconjugate gradient technique was used to solve the system of linear equations. It is reported that first-order discretization schemes produce unrealistic bubble shapes caused by excessive numerical diffusion

[85], which in turn can affect the flow structure. To produce realistic flow patterns in an efficient manner, the higher-order Superbee scheme was used in the spatial discretization scheme [49]. To enhance numerical stability, a deferred correction (DC) scheme was implemented so that it used an upwind method implicitly and the Superbee method explicitly to calculate the convection terms. The time discretization was the backward Euler method with a variable time step [11]. The non-linear source terms are linearized and treated with a semi-implicit method that also serves to reduce instabilities. The numerical technique is based on a modified SIMPLE algorithm for multiphase flows to solve the pressure and volume fraction correction equations [11]. The interphase transfer terms strongly couple the momentum equations of each phase to one another. In order to decouple the equations, the interphase transfer terms can be calculated from the previous iteration values. However, this approach makes the solutions unstable and prone to divergence. On the other hand, solving the discretized equations simultaneously requires solving a large and non-standard matrix of unknowns. Following Spalding [86], MFIX uses a Partial Elimination Algorithm to preserve the septa-diagonal form of the matrix while offering a high degree of coupling between the equations.

All simulations were performed in parallel using 60 cores on an architecture consisting of dual Hex Core Intel Xeon X5650 2.66 GHz with 12 GB of RAM each and running Red Hat Enterprise Linux Server 5.7. The first 100 seconds of the fluidization process are simulated to achieve statistically steady-state solutions. Table 3.2 gives the computational time required to perform a simulation for each wall BC. We observe that the computational time required by the BCs Jenkins and Louge and Schneidenbauer et al. are approximately double that of Johnson and Jackson. We note that although the functional forms of the Jenkins–Louge and Schneiderbauer et al. BCs are more complex than the form of Johnson–Jackson BC, their complexity is not the reason for the significant differences in the computational time. It was observed that the simulations using the Jenkins–Louge and Schneiderbauer et al. BCs required much smaller time steps to achieve convergence. This indicates that these BCs make the system of equations more stiff, and hence smaller time steps were required for convergence compared to the system of equations closed by the Johnson–Jackson BC.

Table 3.2: Comparison of computational cost of various wall BCs

Boundary condition	Cores used	Computational time
Johnson and Jackson [25]	60	20 days and 10 h
Jenkins and Louge [72]	60	40 days and 14 h
Schneiderbauer et al. [73]	60	41 days and 2 h

3.3.2 Physical parameters

It is well-established that the results of the TFM are highly dependent on the constitutive relations used to close the governing equations. Accordingly, the values of the model parameters that appear in the constitutive relations must be carefully chosen to ensure realistic behavior. To this end, extensive 3D simulations

were performed to obtain the model parameter values that yielded the most comparable results with the experimental data. For example, for the particle-particle restitution coefficient, the values of 0.86, 0.88, 0.92, and 0.95 were examined. It was determined that $e = 0.88$ along with a specularity coefficient of 0.03 yielded the best results compared to the experimental data of Laverman et al. [83]. Values of 0.01, 0.03, 0.05, and 0.4 were examined for the specularity coefficient. Also, it was determined that $\varepsilon_p^{\min} = 0.6$ gave better agreement with the measured data than $\varepsilon_p^{\min} = 0.5$. Table 3.3 reports the optimal values of the model parameters used in the current study.

Table 3.3: TFM model parameters used in the simulations

Parameter	Value
Particle-particle restitution coefficient, e	0.88
Particle-wall restitution coefficient, e_w	0.90
Tangential restitution coefficient, β_0	0.33
Specularity coefficient, ϕ_w	0.03
Wall friction coefficient, μ_w	0.30
Minimum frictional particle volume fraction, $\varepsilon_p^{\min}$	0.60
Maximum packing limit, $\varepsilon_p^{\max}$	0.64

3.3.3 Geometry and mesh

The computational domain was taken to be a 3D thin fluidized bed with dimensions listed in Table 2.1. There are several studies in the literature that attempt to address the effect of mesh on the numerical simulation of fluidized beds. For example, Agrawal et al. [52], Andrew IV et al. [53], and Igci et al. [54] performed "highly resolved" simulations of a flow in a small periodic domain and found that a grid size of $8.3d_p$ was sufficient to capture all the spatiotemporal structures that they needed to develop sub-grid scale models. Wang in [55] and [56] also studied a 2D bed using a grid size of $7d_p$ and $8.3d_p$, respectively, to perform a "high-resolution Eulerian simulation".

Given the current state of the art described above, in this study, a grid of 280×120×6 cells was used in the axial, longitudinal, and lateral directions, respectively. Here, the axial, longitudinal, and lateral directions are aligned with the y, x, and z axes, respectively. This resolution, which corresponds with $5.3d_p$, was found sufficient to capture the meso-scale structures without using any sub-grid scale model and qualitatively reflected the experimental data. Following Parmentier et al. [87], who performed a grid study on a dense fluidized bed with a flow configuration roughly similar to the current study, the effect of grid size is negligible when Δ^*, a dimensionless grid size, is smaller than 0.04. Here, $\Delta^* = \dfrac{\Delta}{L}\sqrt{\dfrac{L}{\tau_p^{St} u_{y,g_{@in}}}}$ and Δ, L, and $u_{y,g_{@in}}$ are the grid size, width of the bed, and superficial gas velocity at the inlet, respectively, with $\tau_p^{St} = \rho_p d_p^2/18\mu_g$, the particle response time based on the Stokes law. In this study, the grid size is $\Delta = 2.5 \times 10^{-3}$ m, leading

to a value of $\Delta^* = 0.005$, which is lower than the limiting value. Further refinement of the grid size required time steps on the order of 10^{-7} s, which in turn, resulted in excessively long run times.

3.3.4 Post-processing

The numerical model predicts such output properties as the particle volume fraction, the gas pressure, the velocity components of each phase, and the granular temperature of the particle phase. Python subroutines were developed to post-process these properties and calculate spatially and time-averaged quantities of interest, such as the phasic velocity profiles, particle-flow patterns, 3D bubble characteristics, power spectral density (PSD) of the gas pressure, and resolved-scale particle Reynolds stresses. The variables were time-averaged over the 100 seconds of simulation after the first 10 seconds so as to minimize any transient start-up effects.

3.4 Results and discussion

In order to assess the validity of the two-fluid model, the numerical results are compared with the experimental measurements of Laverman et al. [83], where Particle Image Velocimetry (PIV) coupled with Digital Image Analysis (DIA) were used to study the behavior of glass particles at different superficial gas velocities inside a thin fluidized bed. The time-averaged particle velocity at different heights above the distributor were measured.

Before investigating the effect of boundary conditions on the mean flow, it is helpful to look at the profiles of the wall momentum flux (shear stress) and granular energy flux predicted by each wall BC. The wall shear stress and granular energy flux collapse onto a single curve when the normalized wall shear stress and wall granular energy flux are plotted versus the normalized wall slip velocity, as shown in Figure 3.1. We note that in Figure 3.1, only the kinetic-collisional contribution of the wall shear stress, represented by S, is considered. Figure 3.1 indicates that the difference in the predicted values of the wall fluxes by the Jenkins–Louge and Schneiderbauer et al. models is minimal. In contrast, the Johnson–Jackson BC predicts quite different values for the wall momentum and granular energy fluxes compared to the other two wall BCs.

3.4.1 Effect of wall BC on the bed dynamics

The time-averaged axial particle velocity is calculated as follows:

$$u_{y,p}^{\text{avg}} = \frac{\overline{\varepsilon_p u_{y,p}}}{\overline{\varepsilon_p}}, \tag{3.7}$$

where $\bar{\cdot}$ indicates time-averaging.

Figure 3.2 shows the time-averaged axial velocity profiles of the particles at two different heights. This figure compares the experimental data of Laverman et al. [83] and the numerical results of 3D simulations. At a height of 10.5 cm (Figure 3.2a), there is a downward particle-flow in the near-wall region, i.e., $x < 4$

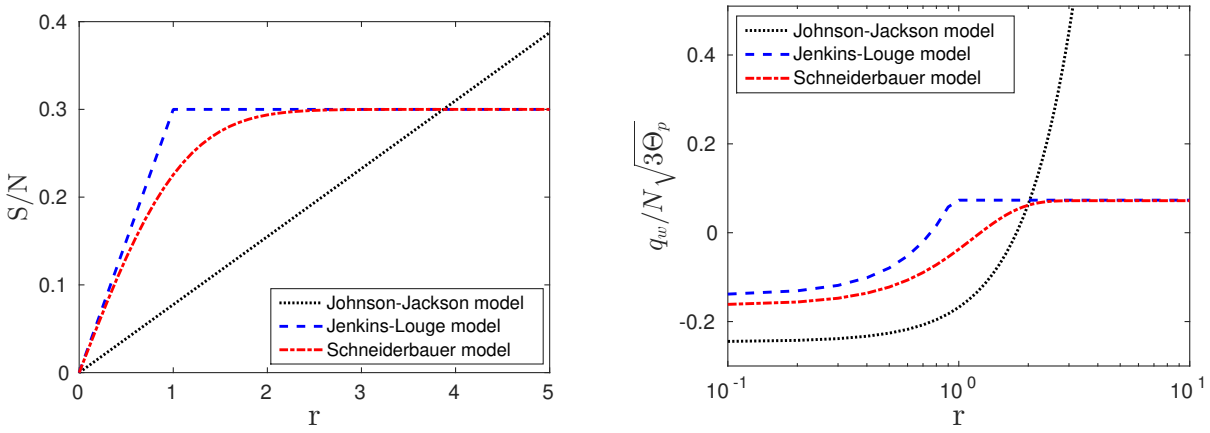

(a) wall momentum flux **(b)** wall granular energy flux

Figure 3.1: Variation of the normalized (a) wall shear stress and (b) wall granular energy flux with the normalized wall slip velocity predicted by each wall BC.

cm and $x > 26$ cm, and in the central region, i.e., 11 cm $< x <$ 18 cm. In the near-wall region, all three BCs predict a similar downward flow. However, in the central region quite different profiles are predicted by each wall BC. To quantify the differences between the model predictions and the experimental data, the root-mean-square error, E_{rms}, is calculated by,

$$E_{\text{rms}} = \sqrt{\frac{\sum_{i=1}^{n} \left(V_{\text{num},i} - V_{\text{exp},i}\right)^2}{n}},$$

where V_{num}, V_{exp}, and n, represent the predicted axial particle velocity, experimentally measured axial particle velocity, and number of samples, respectively. Note that, E_{rms} is a global metric that quantifies the overall difference between the numerical results and their experimental counterpart. At the height of 10.5 cm, the values of E_{rms} for the Johnson–Jackson, Jenkins–Louge, and Schneiderbauer et al. models are 1.7 cm/s, 1.0 cm/s, and 1.7 cm/s, respectively. At a height of 24.5 cm, the experimental data show a downward flow in the region $x <$ 8 cm and $x >$ 21 cm. In the region in between, i.e., the central region, an upward flow is observed with a peak located near the center. The discrepancy between the predicted velocity profiles and their experimental counterpart in the near-wall region at this height could be attributed to the collective deficiency of the modeling, e.g., the interaction of the BC with the particle stress model. At this height, the values of E_{rms} for the Johnson–Jackson, Jenkins–Louge, and Schneiderbauer et al. BCs are 3.1 cm/s, 2.7 cm/s, and 3.2 cm/s, respectively. This indicates that the lowest value of E_{rms}, at both heights, corresponds to the numerical results predicted by the Jenkins–Louge wall BC. We note, however, this by itself is not sufficient to conclude that the Jenkins–Louge wall BC is superior to the other two BCs. Overall, Figure 3.2 indicates that the system of governing equations is sensitive to the type of particle-wall BC. Although all three wall BCs used in this study are physically meaningful and have been applied extensively by other researchers, it appears that they produce somewhat different particle-flow patterns, especially in the central

region of the bed. In this regard, it is helpful to look at the overall time-averaged velocity pattern inside the bed.

Figure 3.3 shows the time-averaged velocity field from the experiment and as predicted by each wall BC at a plane located at $z = 0.375$ cm. Figure 3.3 also shows the corresponding time-averaged particle volume fraction contours in the background. Qualitatively, it appears that the Johnson–Jackson BC has predicted a slightly higher particle volume fraction in the region 5 cm $< x <$ 25 cm and 10 cm $< y <$ 28 cm. Regarding the flow pattern, as shown in this figure, the overall particle motion is governed by the formation of two elongated vortices of opposite sign. Table 3.4 reports the locations of the centers of the two vortices as predicted by the experimental data and each wall BC. Note that the first and second numbers in each ordered pair indicate the x and y coordinates, respectively. This table also shows the net distance between the predicted vortex location for each wall BC and its experimental counterpart. It is observed that the centers of the vortices predicted by the Jenkins–Louge and Schneiderbauer et al. BCs are closer to the measured data than those predicted by the Johnson–Jackson BC. All three BCs also predict a similar downward particle-flow for the high-density near-wall region. However, each BC predicts quite different flow patterns in the central region. For example, in the lower part of the bed, i.e., $y < 10$ cm, a stronger upward flow is predicted by the Johnson–Jackson BC compared to the other two BCs. Also, qualitatively, it appears that the flow pattern predicted by the Jenkins–Louge BC is more symmetric compared to the other two BCs in the central region of the bed. The reason might be attributed to the dominant influence of bubbles on the the particle motion in the central region. Because the bubble formation is affected by the wall BC, e.g., through the mean kinetic energy of the particles dissipated at the wall, different flow patterns might be expected from each wall BC in the central region.

Table 3.4: Location of the vortices for experimental data and different wall BCs; units are cm.

BC type	Center of the left vortex	Center of the right vortex	Net distance to the exp. left vortex	Net distance to the exp. right vortex
Exp. data [83]	(7.5, 29.6)	(22.0, 30.3)	–	–
Johnson–Jackson BC	(7.4, 27.4)	(22.7, 28.0)	2.2	2.4
Jenkins–Louge BC	(7.6, 28.6)	(21.8, 28.5)	1.0	1.8
Schneiderbauer et al. BC	(7.3, 28.6)	(21.9, 28.5)	1.0	1.8

Figure 3.4 shows the time-averaged particle holdup along the bed as predicted by each wall BC. Although there is no precise criterion for defining the expanded bed height, for the current study, a particle volume fraction of 0.2 is used as the threshold value to determine the time-averaged height of the bed. As shown in Figure 3.4, the BCs of Jenkins–Louge and Schneiderbauer et al. predict quite similar particle holdup profiles and a bed height of 33.7 cm. The Johnson–Jackson BC predicts a somewhat under-expanded bed with a height of 33.1 cm. A reduction in the bed expansion, as predicted by the Johnson–Jackson BC compared to the other two BCs, may be attributed to the energy level of the bubbles. Here, a bubble is understood

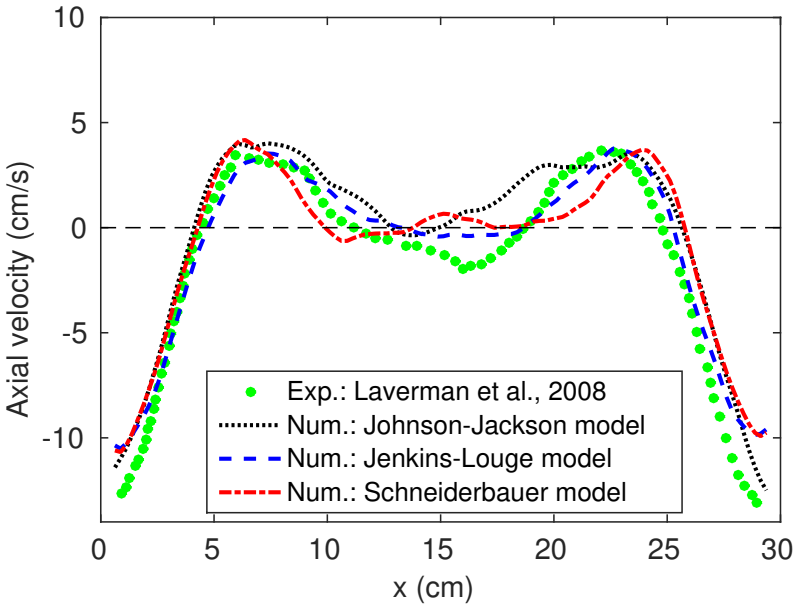

(a) $h = 10.5$ cm

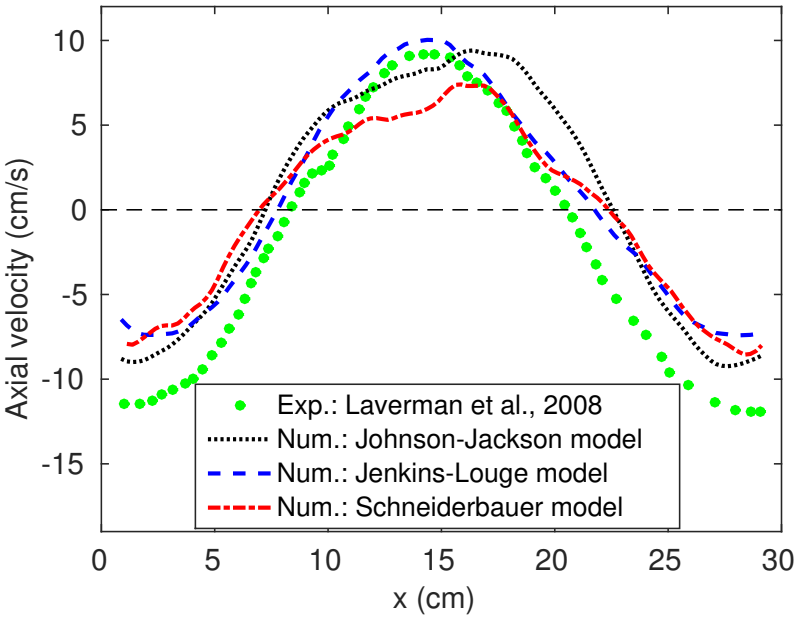

(b) $h = 24.5$ cm

Figure 3.2: Time-averaged axial particle-velocity profiles predicted by various wall BCs at different heights.

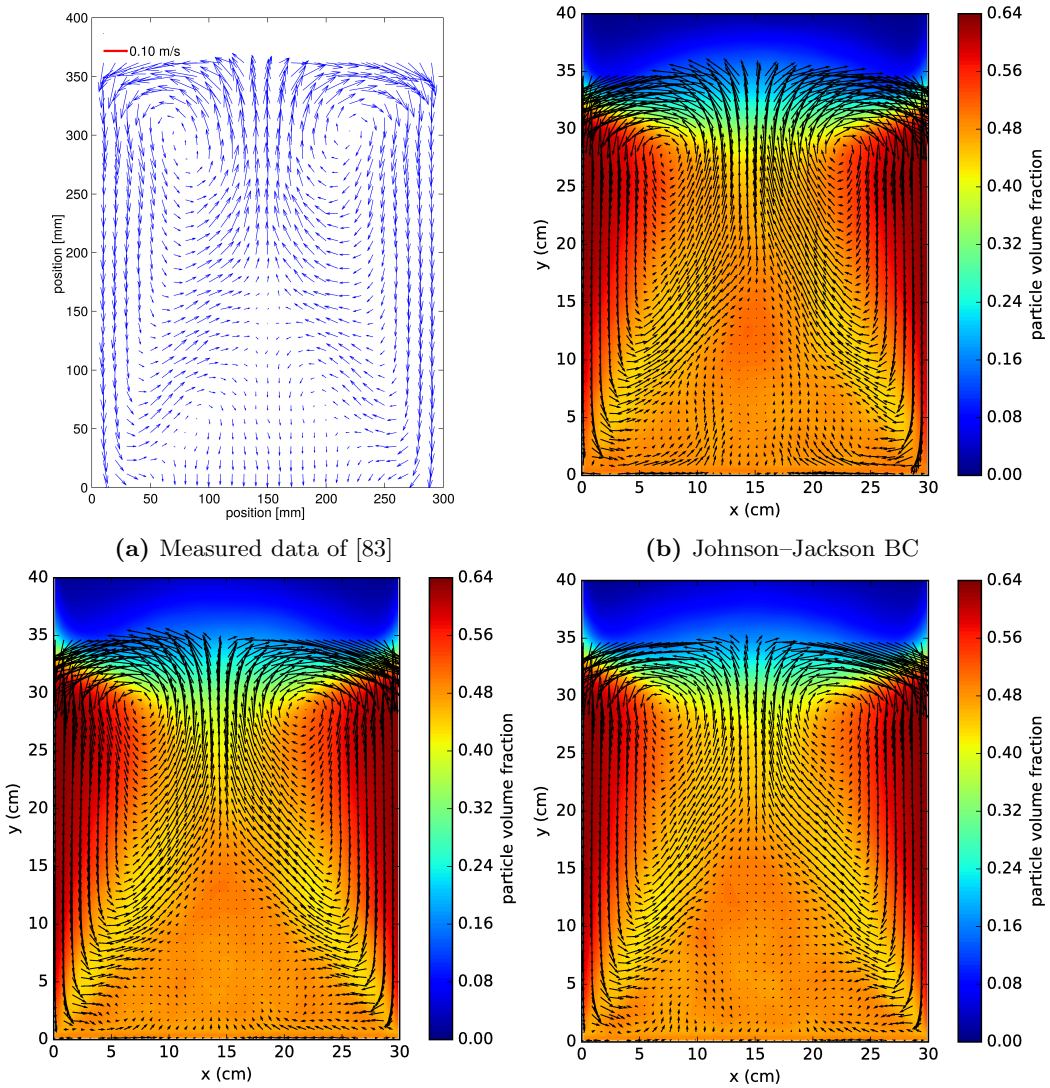

(a) Measured data of [83]

(b) Johnson–Jackson BC

(c) Jenkins–Louge BC

(d) Schneiderbauer et al. BC

Figure 3.3: Time-averaged particle volume fraction and particle velocity field: comparison between measured data and numerical results predicted by different models.

to be a localized region of gas, typically moving as an entity through the particulate phase. In this context, the energy level of a bubble corresponds to the level of bubble activity associated with the gas pressure fluctuation, that induces enhanced resolved-scale velocity fluctuations in the particle flow. It is shown in Section 3.4.3 that the bubbles predicted by the Johnson–Jackson BC are more vigorous, due to stronger gas pressure fluctuations, than those predicted by the other two BCs. More vigorous bubbles tend to bring particles closer to each other, leading to a decrease in the level of the particle fluctuating energy, i.e., granular temperature. As a result, particles are less granular, resulting in a less expanded bed. Figure 3.5 shows the time-averaged granular temperature predicted by each wall BC at the height of 24.5 cm. It illustrates that the Johnson–Jackson BC, as explained above, predicts a lower level of granular energy compared to that predicted by the other two BCs. It is noteworthy that the Jenkins–Louge BC also predicts a more symmetric profile compared to that of the BC of Schneiderbauer et al.

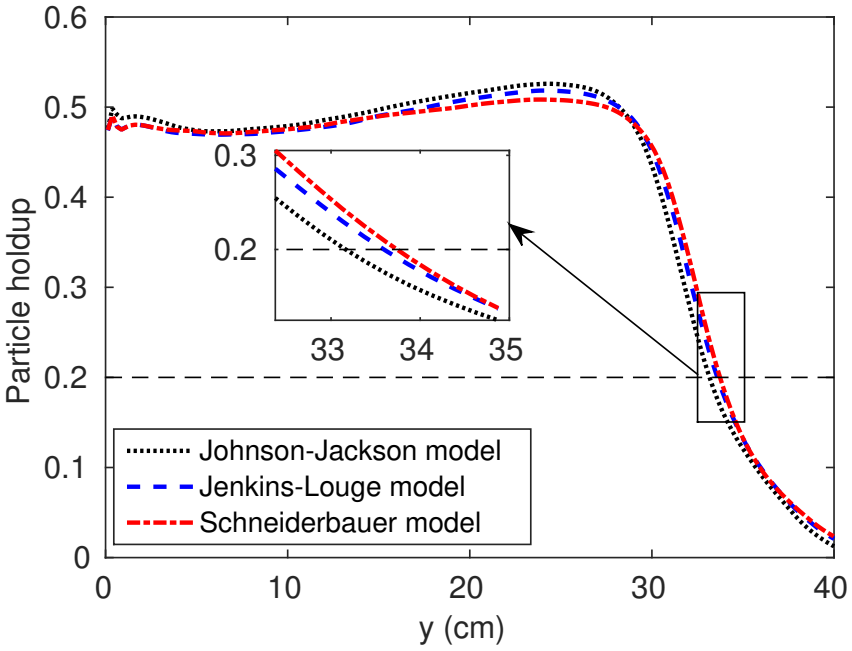

Figure 3.4: Particle holdup profiles predicted by different wall BCs.

Figure 3.6 shows the spatially-averaged variance of void fraction along the bed to characterize the meso-scale variations of the local instantaneous void fraction corresponding to the bubbles. This figure indicates that the variance of the void fraction increases with the height and reaches a maximum value at approximately the bed surface. Figure 3.6 also shows that the Jenkins–Louge and the Schneiderbauer et al. BCs predict almost similar profiles in the region where the maximum of void fraction variance takes place, whereas the Johnson–Jackson BC predicts a quite different profile in that region.

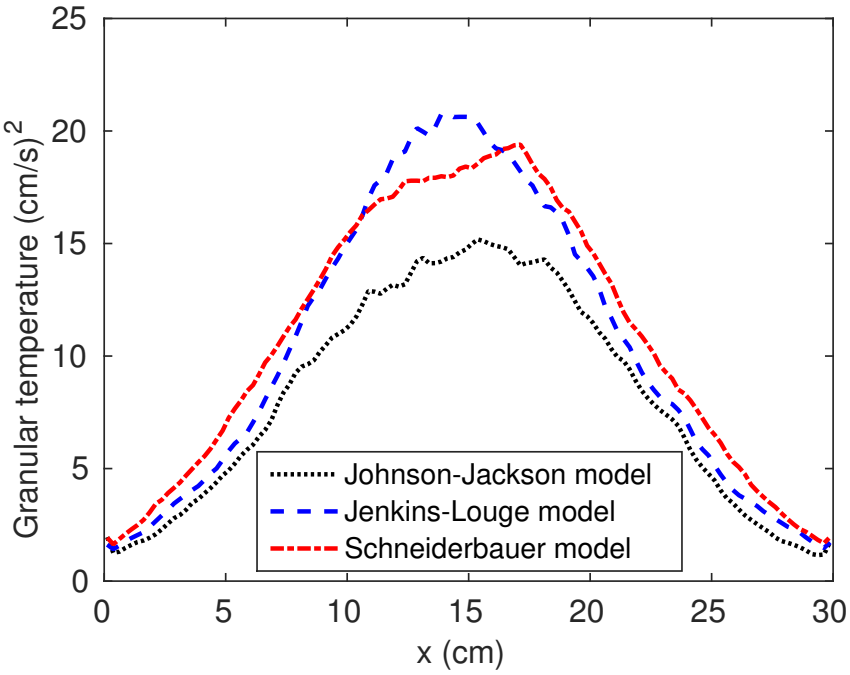

Figure 3.5: Time-averaged granular temperature, predicted by different wall BCs, at the height of 24.5 cm.

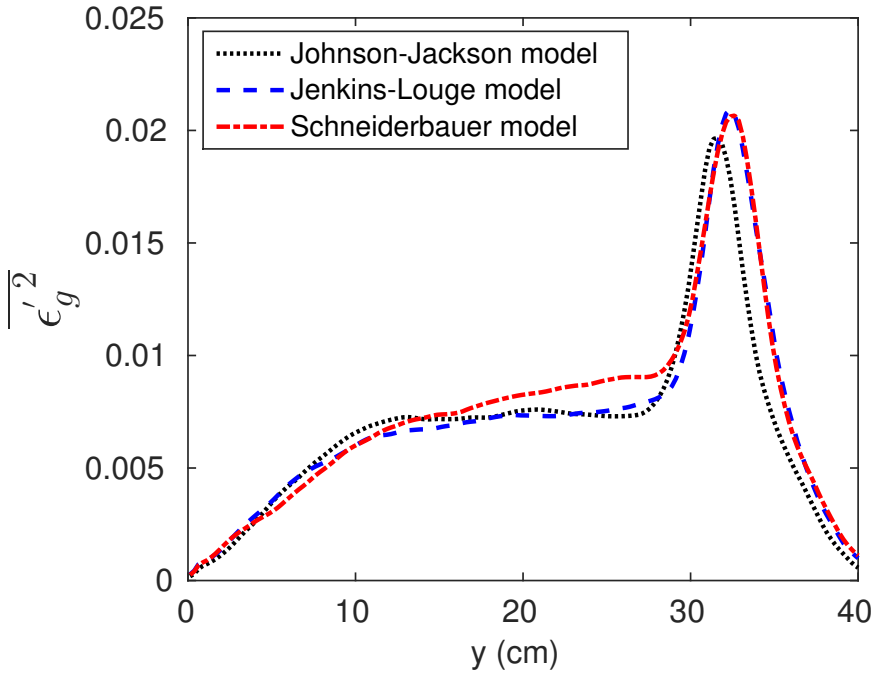

Figure 3.6: Profile of the variance of void fraction along the bed predicted by different wall BCs.

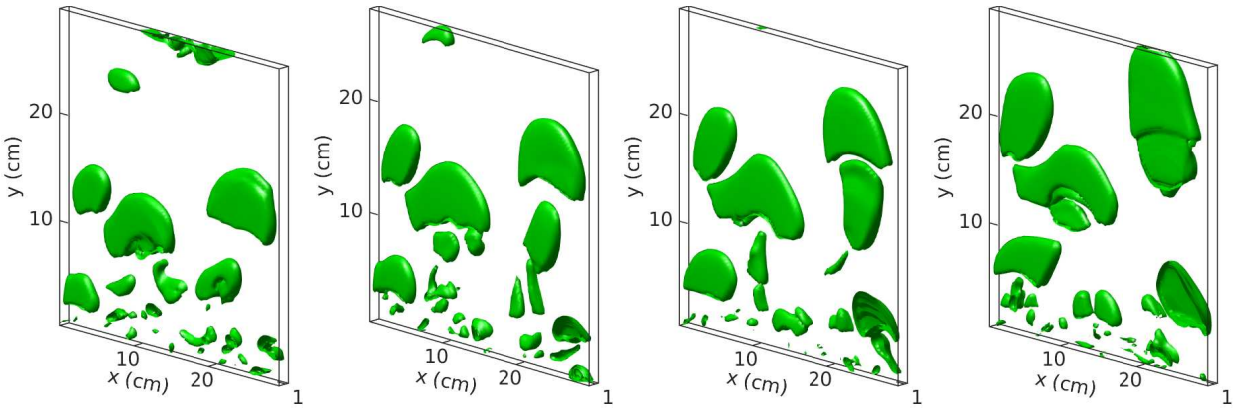

Figure 3.7: Instantaneous snapshots of bubble contours in the bed for four successive instants from left to right; predicted by the Jenkins–Louge wall BC.

3.4.2 Effect of wall BC on the bubble characteristics

The inlet gas velocity in the present study is 2.5 times the minimum fluidization velocity, and the flow corresponds to the bubbling regime. Figure 3.7 shows the 3D visualization of the instantaneous bubble structures at four consecutive times as predicted by the Jenkins–Louge wall BC. Although there is no precise criterion for defining the extent of a bubble, for the current study, a gas fraction of 0.8 has been used as the threshold value to determine the bubble boundary. Figure 3.7 illustrates that the small bubble structures, which originate in the bottom and near-wall regions of the bed, coalesce to form the large bubbles structures. As bubbles rise through the bed, they tend to migrate towards the centerline and eventually burst at the bed surface.

In order to assess the bubble characteristics quantitatively, the bubble rise velocity, equivalent bubble diameter, and average number of bubbles have been calculated using the 3D Matlab code developed by Bakshi et al. [88]. The code, based on the void fraction data, applies a void-fraction threshold and bubble-linking method to identify individual bubbles. The code then tracks bubbles across successive time frames to calculate time-averaged bubble statistics. Approximating individual detected bubbles by a spherical shape, the equivalent bubble diameter is calculated from $D_e = \sqrt[3]{6V_b/\pi}$, where V_b, is the volume of the bubble.

Figure 3.8 shows the equivalent bubble diameter and bubble rise velocity along the bed. Figure 3.8a illustrates that, as the bubbles move upward through the bed, they merge and form larger bubbles. This figure also indicates that, overall, the Johnson–Jackson BC predicts smaller bubbles. This relates to the more vigorous bubbles predicted by the Johnson–Jackson BC. More energetic bubbles, as discussed in Section 3.4.1, lead to a lower granular temperature (Figure 3.5) and a higher average particle volume fraction; see discussion of Figure 3.3b. This leads the bubbles to experience more resistance to their expansion and thus have a smaller size. Figure 3.9 shows the size distribution of bubbles predicted by each wall BC. In summary, it appears that the Johnson–Jackson BC predicts a larger number of smaller bubbles compared to those predicted by the other two BCs. As discussed previously, the small bubble structures are formed near the bottom of the bed.

We have seen from Figure 3.3b that the stronger upward particle-flow in the lower part of the bed can be attributed to the larger number of bubbles as predicted by the Johnson–Jackson BC. No significant difference is observed between the predictions of the BCs of Jenkins–Louge and Schneiderbauer et al. in Figure 3.9.

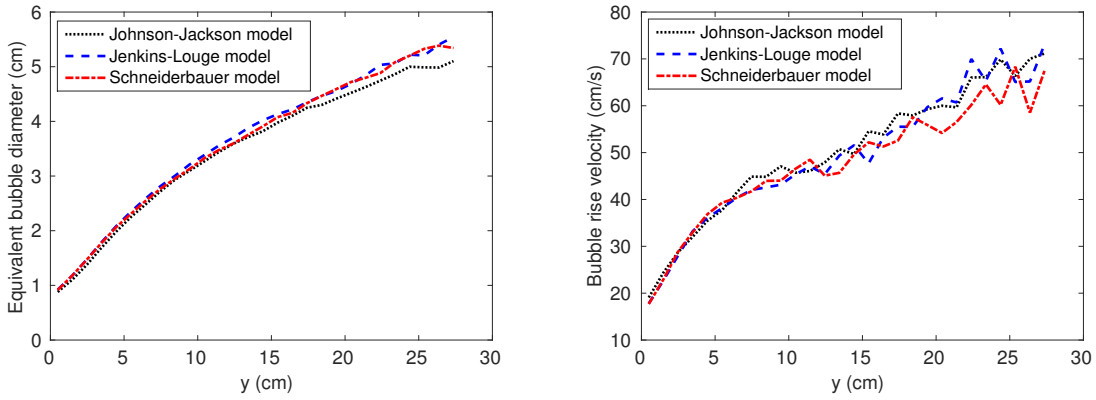

(a) Average bubble size **(b)** Bubble rise velocity

Figure 3.8: Comparison between different wall BCs: (a) Average bubble size and (b) Bubble rise velocity vs. height.

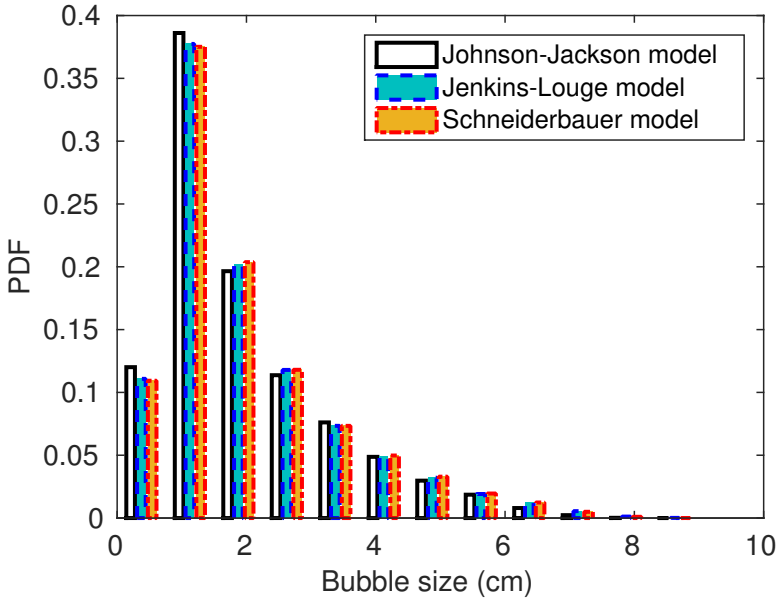

Figure 3.9: Bubble size distribution predicted by different wall BCs.

3.4.3 Effects of wall BC on the gas pressure fluctuations

The dynamics of the bed is strongly influenced by the upward motion of bubbles through the bed. The chaotic motion of bubbles introduces complex unsteady flow patterns. To gain a better insight into such unsteady flow patterns, it is helpful to look at the Power Spectral Density (PSD) of the gas pressure field. To calculate

the PSD of the pressure signals, the value of absolute pressure was recorded at intervals of approximately 10^{-4} s at a height of 10 cm. Because the MFIX code uses a variable time-step method, pressure data were recorded at irregular time intervals. To obtain a uniform time intervals of 10^{-4} s, a Chebyshev polynomial of order 10 was used to interpolate the data. Figure 3.10 shows the PSD of pressure signals predicted by different wall BCs in the frequency domain. All three BCs predict roughly the same natural frequency of approximately 8 Hz. It can be seen that the Johnson–Jackson BC predicts a stronger intensity in the gas pressure fluctuations, i.e., by approximately one order of magnitude, for frequencies higher than 100 Hz, suggesting more vigorous bubbles compared to the results predicted by the other two BCs. More vigorous bubbles may also be coupled to a larger resolved-scale particle Reynolds stress, discussed in the Section 3.4.4. For frequencies between 200 to 1000 Hz, the BC of Schneiderbauer et al. predicts a relatively stronger intensity in the gas pressure signal compared to the Jenkins–Louge BC. To the best of our knowledge, this is the first time that a PSD of pressure data is calculated for frequencies higher than 500 Hz. The PSD analysis does not show the classical small-scale turbulence behavior, indicating that gas turbulence, if any, is damped by the inertia of particles in the bubbling bed.

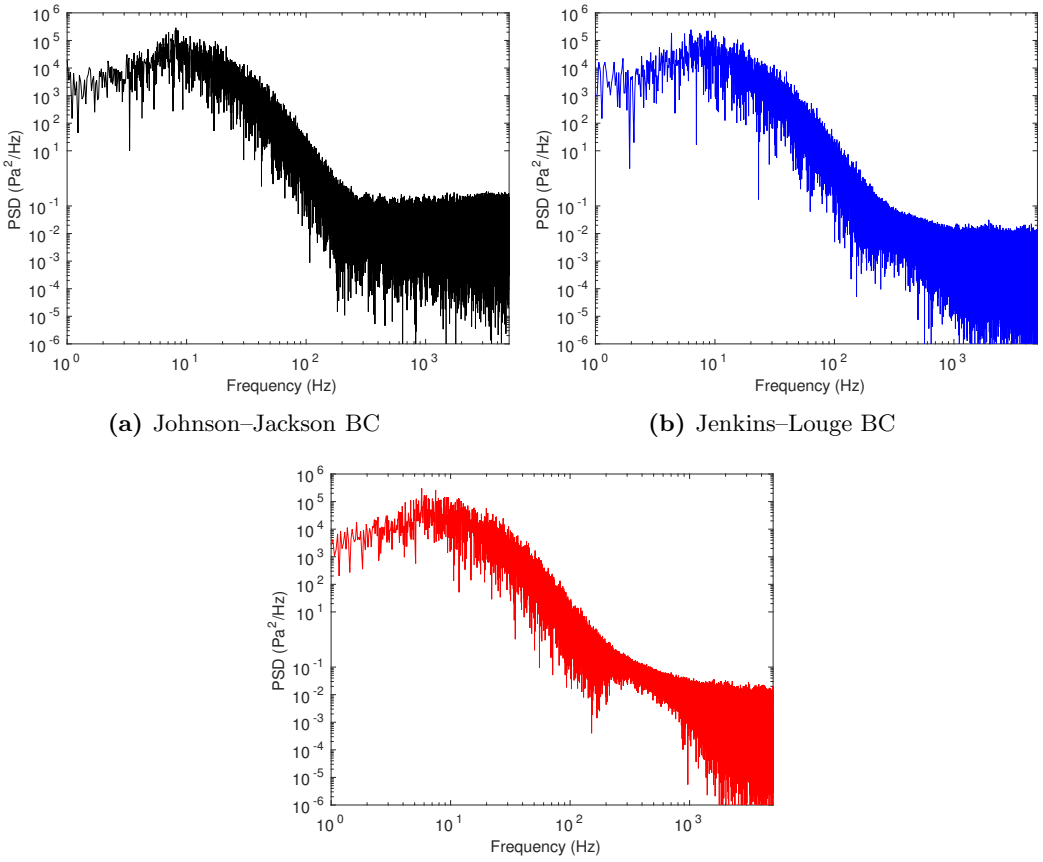

(a) Johnson–Jackson BC

(b) Jenkins–Louge BC

(c) Schneiderbauer et al. BC

Figure 3.10: PSD of pressure signals predicted by different wall BCs.

3.4.4 Effect of wall BC on the "resolved-scale" particle Reynolds stress

In bubbling beds, particles extract energy from the mean kinetic energy of the gas flow to produce kinetic energy that corresponds to the fluctuating motions at the level of individual particles, i.e., granular temperature. Therefore, granular temperature represents the small-scale fluctuating motions of particles that might have a small contribution to the mixing process in the bed. On the other hand, the chaotic motion of bubbles leads to large-scale fluctuations at the level of collections of particles that contribute to the mixing process in the bed. Once the instantaneous particle velocity field is obtained, the resolved-scale particle Reynolds stress per unit bulk density can be calculated as

$$\overline{u_i' u_j'} = \frac{1}{T} \int_{t_0}^{t_0+T} (u_i - \overline{u_i})(u_j - \overline{u_j})\, dt, \tag{3.8}$$

$$\overline{u_i} = \frac{1}{T} \int_{t_0}^{t_0+T} u_i\, dt. \tag{3.9}$$

Figure 3.11 shows the contours of time-averaged particle normal Reynolds stress in the axial direction, calculated at the same plane as in Figure 3.3. All three components of Reynolds normal stress are calculated, and it is found that $\overline{u_y' u_y'} > \overline{u_x' u_x'} > \overline{u_z' u_z'}$. For brevity, only the contours of the dominant component, $\overline{u_y' u_y'}$, are plotted. Compared to Figure 3.5, this figure illustrates that the resolved-scale fluctuations are much more intense than the particle-scale fluctuations and hence are the main mechanism of mixing inside the bed. Figure 3.11 indicates that the resolved-scale Reynolds normal stress predicted by the Johnson–Jackson BC is larger than that predicted by the other two BCs. As discussed in the previous section, the larger resolved-scale particle Reynolds stress is a result of the more vigorous bubble activity predicted by the Johnson–Jackson BC. We note that all three BCs predict the largest fluctuations to occur at 30 cm $< y <$ 35 cm, corresponding to the region of fluctuations in the bed surface. It also appears that the Johnson–Jackson BC has predicted more extensive regions of large $\overline{u_y' u_y'}$ compared to the other two BCs.

A significant feature of fluidized beds, as far as applications are concerned, is the enormous mixing that takes place in them and causes increased rates of momentum, heat, and mass transfer. Therefore, it is important to identify and visualize the regions in the bed where on average most of the mixing takes place. It is well-established that in incompressible single-phase turbulent flows, Reynolds shear stresses are mainly responsible for the mixing. Similarly, contours of particle Reynolds shear stress, $\overline{u_x' u_y'}$, reveal the regions of dominant mixing in the bed. Figure 3.12 shows the contours of time-averaged $\overline{u_x' u_y'}$ in the same plane as in Figure 3.11. It shows that there are two high-mixing regions near the bed surface, 30 cm $< y <$ 35 cm. Figure 3.3 suggests that these two regions might be a result of bubbles bursting at the bed surface that direct particles transversely towards the wall from a vertically oriented motion. For lower heights, 20 cm $< y <$ 30 cm, there are also two moderate-mixing regions near the center of the principal vortices depicted in Figure 3.3. In the lower part of the bed, $y <$ 20 cm, there are also two moderate-mixing paths between the high-density regions near the wall and the moderate-density low-velocity region in the lower central region. As discussed above, the Johnson–Jackson BC tends to predict more vigorous bubbles compared to the other two BCs.

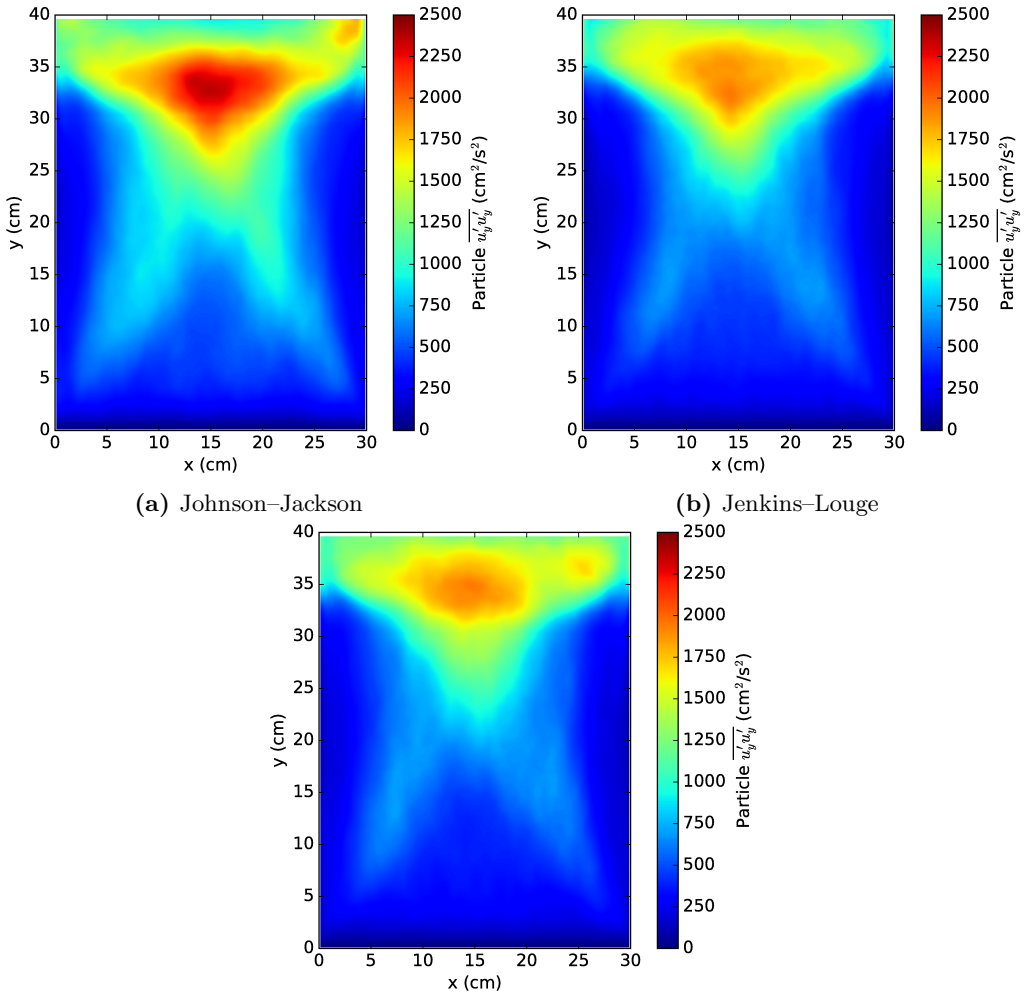

(a) Johnson–Jackson

(b) Jenkins–Louge

(c) Schneiderbauer et al.

Figure 3.11: Time-averaged particle Reynolds normal stress, i.e., $\overline{u_y' u_y'}$, predicted by different wall BCs.

Consequently, more extensive mixing regions are predicted by this BC, specifically in the lower part of the bed. Comparing Figures 3.11 and 3.12 shows that the mixing caused by the normal Reynolds stress is much stronger than the one caused by the shear Reynolds stress. This observation is unlike that observed in incompressible single-phase turbulent flows. However, it is important to note that the particles in the TFM approach are treated as a compressible phase.

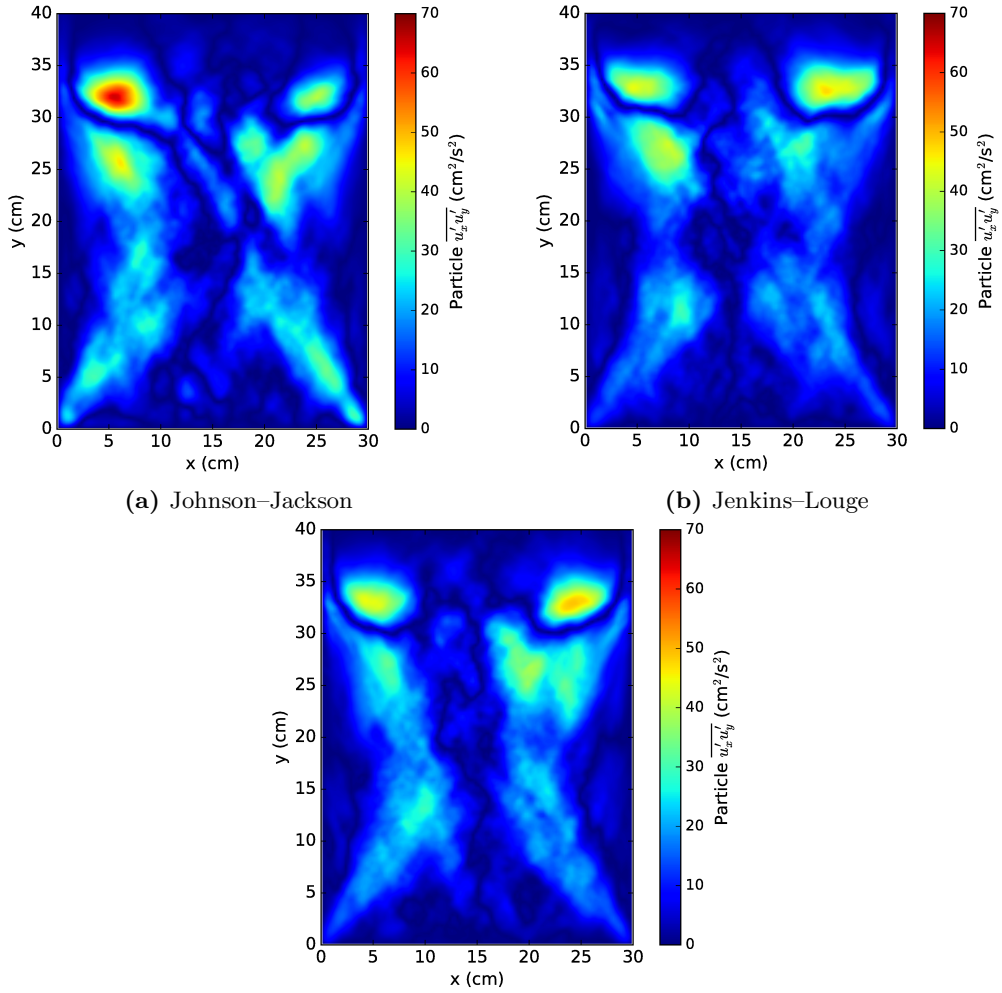

(a) Johnson–Jackson

(b) Jenkins–Louge

(c) Schneiderbauer et al.

Figure 3.12: Time-averaged particle Reynolds shear stress, i.e., $\overline{u_x' u_y'}$, predicted by different wall BCs.

The results of this study indicate that overall the most notable difference in the flow characteristics is predicted by the Johnson–Jackson BC compared to the BCs of Jenkins–Louge and Schneiderbauer et al. Although some differences are observed in the flow structures predicted by these two BCs, they might be insignificant in the overall performance of the bed. We note that the lowest value of the root-mean-square error corresponded to the numerical results predicted by the Jenkins–Louge wall BC. As discussed previously, this by itself is not sufficient to conclude that the Jenkins–Louge wall BC is superior to the Schneiderbauer

et al. BC.

3.5 Conclusion

This study demonstrates the significant role of the particle-wall boundary condition in the prediction of dense gas-particle flows using a two-fluid model. A comprehensive study is performed to assess the effect of three different wall BCs on the structural characteristics of a dense gas-particle flow inside a 3D bubbling bed. The wall BCs considered in this study included the Johnson–Jackson BC [25], the Jenkins–Louge BC [72], and the BC of Schneiderbauer et al. [73].

The paper assessed the ability of the aforementioned particle-wall BCs to predict the hydrodynamics of the bed. The main focus of this study was to perform an in-depth systematic study to compare the effect of these wall BCs on the simulated flow behavior. The paper quantitatively explained some important features of the mechanics of the bubbling beds that have received relatively little attention in the literature. For example, the effect of wall BC on the velocity field, 3D bubble statistics, gas-pressure fluctuations, and particle resolved-scale Reynolds stress were investigated.

To quantify the differences between BC predictions and the experimental data, the value of the root-mean-square error was calculated for each wall BC. It was determined that the lowest value of the root-mean-square error corresponded to the numerical results predicted by the Jenkins–Louge wall BC. Also, it was observed that the Jenkins–Louge BC consistently produced a more symmetric velocity field compared to the other two wall BCs. However, there is a significant discrepancy between the BC predictions and the experimental observation. This discrepancy can be attributed to the collective deficiency of the overall model. Accordingly, one must be cautious in drawing a definitive conclusion.

Overall, the flows predicted by the three wall BCs were structurally similar. However, some specific features differed in a systematic way that were tracked to the effect of wall boundary condition on the bubble behavior. For example, the flow characteristics predicted by the Johnson–Jackson BC were in some ways different from those predicted by the other two BCs. The reason was attributed to the more vigorous bubbles predicted by the Johnson–Jackson wall BC. The more energetic bubbles resulted in a lower level of granular temperature, a less-expanded bed, and more extensive mixing regions inside the bed. It was also found that in bubbling beds the mixing caused by the particle Reynolds normal stress is much stronger than the one caused by the particle Reynolds shear stress.

Acknowledgement

The authors are grateful to the Natural Sciences and Engineering Research Council of Canada (NSERC) for providing financial assistance for this research project. The authors acknowledge Akhilesh Bakshi for making the 3D bubble tracking Matlab code available.

Chapter 4

Energy budget analysis of a dense gas-particle flow inside a fluidized bed

A similar version of this chapter has been submitted as:

- M. R. Haghgoo, D. J. Bergstrom, and R. J. Spiteri. Energy budget analysis of a dense gas-particle flow inside a fluidized bed. *Powder Technol.*, Under Review, 2018.

The first author conducted the simulations, post-processed and analyzed the results, and prepared the first draft of the manuscript. He then worked with the co-authors to discuss the results and finalize the content and form of the manuscript.

Preamble

The energy cascade process plays a significant role in the dynamics of single-phase turbulent flows. Based on the observations in single-phase turbulent flows, it is logical to perform an energy budget analysis on the gas-particle flow inside a bubbling bed to understand the energy exchange between various scales based on a variety of mechanisms. A thorough study of the dynamics of fluidized beds is incomplete without performing an energy budget analysis. The budget analysis helps not only to quantify the relative importance of various terms contributing to the energy cascade, but also to identify the regions in the bed where most of the energy cascade takes place. In this chapter special consideration is given to the three particle-wall boundary conditions discussed in the previous chapter to quantify their contribution to the overall energy cascade.

In this chapter, an equation for the kinetic energy of the mean particle flow is rigorously derived in the context of the TFM approach, and a particle energy budget analysis is performed. The physical implications of various terms in the energy equations are discussed, and their spatial distributions are plotted. This is the first time that an in-depth systematic study is performed that uses a particle energy budget analysis to discuss the dynamics of a three-dimensional bubbling bed.

Abstract

Deeper insight into the complex dynamics of dense gas-particle flows can be gained from the investigation of the energy cascade of the particulate phase. To this end, an in-depth systematic study is performed that uses a particle energy budget analysis to examine the dynamics of a three-dimensional bubbling bed. The budget analysis helps not only to quantify the relative importance of various terms contributing to the energy cascade but also to identify the regions in the bed where most of the energy cascade takes place. It was determined that most of the energy cascade takes place in the central region of the bed, whereas the contribution from the near-wall region was insignificant. It was also found that the flow inside the bed tends on average toward local equilibrium. In this regard, it was determined that the wall boundary conditions significantly affect the local equilibrium.

4.1 Introduction

It is well-established that the dynamics of a bubbling fluidized bed is highly influenced by the bubbles moving up through the bed. Using a non-linear stability analysis, Anderson et al. [89] demonstrated that bubbles form due to a loss of stability of upward traveling waves subject to horizontal perturbations that results in particle clustering. The chaotic motion of bubbles is reminiscent of large-scale eddies in single-phase turbulent flows. However, the cascade of energy in gas-particle flows differs from that in single-phase turbulent flows. In the latter, it is well-known that on average the energy cascades from large to small scales. However, the scenario is more complicated in the case of gas-particle flows, where the meso-scale structures, i.e., bubbles in the current study, emerge initially at small length scales and develop into larger scales. Hence, there is energy transfer from the small to the large scales in addition to a cascade of energy from large to smaller scales [52]. We note that in the context of fluidized beds, the term "cascade" is used to refer to the exchange of energy between various scales based on variety of mechanisms. Goldschmidt et al. [13] performed an energy balance analysis and reported the values of selected terms that appear in the particle mechanical energy equation for both the "Two-fluid model" (TFM) and "Discrete particle model" approaches. Their analysis focused on the comparison between the values predicted by each approach and did not include the contribution of physical walls and dissipation of kinetic energy by frictional stresses in the TFM approach. Using discrete particle simulation and energy balance analysis, Li and Kuipers [90] showed that the competition between particle-particle collision and particle-fluid interaction determines flow structure formation in fluidized beds.

In general, it appears that if more particle kinetic energy is dissipated, bubbles can grow more vigorously, leading to stronger particle clusters. In bubbling beds, there are two principal mechanisms through which the particle kinetic energy is dissipated. In one mechanism, the particle normal and shear stresses extract kinetic energy of the mean particle flow to produce fluctuating energy, i.e., granular temperature. In the other mechanism, some of the kinetic energy of the mean particle flow is dissipated into internal energy through

frictional stresses. Figure 4.1 compares the energy cascade in the particulate phase of a dense gas-particle flow, where the frictional stress plays a significant role, with that in a single-phase turbulent flow.

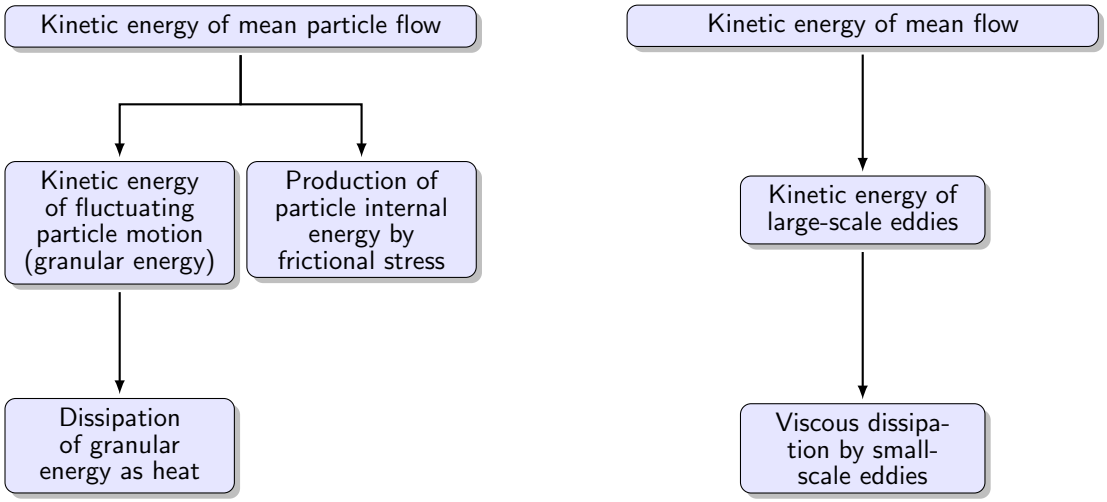

(a) Particulate phase in a dense gas-particle flow **(b)** Single-phase turbulent flow

Figure 4.1: Energy cascade in: (a) the particle phase of a dense gas-particle flow, and (b) a single-phase turbulent flow.

To gain deeper insight into the complex dynamics of bubbling beds, it is helpful to perform a budget analysis on the particle energy equations, i.e., the fluctuating and mean kinetic energy equations, and visualize contours of different terms that appear in the energy equations. This budget analysis helps not only to quantify the relative importance of various terms contributing to the energy cascade but also to identify the regions in the bed where most of the energy cascade takes place. To this end, an equation for the kinetic energy of the mean particle flow is rigorously derived in the context of the TFM approach, and a particle energy budget analysis is performed. The physical implications of various terms in the energy equations are discussed, and their spatial distributions are plotted. To the best of the authors' knowledge, this is the first time that an in-depth systematic study is performed that uses a particle energy budget analysis to discuss the dynamics of a three-dimensional (3D) bubbling bed. Special consideration is given to the contribution of walls to the overall bubble behavior and the energy cascade. In this regard, three different wall boundary conditions (BCs) for the particulate phase that account for the particle slip-velocity and the granular energy flux at the wall are assessed, and the overall contribution to the dissipation of mean particle kinetic energy and random particle fluctuating energy, predicted by each wall model, is determined. The numerical code Multiphase Flow with Interphase eXchanges (MFIX) [11] was used to perform the simulations, using the Eulerian–Eulerian framework. Some additional Fortran subroutines were developed and integrated into the MFIX code to implement the BCs of Jenkins and Louge [72] and Schneiderbauer et al. [73]. Special Python subroutines were developed to perform the energy budget analysis. The results were validated against limited published experimental data of Laverman et al. [83].

It was determined that most of the energy cascade takes place in the central region of the bed, whereas

the contribution from the near-wall region was insignificant. It was also found that the source terms, i.e., dissipation and production, in the granular energy equation played a more significant role in the energy cascade than the convective and diffusive terms. This indicates that on average the flow inside the bed tends toward local equilibrium. In this regard, it was determined that the wall boundary conditions had significant effect on the local equilibrium, and the effect of each wall boundary condition investigated was quantified.

The remainder of this paper is organized as follows. In Section 4.2, an equation for the kinetic energy of the mean particle flow is rigorously derived in the context of the TFM approach, and the physical implications of various terms in the energy equations are discussed. A diagram is provided to summarize how the energy cascades in a dense gas-particle flow. In Section 4.3, the numerical simulation set-up and the values of physical parameters are discussed. In Section 4.4, a particle energy budget analysis is performed, and the time-averaged spatial distribution of different terms contributing to the energy cascade is plotted. In addition, the contribution of wall to the energy cascade is quantitatively discussed.

4.2 Mathematical modeling

The Eulerian–Eulerian TFM, based on the locally averaged equations derived by Anderson and Jackson [7], is used to simulate a dense gas-particle flow inside a 3D thin fluidized bed. The governing/constitutive equations describing the dynamics of such a system can be found in our previous study [20] and accordingly is not repeated here. We note, however, that the current study uses the drag model of Gidaspow [84]. Haghgoo et al. [20] previously showed that the frictional stress proposed by Srivastava and Sundaresan [26] predicted more realistic results than the one proposed by Schaeffer [27]. Therefore, in this study the former frictional model was used to account for the longer-lasting multiple-particle contacts with the frictional stress initiated at a minimum particle volume fraction of $\varepsilon_p^{\min} = 0.6$.

We also note that in the TFM of Anderson and Jackson, a spatial averaging is applied to the carrier phase to obtain the equations for the fluid phase and also to the particles to obtain the "fluid-like" equations for the particle phase. Hence, in this description each point can be occupied simultaneously by both phases, and the fluid phase is not the interstitial fluid but rather an average that is defined throughout the domain. Following Hinze [91], an equation for the kinetic energy of the mean particle-flow can be derived by taking the inner product of the particle momentum equation and the mean particle velocity, resulting in:

$$\underbrace{\frac{D}{Dt}\left(\frac{1}{2}\varepsilon_p\rho_p|\vec{u}_p|^2\right)}_{\text{(I)}} - \underbrace{\varepsilon_p\rho_p\vec{u}_p\cdot\vec{g}}_{\text{(II)}} = \underbrace{-\varepsilon_p\vec{u}_p\cdot\vec{\nabla}P_g}_{\text{(III)}} \underbrace{-\vec{u}_p\cdot\vec{\nabla}P_p}_{\text{(IV)}} + \vec{u}_p\cdot\vec{\nabla}\left(\bar{\bar{\tau}}_{kc}+\bar{\bar{\tau}}_f\right) + \vec{u}_p\cdot\beta\left(\vec{u}_g-\vec{u}_p\right), \tag{4.1}$$

where, ε, ρ, $\vec{u}$, P, $\bar{\bar{\tau}}$, and β represent volume fraction, density, velocity vector, pressure, stress tensor, and inter-phase momentum transfer coefficient, respectively. The subscript p, g, kc, and f stand for the particle phase, gas phase, kinetic/collisional, and frictional, respectively. The first and second terms on the left-hand side of Eq. 4.1 indicate the changes of mean kinetic and potential energies, respectively, for an ensemble of particles per unit volume per unit time. The first and second terms on the right-hand side ((I) and

(II)) express the rate of work, per unit of volume, performed by the gas and particle pressure gradients, respectively. The third term (III) indicates the work, per unit of volume and time, performed by the gradient of the total particle stress, including the kinetic-collisional and frictional stresses. The last term (IV) describes the change in the particle mean kinetic energy, per unit of volume and time, due to drag force between two phases. Eq. 4.1 shows the net contribution of different terms to the mean kinetic energy of the particle-flow; it does not show explicitly which terms correspond to the energy exchange between the mean particle-flow and the fluctuating random motion of particles. It also does not explicitly show how the mean kinetic energy dissipates into internal energy by frictional stress. We note that it is important to calculate the portion of the mean kinetic energy being dissipated because it in turn affects bubble behavior and the overall bed dynamics. To this end, following Hinze [91], each term on the right-hand side of Eq. 4.1 is decomposed into a contribution to the particle total energy, including the mean kinetic energy, the fluctuating energy, and the internal energy, and a contribution to the dissipation of the mean kinetic energy, as follows,

(I): $$\underset{}{\varepsilon_p \vec{u}_p \cdot \vec{\nabla} P_g} = \underset{\text{(i)}}{\vec{\nabla} \cdot (P_g \varepsilon_p \vec{u}_p)} - \underset{\text{(ii)}}{P_g \vec{\nabla} \cdot (\varepsilon_p \vec{u}_p)}.$$

Here, term (i) indicates the rate of work, per unit of volume, performed by the gas pressure, giving a contribution to the particle total energy. Term (ii), that indicates the rate of work done by compression or expansion, is converted into heat. However, this term might be neglected based on the particle phase continuity, assuming that the time derivative part of the particle continuity is negligible compared to term (i).

(II): $$\underset{}{\vec{u}_p \cdot \vec{\nabla} P_p} = \underset{\text{(i)}}{\vec{\nabla} \cdot (P_p \vec{u}_p)} - \underset{\text{(ii)}}{P_{kc} \vec{\nabla} \cdot \vec{u}_p} - \underset{\text{(iii)}}{P_f \vec{\nabla} \cdot \vec{u}_p},$$

where $P_p = P_f + P_{kc}$. Here, term (i) represents the rate of work, per unit of volume, performed by the total particle pressure, contributing to the total energy of the particle phase. Both terms (ii) and (iii) represent the rate of work done by compression or expansion of the particulate phase. Term (ii) extracts some portion of the particle mean kinetic energy to produce particle fluctuating energy, whereas term (iii) converts some part of the mean kinetic energy into heat by frictional pressure.

(III): $$\underset{}{\vec{u}_p \cdot \vec{\nabla} (\bar{\bar{\tau}}_{kc} + \bar{\bar{\tau}}_f)} = \underset{\text{(i)}}{\vec{\nabla} \cdot [\vec{u}_p \cdot (\bar{\bar{\tau}}_{kc} + \bar{\bar{\tau}}_f)]} - \underset{\text{(ii)}}{\bar{\bar{\tau}}_{kc} : \vec{\nabla} \vec{u}_p} - \underset{\text{(iii)}}{\bar{\bar{\tau}}_f : \vec{\nabla} \vec{u}_p}.$$

Here, term (i) describes the rate of work, per unit of volume, by the total particle stress, contributing to the total particle energy. Term (ii) indicates the dissipation of particle mean kinetic energy, per unit time, to produce fluctuating energy by kinetic-collisional stress, whereas term (iii) shows the rate of dissipation of mean kinetic energy into heat by frictional stress.

Based on the above discussion, it appears that terms (II,ii) and (III,ii) are the granular energy production terms that are supplied by the kinetic energy of the mean particle-flow and eventually dissipate into heat, as indicated in Figure 4.1. The granular energy equation is:

$$\frac{D}{Dt}\left(\frac{3}{2}\varepsilon_p \rho_p \theta\right) = -\vec{\nabla} \cdot \left(\kappa_p \vec{\nabla} \theta\right) - P_{kc} \vec{\nabla} \cdot \vec{u}_p + \bar{\bar{\tau}}_{kc} : \vec{\nabla} \vec{u}_p + \Gamma_{slip} - J_{coll} - J_{drag}, \tag{4.2}$$

where θ, κ, Γ_{slip}, J_{coll}, and J_{drag} represent the granular temperature, conductivity of the granular energy, production of granular energy due to gas-particle slip, dissipation of granular energy into heat by inelastic collisions, and exchange of granular energy between two phases due to drag, respectively. Similarly, the particle internal energy includes terms (II,iii) and (III,iii). We also note that the fluctuating energy produced is dissipated into internal energy by inelastic collisions. The particle internal energy equation reads:

$$\frac{D}{Dt}\left(\varepsilon_p \rho_p E_h\right) = -\vec{\nabla}\cdot\left(\kappa_h \vec{\nabla} T\right) - P_f \vec{\nabla}\cdot\vec{u}_p + \bar{\bar{\tau}}_f : \vec{\nabla}\vec{u}_p + J_{coll}, \tag{4.3}$$

where E_h, κ_h, and T represent internal energy and thermal conductivity, and temperature, respectively. Consequently, the particle total energy equation is obtained by adding Eqs. 4.1– 4.3, as follows,

$$\begin{aligned}\frac{D}{Dt}\left[\varepsilon_p \rho_p \left(\frac{1}{2}|\vec{u}_p|^2 + \frac{3}{2}\theta + E_h\right)\right] - \varepsilon_p \rho_p \vec{u}_p \cdot \vec{g} = &-\vec{\nabla}\cdot\left(P_g \varepsilon_p \vec{u}_p\right) - \vec{\nabla}\cdot\left(P_p \vec{u}_p\right) + \vec{\nabla}\cdot\left[\vec{u}_p \cdot \left(\bar{\bar{\tau}}_{kc} + \bar{\bar{\tau}}_f\right)\right] \\ &- \vec{\nabla}\cdot\left(\kappa_p \vec{\nabla}\theta\right) - \vec{\nabla}\cdot\left(\kappa_h \vec{\nabla} T\right) \\ &+ \Gamma_{slip} - J_{drag} + \vec{u}_p \cdot \beta\left(\vec{u}_g - \vec{u}_p\right).\end{aligned} \tag{4.4}$$

Figure 4.2 summarizes the role of each term, as discussed above, in the energy cascade of a dense gas-particle flow.

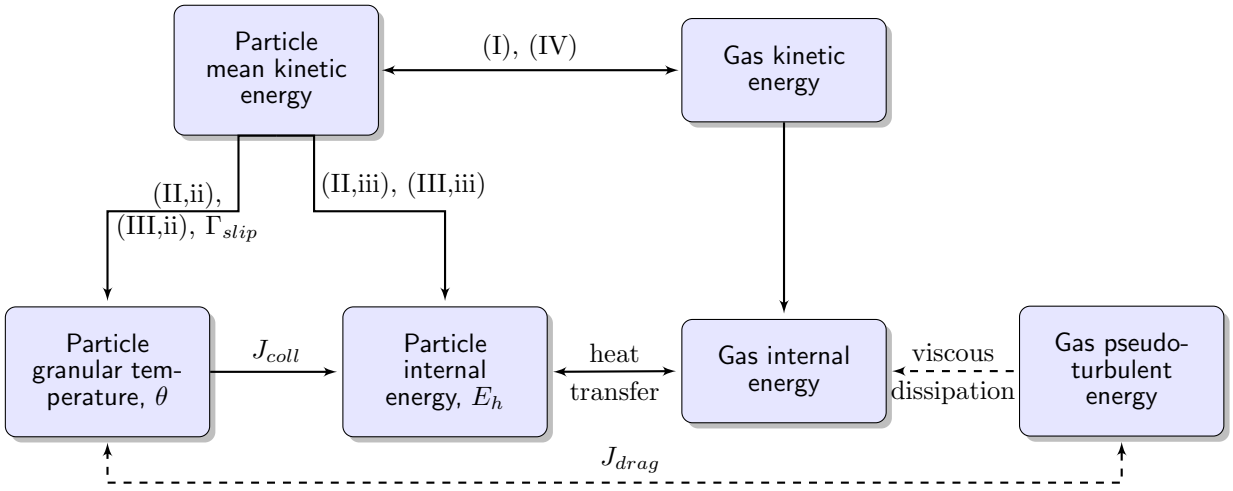

Figure 4.2: Energy cascade in a dense gas-particle flow.

In the context of dense gas-particle flows, where any turbulence of the gas is damped by the inertia of the particles, there is no gas pseudo-turbulent kinetic energy. The pseudo-turbulent kinetic energy is the energy associated with the gas velocity fluctuations caused, for instance, by particle wakes [92]. Figure 4.2 indicates that the drag term makes two contributions to the particle energy cascade: the exchange of (a) mean kinetic energy and (b) granular energy between the gas and particle phases. As discussed by Fox [92], the granular energy is converted into the gas pseudo-turbulent kinetic energy through the drag term, which in turn, dissipates into gas internal energy. This part of energy cascade is shown as a dashed line because the gas fluctuating kinetic energy in dense gas-particle flows is negligible, and therefore no transport equation is

solved to obtain it. In this scenario, the particle granular energy is directly converted into the gas internal energy by viscous dissipation term.

In addition to the aforementioned mechanisms by which the particle-energy cascades inside a bubbling bed, the walls also contribute to the energy cascade. It is thus important to assess the contribution of the wall to the overall particle-energy cascade taking place in the system. The particle wall shear stress extracts kinetic energy from the mean particle-flow and converts it to granular energy and then ultimately to heat. Additionally, the frictional stress at the wall converts the mean kinetic energy to heat. In the current study, three different particle-wall BCs, i.e., the BC of Johnson and Jackson [25], Jenkins and Louge [72], and Schneiderbauer et al. [73], are examined to assess their contribution to the particle-energy cascade and their effect on the overall predicted bed dynamics. The mathematical descriptions for each BC for the wall shear stress and fluctuating energy flux and details about their implementation in the MFIX code can be found in our recent work [2]. We note that for all three BCs, the effect of frictional stress at the wall is taken into account by

$$\vec{\tau}_w^f = -\mu_w N_f \frac{\vec{u}_{sl}}{|\vec{u}_{sl}|}, \tag{4.5}$$

where $\vec{\tau}_w^f$, μ_w, N_f, and $\vec{u}_{sl}$ represent the wall shear stress due to friction between particles and the wall, friction coefficient at the wall, frictional stress normal to the wall, and particle slip velocity vector at the wall, respectively. Therefore, the rate of mean kinetic energy, per unit area, dissipated as heat by frictional stress at the wall is $\mathcal{D}_w^f = \vec{\tau}_w^f \cdot \vec{u}_{sl}$. For particles slipping along the wall, the work performed by the wall shear stress, due to the collisional stress, extracts the mean kinetic energy and converts it to granular energy. As a result, the rate of production of granular energy, per unit area, at the wall is $\mathcal{P}_w^c = \vec{\tau}_w \cdot \vec{u}_{sl}$. Accordingly, given the granular energy flux at the wall, the rate of dissipation of granular energy is obtained by $\mathcal{D}_w^c = \mathcal{P}_w^c - q_w$.

4.3 Numerical simulation

Using the TFM approach of Anderson and Jackson [7], 3D simulations of a bubbling fluidized bed were performed to evaluate the contribution of different terms in the energy cascade. The numerical code MFIX was used to perform the simulations. The MFIX code did not originally include the wall BCs proposed by Jenkins and Louge [72] and Schneiderbauer et al. [73]. Therefore, additional FORTRAN subroutines were developed to implement these wall BCs. Special Python subroutines were developed to perform the energy budget analysis. The numerical results of this study were compared with the experimental measurements of Laverman et al. [83]. Table 4.1 shows the simulation parameters based on the experimental set-up.

All simulations were performed in parallel using 60 cores on an architecture consisting of dual Hex Core Intel Xeon X5650 2.66 GHz with 12 GB of RAM each and running Red Hat Enterprise Linux Server 5.7. The first 100 seconds of the fluidization process are simulated to achieve statistically steady-state solutions. The computational time required to perform a single simulation using the Jenkins–Louge particle-wall BC [72] was approximately 40 days and 14 hours. Extensive 3D simulations (more than 15) were performed to obtain the

Table 4.1: Simulation parameters for comparison with experimental study.

Property	Value
Fluidized bed height	70 cm
Fluidized bed width	30 cm
Fluidized bed thickness	1.5 cm
Initial bed height	30 cm
Particle diameter, d_p	0.485 mm
Particle density, ρ_p	2500 kg m^{-3}
Minimum fluidization velocity, u_{mf}	18 cm s^{-1}
Superficial gas velocity	$2.5u_{mf}$

model parameter values that yielded the most comparable results with the experimental data. Details on the optimal values of the model parameters, numerical methodology, grid study, and CPU-hours of computing to produce the results are available in [2]. Table 4.2 reports the optimal values of the model parameters used in the current study.

Table 4.2: TFM model parameters used in the simulations

Parameter	Value
Particle-particle restitution coefficient, e	0.88
Particle-wall restitution coefficient, e_w	0.90
Tangential restitution coefficient, β_0	0.33
Specularity coefficient, ϕ_w	0.03
Wall friction coefficient, μ_w	0.30
Minimum frictional particle volume fraction, $\varepsilon_p^{\min}$	0.60
Maximum packing limit, $\varepsilon_p^{\max}$	0.64

4.4 Results and discussion

The validity of the TFM for the simulations was established by comparing the numerical results with the limited experimental measurements of [83] in [2]. We note that the variables were time-averaged over the 100 seconds of simulation after the first 10 seconds so as to minimize any transient start-up effects. Haghgoo et al. [2] showed that the Jenkins–Louge particle-wall boundary condition [72] predicts the bed dynamics somewhat better than the more widely used boundary condition of Johnson–Jackson [25]. Therefore, in this study the former particle-wall boundary condition was used to plot the contours of different terms involved in the energy cascade. At the bed inlet, a constant velocity with a flat profile was imposed for the gas phase,

whereas the particle velocity was set to zero.

Figure 4.3 shows the time-averaged velocity field from the experiment and as predicted by the Jenkins–Louge BC in a plane located at $z = 0.375$ cm [2]. Figure 4.3 also shows the corresponding time-averaged particle volume fraction contours in the background. This figure indicates that the overall particle motion is governed by the formation of two elongated vortices of opposite sign.

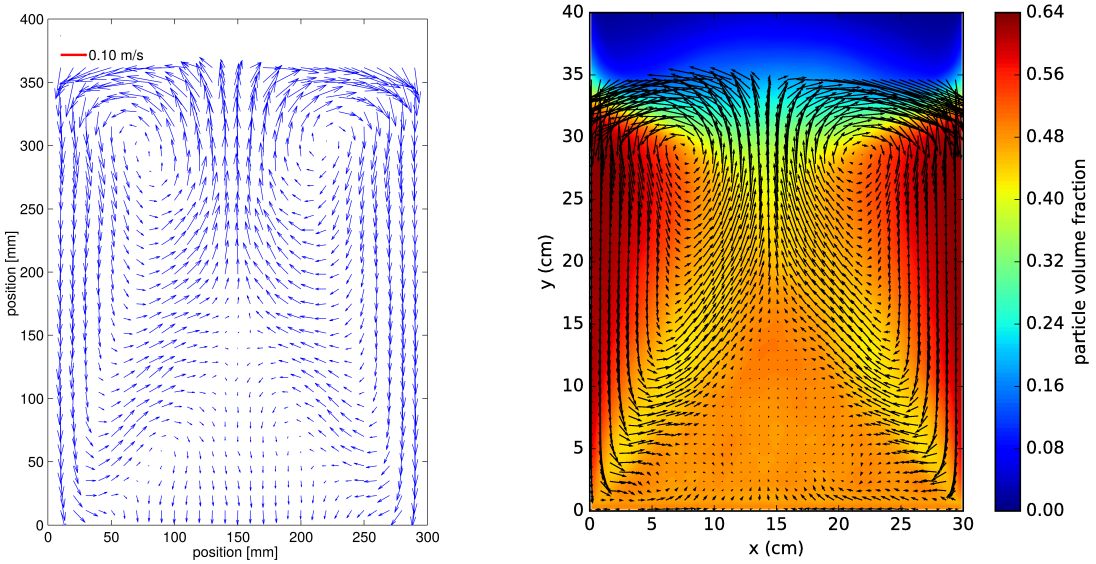

(a) Measured data of [83] **(b)** Jenkins–Louge BC

Figure 4.3: Time-averaged particle volume fraction and particle velocity field: comparison between measured data and numerical result predicted by the Jenkins–Louge BCs [2].

As discussed previously, it is helpful to look at the time-averaged contours of various terms contributing to the energy cascade. Recall from Figure 4.2, terms (I) and (IV) represent the rate of mean kinetic energy exchange between two phases by the gas pressure gradient and drag coupling terms. The first term corresponds to the work performed by reaction on the particles of large scale pressure gradients in the fluid, whereas the second term corresponds to the work performed by drag. Overall, the mean kinetic energy of particles is supplied by the mean kinetic energy of the carrier phase through the work performed by the large-scale pressure gradients and drag force. Figure 4.4 shows the time-averaged spatial distribution of work, per unit time, performed by these terms in the same plane as in Figure 4.3.

In the dilute gas-particle flow, the relative importance of term (IV) is determined by the mass loading [92]. However, Figure 4.4 indicates that both terms contribute almost equally to the energy cascade in dense gas-particle flows. This figure depicts regions in the bed where the two phases strongly interact with each other. It appears that, on average, most of the energy exchange between two phases occurs in the central regions of the bed located away from the walls and bottom inlet. We note that the dominant values of energy exchange correspond to the region where two principal upward streams of particles engage each other (10 cm $< x <$ 20 cm and 18 cm $< y <$ 28 cm) as shown in Figure 4.3. As mentioned previously, the drag

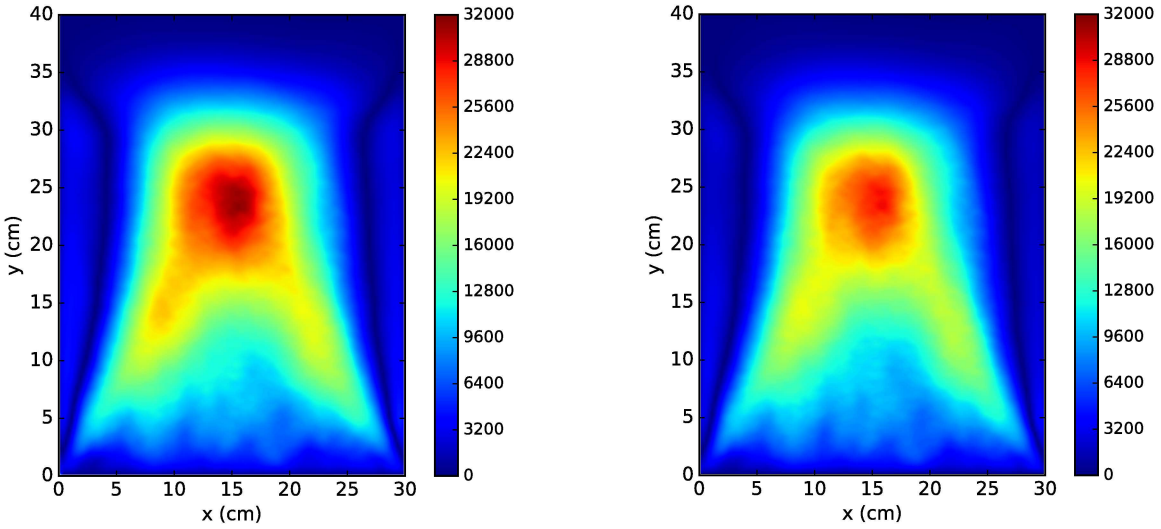

(a) Term (I) **(b)** Term (IV)

Figure 4.4: Time-averaged contour plots of the energy exchange rate between two phases by (a) term (I), i.e., gas pressure gradient and (b) term (IV), i.e., drag. The color-bar values are in $\frac{\mathrm{g}}{\mathrm{cms}^3} = 10^{-1}\frac{\mathrm{J}}{\mathrm{m}^3\mathrm{s}}$.

term also makes a second contribution to the energy exchange between phases by converting the particle fluctuating energy into internal energy of the gas phase. Figure 4.5 shows the time-averaged contours of the corresponding term, i.e., J_{drag}. A comparison of Figures 4.4 and 4.5 indicates that the contribution of drag to the energy cascade through term J_{drag} is negligible compared to those by terms (I) and (IV). We note that both Figures 4.4 and 4.5 indicate that the contribution to the energy cascade of the high-density flow in the near-wall region is insignificant.

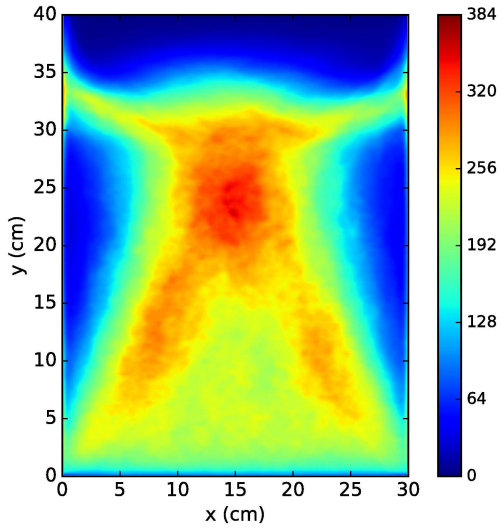

Figure 4.5: The time-averaged contour plots of the energy exchange rate between two phases through J_{drag}. The color-bar values are in $\frac{\mathrm{g}}{\mathrm{cms}^3} = 10^{-1}\frac{\mathrm{J}}{\mathrm{m}^3\mathrm{s}}$.

Figures 4.6a and 4.6b show the time-averaged contours of energy, per unit time, extracted from the mean

kinetic energy of the particles and converted into the particle internal energy through frictional shear stress and pressure, respectively. As shown, the main contribution of the frictional stress to the energy cascade is via the shear stress; the effect on the energy cascade of frictional pressure is negligible. Although the frictional stress plays a significant role in the momentum transport in the highly dense near-wall region, Figure 4.6a indicates that its contribution to the energy cascade is negligible due to a minimal velocity gradient in this region. It appears that the dominant region of mean kinetic energy dissipation by the frictional stress is located at the center of the bed, possibly due to the collision of two principal upward particle streams, as mentioned.

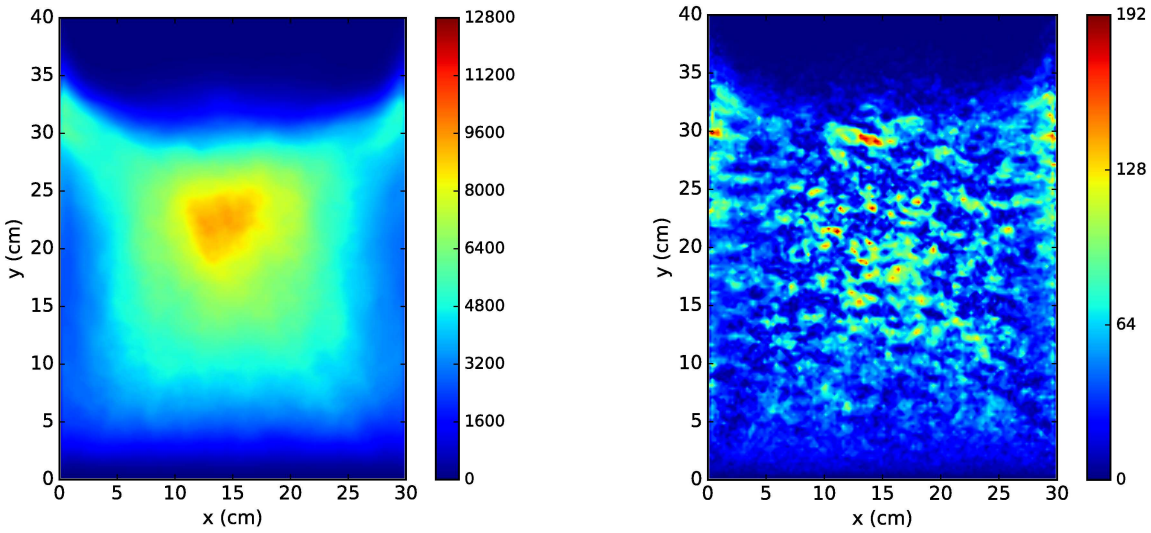

(a) Term (III,iii) **(b)** Term (II,iii)

Figure 4.6: The time-averaged contour plots of energy, per unit time, dissipated as heat by (a) term (III,iii), i.e., frictional shear stress and (b) term (II,iii), i.e., frictional pressure. The color-bar values are in $\frac{\mathrm{g}}{\mathrm{cms}^3} = 10^{-1}\frac{\mathrm{J}}{\mathrm{m}^3\mathrm{s}}$.

Recalling Figure 4.2, the particle mean kinetic energy dissipates into particle fluctuating energy via terms (II,ii), (III,ii), and Γ_{slip}. Figure 4.7 represents the time-averaged spatial distribution of the granular energy production, per unit time, through these terms. A comparison of Figures 4.7a and 4.7b indicates that the granular energy produced by the kinetic-collisional pressure is comparable to that produced by the kinetic-collisional shear stress. Therefore, the kinetic-collisional part of the particle pressure contributes substantially to the production of fluctuating energy via extracting energy from the mean particle-flow. This observation is unlike that observed in single-phase incompressible turbulent flows, where the contribution of fluid pressure to the production of turbulence kinetic energy is negligible compared to that of the mean shear stress. Figure 4.7c shows that the production of granular energy due to the slip velocity between the two phases, i.e., Γ_{slip}, is negligible in dense gas-particle flows. This term might play a more significant role in the energy cascade of dilute to moderately dense gas-particle flows where the gas turbulence is not negligible. A comparison of Figures 4.7a and 4.6a, indicates that, although the frictional stress is taken into account for only a narrow window of particle volume fraction, i.e., $0.6 \leq \varepsilon_p \leq 0.64$, the contribution of the frictional

stress in the cascade of energy is comparable to that of the kinetic-collisional stress, whereas in the dilute or moderately dense flows, frictional stress is typically not important.

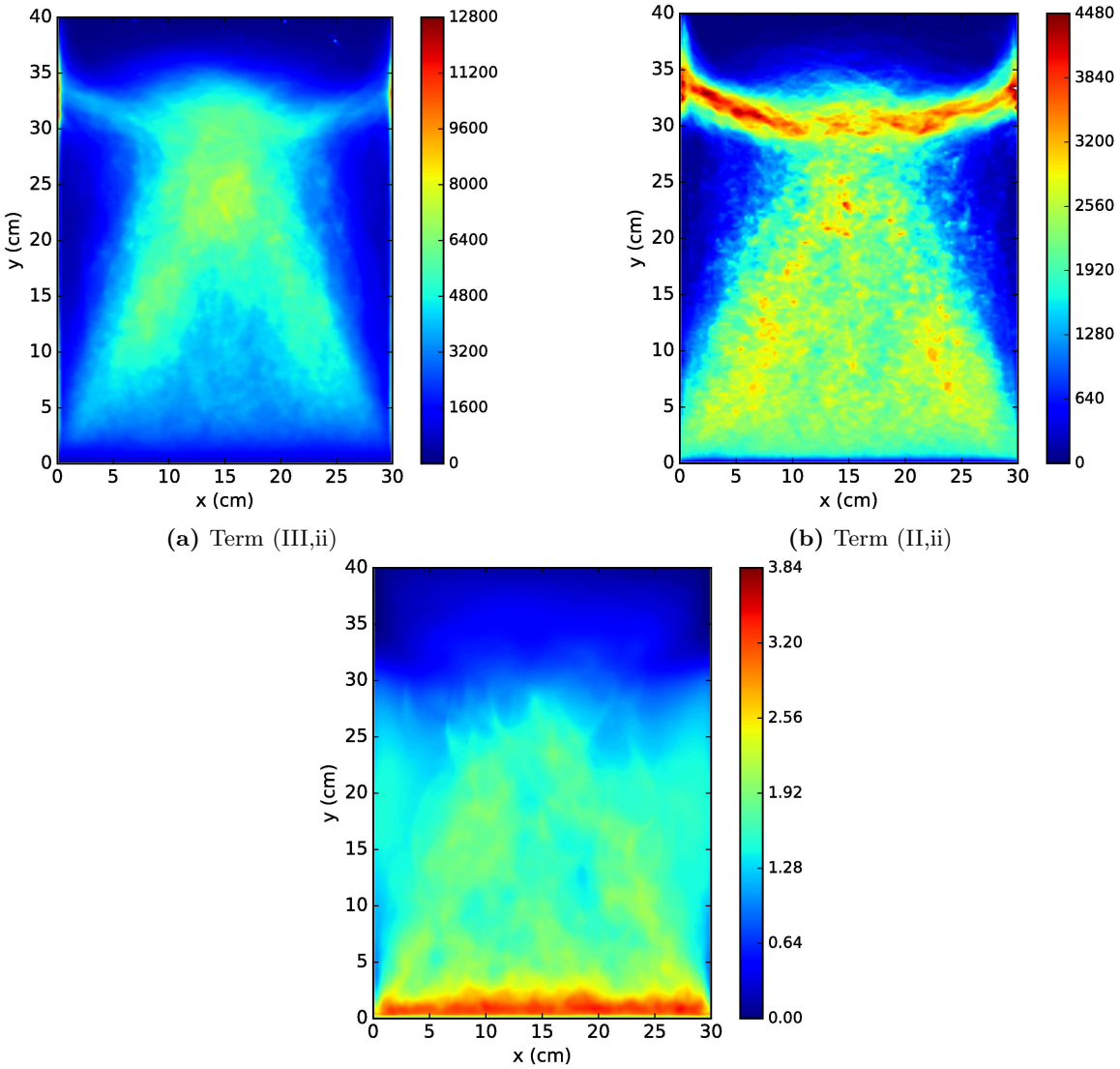

(a) Term (III,ii)

(b) Term (II,ii)

(c) Term Γ_{slip}

Figure 4.7: The time-averaged contour plots of granular energy production, per unit time, by (a) term (III,ii), i.e., kinetic-collisional shear stress, (b) term (II,ii), i.e., kinetic-collisional pressure, and (c) term Γ_{slip}. The color-bar values are in $\frac{\text{g}}{\text{cms}^3} = 10^{-1}\frac{\text{J}}{\text{m}^3\text{s}}$.

As shown in Figure 4.2, the produced granular energy dissipates into particle internal energy through inelastic particle collisions, i.e., J_{coll}. Figure 4.8a represents the time-averaged contour plots of the rate of fluctuating energy dissipation through J_{coll}. This figure indicates that the central region where two principal upward particle streams interact with each other, i.e., 10 cm $< x <$ 20 cm and 18 cm $< y <$ 28 cm, corresponds to the dominant region of granular energy dissipation. Figure 4.8b shows the time-averaged spatial distribution of the granular energy production, per unit time, via both kinetic-collisional pressure and shear stress. Figures 4.8a and 4.8b are almost identical, indicating that overall, the rate of granular energy

supply is equal to the rate of dissipation. Therefore, the well-known algebraic approximation of the transport equation for the granular energy can be used to produce an accurate distribution of granular temperature.

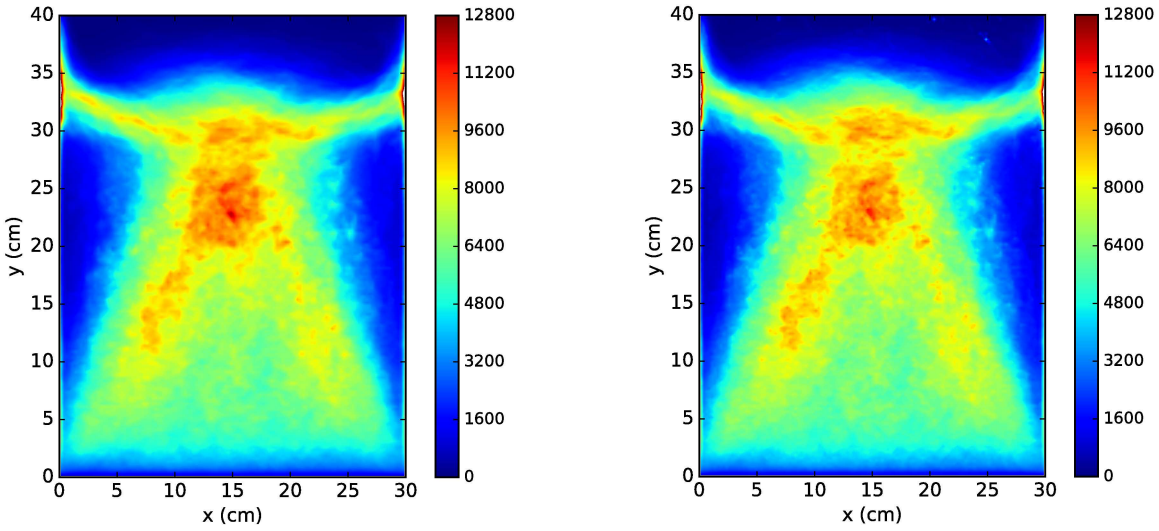

(a) Term J_{coll} **(b)** Terms (II,ii)+(III,ii)

Figure 4.8: The time-averaged contour plots of (a) dissipation of granular energy, per unit time, into heat through particle inelastic collisions and (b) net production of granular energy by both kinetic-collisional shear stress and pressure. The color-bar values are in $\frac{\text{g}}{\text{cms}^3} = 10^{-1}\frac{\text{J}}{\text{m}^3\text{s}}$.

Figure 4.9 represents the time-averaged contours of the rate of mean kinetic energy converted to potential energy. This figure indicates that the principal role of the highly dense flow in the near-wall region is limited to the conversion of particle mean kinetic energy to potential energy. As shown in previous figures, this region does not play a significant role in the energy cascade. Overall, most of the energy cascade occurs in the central region of the bed surrounded by the high-concentration near-wall flows. This is due to the migration of bubbles, initially formed as small structures near the bottom and wall regions, that coalesce as they rise towards the central region.

Although the near-wall region in the bubbling bed does not significantly participate in the energy cascade, the effect of the particle-wall boundary condition itself might be significant in the prediction of the flow. As mentioned above, the dynamics of bubbling beds are dominantly influenced by the motion of bubbles. Because the bubble formation is highly dependent on the particle energy level, the particle-wall boundary condition may affect the bubble behavior through the dissipation of the particle mean kinetic energy. Therefore, it is important to evaluate the contribution of the wall to the overall energy cascade that occurs in the bed. Figure 4.10 represents the time-averaged contribution of different terms involved in the particle-wall BC to the energy cascade, as described at the end of Section 4.2. This figure shows the corresponding time-averaged contour plots on the front wall located at $z = 0$ cm. Figures 4.10a and 4.10b show the contour plots of the production of granular energy, per unit time, supplied by the particle mean kinetic energy, and the rate of dissipation of granular energy into heat by inelastic particle-wall collisions at the wall, respectively. The rate of production of granular energy by the work performed by the wall collisional stress is approximately equal

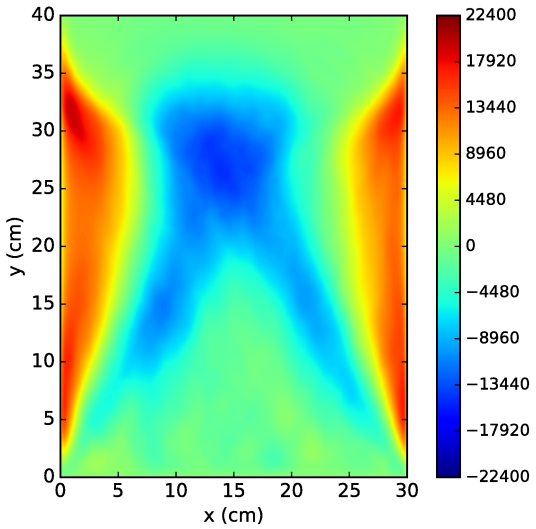

Figure 4.9: The time-averaged contour plots of potential energy, per unit time. The color-bar values are in $\frac{\mathrm{g}}{\mathrm{cms}^3} = 10^{-1}\frac{\mathrm{J}}{\mathrm{m}^3\mathrm{s}}$.

to its rate of dissipation into heat. Comparing these figures and Figure 4.8 shows that the rate of production of granular energy by the wall collisional stress is less than, but comparable to, that of the kinetic-collisional stress in the interior plane. Figure 4.10c also shows the rate of dissipation of the mean kinetic energy by the wall frictional stress. Figures 4.10c indicates that the regions on the wall corresponding to the maximum values of dissipation of the mean kinetic energy by the particle-wall friction are located away from the center and near the side-walls, whereas Figure 4.6a shows that the region where the maximum values of dissipation of the mean kinetic energy by the particle-particle friction occur is located in the central region. We note that the work performed by the wall frictional stress is related to the particle slip velocity on the wall (see Eq. 4.5), whereas the work performed by the particle-particle frictional stress is related to the particle velocity gradient; see term (III,iii) in Section 4.2. Figure 4.10 shows qualitatively that the overall contribution of the collisional stress on the wall to the energy cascade is larger than that of the frictional stress.

An energy budget analysis was performed to quantify the energy cascade in the bubbling bed. Table 4.3 summarizes the contribution of the previously discussed terms to the energy cascade, for different wall BCs, over the last 10 seconds of the simulation.

Table 4.3: Results of energy budget analysis ($t = 90$ s $- 100$ s); units are kJ.

	Inside the bed							At the wall		
BC type	(I)	(IV)	(II,ii)+(III,ii)	(II,iii)+(III,iii)	Γ_{slip}	J_{drag}	J_{coll}	$\mathcal{D}_w^f$	$\mathcal{P}_w^c$	$\mathcal{D}_w^c$
Johnson–Jackson [25]	13.4	12.4	8.5	5.9	0.0024	0.31	9.4	3.4	5.0	2.2
Jenkins–Louge [72]	14.1	12.9	11.8	5.9	0.0025	0.36	11.5	0.59	0.99	1.0
Schneiderbauer et al. [73]	14.1	12.9	12.0	6.0	0.0026	0.36	11.5	0.62	0.94	1.0

This table indicates that, inside the bed, the effect on the energy cascade of the gas pressure gradient, i.e.,

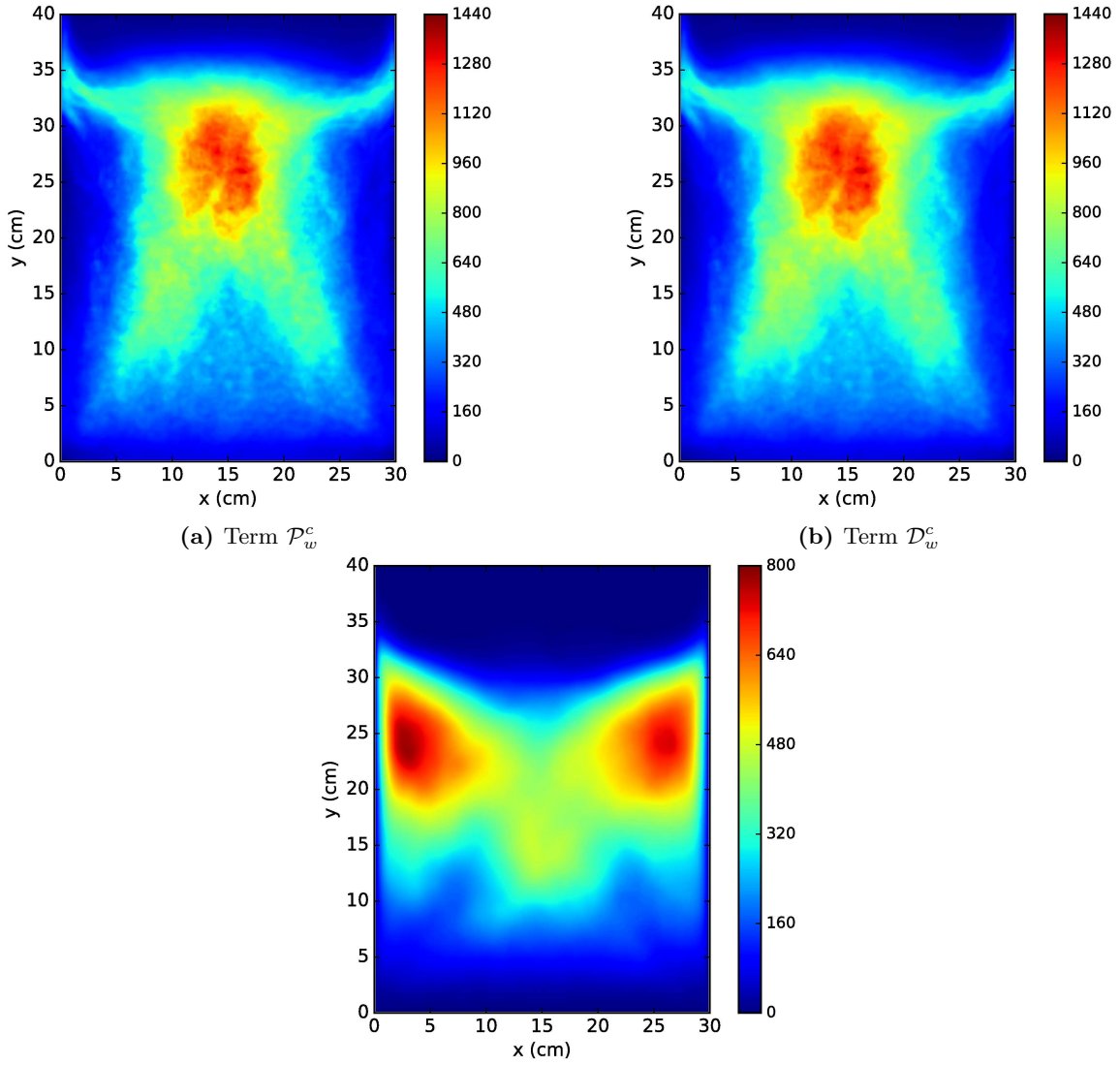

(a) Term $\mathcal{P}_w^c$

(b) Term $\mathcal{D}_w^c$

(c) Term $\mathcal{D}_w^f$

Figure 4.10: The time-averaged contour plots of (a) rate of production of granular energy at the wall, i.e., $\mathcal{P}_w^c$, (b) rate of dissipation of granular energy to heat via inelastic particle-wall collisions, i.e., $\mathcal{D}_w^c$, and (c) rate of dissipation of mean kinetic energy by frictional stress at he wall, i.e., $\mathcal{D}_w^f$. The unit of color-bar values is $\frac{\mathrm{g}}{\mathrm{s}^3} = 10^{-3}\frac{\mathrm{J}}{\mathrm{m}^2\mathrm{s}}$.

term (I), is slightly larger than that of the drag, i.e., term (IV). Also, it appears that the dissipation of the particle mean kinetic energy through both kinetic-collisional and frictional stresses are comparable, with the former giving a relatively larger contribution to the energy cascade. We note that the contribution of Γ_{slip} to the energy cascade is minimal among all the terms involved. The overall net granular energy, i.e., production minus dissipation produced inside the bed corresponding to the BCs of Johnson–Jackson, Jenkins–Louge, and, Schneiderbauer et al. are -1.21 kJ, -0.06 kJ, and -0.14 kJ, respectively. This indicates that on average the flow inside the bed as predicted by the Jenkins–Louge BC tends toward local equilibrium, i.e., the production of granular energy is approximately equal to its dissipation, compared to the flow predicted by the other two BCs. Consistent with the result of [2], this indicates that the Jenkins–Louge BC predicts the bed dynamics somewhat better than the more widely used boundary condition of Johnson–Jackson. From Table 4.3, it can be seen that 36.8%, 8.2%, and 8.0% of the total dissipation of the particle mean kinetic energy occurs at the bed walls as predicted by the BCs of Johnson and Jackson, Jenkins and Louge, and Schneiderbauer et al., respectively. Also, the wall contribution to the total production of granular energy is 37.1%, 7.7%, and 7.3%, corresponding to the BCs of Johnson and Jackson, Jenkins and Louge, and Schneiderbauer et al., respectively. These results indicate that the energy budget predicted by the Johnson–Jackson BC substantially differs from those predicted by the other two BCs at the wall. Table 4.3 shows no significant difference between the predictions of the BCs of Jenkins and Louge and Schneiderbauer et al. In the Johnson–Jackson BC, the contributions of both wall collisional and frictional stresses to the dissipation of the mean kinetic energy, i.e., $\mathcal{P}_w^c$ and $\mathcal{D}_w^f$, are highly overestimated. Consequently, much more particle mean kinetic energy is dissipated at the wall as predicted by the Johnson–Jackson BC, leading to the formation of more vigorous bubbles. More vigorous bubbles tend to bring particles closer to each other, leading to a decrease in the level of the particle fluctuating energy, which in turn results in a less expanded bed. We note that the Johnson–Jackson BC was developed heuristically such that the effect of momentum and energy transfer of the colliding particles is characterized by the specularity coefficient, whereas in the more sophisticated BCs of Jenkins and Louge and Schneiderbauer et al., the particle-wall collisions are more accurately accounted for, and the sticking and sliding collisions are distinguished.

4.5 Conclusions

An in-depth systematic study that used a particle energy budget analysis was performed to investigate the dynamics of a 3D bubbling bed. An equation for the kinetic energy of the mean particle flow was rigorously derived in the context of TFM approach, and the physical implications of the terms involved were discussed. The time-averaged spatial distribution of different terms appearing in the energy equation was visualized. The budget analysis not only quantifies the relative importance of various terms contributing to the energy cascade, but it also identifies the regions in the bed where most of the energy cascade takes place.

The results of the energy analysis indicate that the mean particle-flow gains its kinetic energy from the

mean kinetic energy of the gas phase through large-scale gas pressure gradient and drag terms. It was found that the role of each term was equally significant in the exchange of mean kinetic energy between the two phases and happens in the central region of the bed. The conversion of particle fluctuating energy into internal energy of the gas phase was estimated to be negligible. The contributions to the energy cascade of both kinetic-collisional and frictional stresses were found to be comparable. The kinetic-collisional stress extracts mean kinetic energy to produce granular energy, whereas the frictional stress dissipates it into heat. It was also observed that the kinetic-collisional part of the particle pressure contributes substantially to the production of fluctuating energy by extracting energy from the mean particle-flow. It was determined that, among the terms involved in the energy cascade process, the minimum contribution corresponds to the production of granular energy due to slip velocity between the two phases. It was observed that highly dense flow in the near-wall region did not contribute much to the energy cascade, and its role was limited to the conversion of particle mean kinetic energy to potential energy.

In addition to the energy cascade that happens through particle-particle and particle-gas interactions, the energy cascade that occurs at the physical walls due to the wall-particle interaction was investigated. In this regard, three different wall boundary conditions for the particulate phase that account for the particle slip-velocity and the granular energy flux at the wall were assessed, and the wall contribution to the dissipation of mean particle kinetic energy and random particle fluctuating energy predicted by each BC was determined. The wall BCs considered in this study included those of Johnson and Jackson [25], Jenkins and Louge [72], and Schneiderbauer et al. [73].

The energy budget predicted by the Johnson–Jackson BC substantially diverges from those predicted by the other two wall BCs. For example, the wall contribution to the total dissipation of particle mean kinetic energy was found to be 36.8%, 8.2%, and 8.0% as predicted by the BCs of Johnson and Jackson, Jenkins and Louge, and Schneiderbauer et al., respectively. For the Johnson–Jackson BC, the contributions of both wall collisional and frictional stresses to the dissipation of the mean kinetic energy were highly overestimated. It was also found that the source terms, i.e., dissipation and production contributions, in the granular energy equation played a more significant role in the energy cascade compared to the convective and diffusive terms. The overall net granular energy produced inside the bed corresponding to the BCs of Johnson–Jackson, Jenkins–Louge, and Schneiderbauer et al. were -1.21 kJ, -0.06 kJ, and -0.14 kJ, respectively. This indicates that on average the flow inside the bed as predicted by the Jenkins–Louge BC tends more toward local equilibrium than the flows predicted by the other two BCs.

Acknowledgement

The authors are grateful to the Natural Sciences and Engineering Research Council of Canada (NSERC) for providing financial assistance for this research project.

Chapter 5

Identifying particle flow structures in a dense gas-particle fluidized bed using proper orthogonal decomposition

A similar version of this chapter is submitted as:

- M. R. Haghgoo, D. J. Bergstrom, and R. J. Spiteri. Identifying particle flow structures in a dense gas-particle fluidized bed using proper orthogonal decomposition. *J. Fluid Mech.* Submitted, 2018.

The first author conducted the simulations, post-processed and analyzed the results, and prepared the first draft of the manuscript. He then worked with the co-authors to discuss the results and finalize the content and form of the manuscript.

Preamble

The motion of bubbles through the bed induces strong unsteady flow patterns and creates intense fluctuations in the particle velocity and volume fraction fields. The complex fluctuating components of the particle flow fields, giving rise to an enhanced particle mixing, are not reflected in the time-averaged flow features. Therefore, it is significant to quantitatively assess the particle-flow fluctuating fields. To this end, state-of-the-art post-processing methodologies namely, the Proper Orthogonal Decomposition (POD) and the swirling strength criterion, are applied to the fluctuating particle flow fields predicted by the two-fluid model of the bubbling bed discussed in the previous two chapters to identify and analyze the dominant spatio-temporal patterns of the particulate phase.

The instantaneous particle flow is determined to be characterized by the formation of high-vorticity regions in the vicinity of the bubble boundaries with a relatively higher vorticity magnitude in the wake region of bubbles. The dominant particle meso-scale fluctuating velocity patterns (the first two most energetic POD modes) are principally aligned in the axial direction, corresponding to the particle mixing by the bubble wakes, with laterally directed fluctuating velocity vectors at the bed surface, corresponding to the mixing caused by the bubbles bursting. Applying the swirling strength criterion reveals the existence of smaller ring-like vortex sheets in the lower part of the bed, larger ribbon-like structures in the middle of the bed, and a laterally oriented vortex sheet at the bed surface. It is observed that the main characteristic feature of the particle vortical motions is their flat structure. The flat vortex sheets appear to be stable structures in bubbling beds, unlike the case of single-phase turbulent flows, that emerge due to the collective effect of instabilities occurring in the particulate phase.

Abstract

The particle flow fields, i.e., particle volume fraction and velocity fields, inside bubbling beds exhibit strong unsteady flow patterns accompanied by intense meso-scale fluctuations induced by the motion of bubbles. State-of-the-art post-processing methodologies, the Proper Orthogonal Decomposition (POD) and the swirling strength criterion, are applied to the fluctuating particle flow fields predicted by the two-fluid model of a bubbling bed to identify and analyze the dominant spatio-temporal patterns of the particulate phase. The variation of the POD temporal coefficients associated with the particle volume fraction fluctuation field indicates the existence of a low-dimensional attractor and irregular periodicity in the flow. Three-dimensional POD results indicate that the dominant particle meso-scale fluctuating velocity patterns (first two energetic POD modes) are principally aligned in the axial direction, corresponding to the particle mixing by the bubble wakes, with laterally directed fluctuating velocity vectors at the bed surface, corresponding to the mixing caused by the bubbles bursting. The identified particle vortical motions are characterized by their flat structure. These flat vortex sheets appear to be stable structures in bubbling beds that emerge due to the collective effect of instabilities occurring in the particulate phase. POD is used to obtain a reduced-order reconstruction of the particle velocity and volume fraction fields using a subset of the high-energy containing modes. The ability of the POD eigenmodes to reproduce the instantaneous fields is systematically assessed.

5.1 Introduction

Fluidization refers to a process where solid particles are transformed into a fluid-like state through suspension in a gas (or liquid). Gas-particle fluidized beds have widespread application in industry due to their increased rate of heat, mass, and momentum transfer, and particle mixing. Using a non-linear stability analysis, Anderson et al. [89] demonstrated that in bubbling fluidized beds the meso-scale structures, i.e., bubbles, form due to a loss of stability of upward traveling waves subject to horizontal perturbations. Here, a bubble is understood to be a localized region of gas, typically moving as an entity through the particulate phase. As indicated in our previous study [20], the formation of large bubble structures in bubbling fluidized beds occurs due to the coalescence of small bubbles that originate in the bottom and near-wall regions of the bed. As the bubbles rise, they tend to migrate towards the central region due to its lower resistance. Eventually, the bubbles burst at the surface of the bed, and the particles, being carried by the bubbles, are dispersed transversely from a vertically oriented motion toward the walls, leading to fluctuations in the bed surface.

The motion of bubbles through the bed induces strong unsteady flow patterns and creates intense fluctuations in the particle velocity and volume fraction fields. The mean transport of particle fluctuating momentum by meso-scale particle velocity fluctuations, i.e., resolved-scale particle Reynolds stress, gives rise to a significant increase in the particle mixing. In this regard, it is shown in our recent study [2] that the mixing caused by the resolved-scale particle Reynolds normal stress is much stronger than the mixing

caused by the particle Reynolds shear stress. This indicates that, in addition to the mean flow field, it is significant to quantitatively explore the fluctuating particle flow field. However, most of the studies available in the literature have focused on the time-averaged features of bubbling beds: only a few studies investigate the fluctuating topologies of the particle flow fields. The complex fluctuating components of the particle flow fields that give rise to enhanced particle mixing are not reflected in the time-averaged flow features. Therefore, it is significant to assess the particle-flow fluctuating fields in a quantitative manner. Indeed, a strong motivation for undertaking the present study was to utilize state-of-the-art post-processing tools to identify particle vortical structures and quantitatively analyze dominant spatio-temporal patterns associated with the particle fluctuating fields.

The introduction of proper orthogonal decomposition (POD) as a powerful tool for the analysis and synthesis of numerical and experimental solutions has improved our understanding of the flow behavior in complex systems. The POD performs a modal decomposition of an ensemble of functions, such as data obtained from numerical or experimental studies, to extract the most dominant features of the process. In the context of fluid flow these dominant features are typically the spatio-temporal patterns, e.g., coherent structures in turbulent flows. Lumley [93] was the first to introduce the POD in the context of turbulence. Cizmas et al. [94] applied a two-dimensional (2D) POD on the flow field predicted by a "two-fluid model" (TFM) of a spouting bed to explore the utility of a reduced-order model (ROM). Palacios et al. [95] also applied 2D POD on a set of experimental data of a spouting bed and showed that the overall dynamics of the bed can be captured by only a few POD eigenfunctions. Cizmas et al. [96] applied several acceleration techniques to a POD-based ROM of a 2D gas-particle fluidized bed. Overall, these three seminal studies utilized 2D POD for the purpose of developing a ROM of fluidized beds and hence are less focused on the investigation of the particle flow structures as a tool to analyze the particle flow fields. Although POD is frequently used to examine single-phase turbulent flows, the use of three-dimensional (3D) POD is still relatively rare even in such applications [97]. To the best of the authors' knowledge, the use of 2D POD in dense gas-particle flows is limited to the three studies mentioned above, mainly focused on developing a ROM. In the current study, a 3D POD technique is used to quantitatively assess the dominant spatio-temporal patterns of the fluctuating particle velocity and volume fraction fields in a bubbling fluidized bed.

The motion of bubbles through a bed induces particle vortical structures in the particulate phase. The instantaneous particle flow consists of a complex mixture of these structures that play a dynamically significant role in the particle kinetic energy and its dissipation, particle mixing, and transport of mass, momentum, and heat through the bed reactor. Therefore, it is significant to identify these vortical structures that mainly originate due to the interaction of bubbles with the particulate phase and give rise to the particle mixing in bubbling beds. Identification of these structures not only helps to gain a deeper insight into the complex flow phenomena in fluidized beds, but also is a prerequisite for flow prediction and control. It is well-established that the vortical structures play a significant role in the dynamics of single-phase turbulent flows. Based on this knowledge, it is logical to explore the role of vortical motions in the particle phase inside a bubbling

bed. To identify and visualize the local vortex structures, several vortex identification methods have been developed, mostly based on the velocity gradient tensor. The most widely used vortex identification techniques are associated with determining the following parameters: the second invariant (Q) [98], Δ [99], λ_2 [100], and swirling strength (λ_{ci}) [101]. In this study, the Q, Δ, and λ_{ci} criteria were initially implemented to identify particle vortical structures. However, no significant difference was observed in the vortical structures captured by each criterion. Therefore, following Hossain et al. [97], who conducted a comparative study among these different criteria and showed that the swirling strength criterion resulted in the cleanest visualization, only the results using the λ_{ci} criterion are discussed in this study. The swirling strength technique uses the imaginary part of the complex eigenvalue of the velocity gradient tensor to visualize vortices [102]. The swirling strength, determined by λ_{ci}, is a measure of the local swirling rate inside the vortex. One distinctive feature of the swirling strength criterion is that it identifies not only the vortex core region but also the strength and the local plane of swirling [103].

It is significant to quantitatively explore the meso-scale fluctuating particle flow fields induced by the motion of bubbles through a fluidized bed. To this end, for the first time, a 3D POD technique is applied to the particle flow fields predicted by a TFM of a bubbling bed to identify and analyze the dominant spatio-temporal patterns. The instantaneous particle velocity fields inside the bed are used to investigate the particle-flow structures, including the vortical ones, that characterize the flow. Based on the analogy with the single-phase turbulent flow, for the first time, the particle vortical structures in a bubbling bed are identified using a swirling strength criterion to assess their role in the dynamics of the bed. 3D POD is used to extract the dominant vortical motions and obtain a reduced-order reconstruction of the particle velocity and volume fraction fields using a subset of the high-energy containing modes. The ability of the eigen-modes to reproduce the instantaneous particle velocity and volume fraction fields is systematically assessed.

5.2 Mathematical modeling

The Eulerian–Eulerian TFM, based on the locally averaged equations derived by Anderson and Jackson [7], is used to simulate a dense gas-particle flow inside a 3D thin fluidized bed. The governing and constitutive equations describing the dynamics of such a system can be found in our previous study [2] and accordingly are not repeated here. Haghgoo et al. [2, 21] showed that the Jenkins–Louge particle-wall boundary condition [72] predicts the bed dynamics somewhat better than the more widely-used boundary condition of Johnson–Jackson [25]. Therefore, in this study the former particle-wall boundary condition was used to account for the particle momentum and granular energy fluxes at the walls.

5.2.1 Proper orthogonal decomposition

We consider an ensemble of numerical or experimental observations of a scalar variable $u(x,t)$. It is significant to know which single function is "most similar" to the observations of $u(x,t)$, on average. The mathematical

statement of the notion "most similar" corresponds to choosing a function φ to maximize the normalized average projection of u onto φ [104]:

$$\max_{\varphi \in L^2(D)} \frac{\left\langle |\,(u,\varphi)\,|^2 \right\rangle}{\|\varphi\|^2}, \tag{5.1}$$

where $\langle . \rangle$, $|.|$, $(.,.)$, and $\|.\|$ denote the averaging operation, absolute value, inner product, and L^2-norm, respectively. Here, L^2 is a Hilbert space and D is a bounded subset of real Euclidean space. Finding a function φ such that its normalized inner product with the field u is maximized is a classical problem in the calculus of variations [104]. Holmes et al. [105] showed that the condition in Eq. 5.1 reduces to an eigenvalue problem:

$$\int_D \underbrace{\langle u(x,t)u^*(x',t)\rangle}_{R(x,x')} \varphi_(x')dx' = \lambda\varphi(x). \tag{5.2}$$

Here, * denotes the complex conjugate and R is defined to be the averaged autocorrelation tensor. Eq. 5.2 can be rewritten as an operator equation: $\mathbf{R}\varphi = \lambda\varphi$. Therefore, the extremal basis is the eigenfunction corresponding to the largest eigenvalue of the autocorrelation tensor. It is also known that there are numerous solutions for the eigenvalues, λ_i, and eigenfunctions, φ_i, that satisfy Eq. 5.2. In POD analysis, It is common practice to sort the eigenvalues so that $\lambda_i \geq \lambda_{i+1}$, where $\lambda_i \geq 0$.

It is known that, see, e.g., Sirovich [106], almost every member of the ensemble can be reconstructed by a model decomposition based on a family of orthogonal basis functions $\Phi_i(x)$:

$$u(x,t) = \sum_{i=1}^{\infty} a_i(t)\Phi_i(x), \tag{5.3}$$

where the a_i are the temporal coefficients of the basis functions. We note that the $\Phi_i(x)$ in Eq. 5.3 can be any set of orthogonal basis functions, e.g., Fourier, Chebyshev, Legendre, and POD modes. However, what distinguishes the POD modes from other sets of orthonormal basis functions is the claim that the POD is in some sense optimal for reproducing the function $u(x,t)$. It implies that among all linear decompositions, the POD is the most efficient for reconstructing $u(x,t)$ in the sense that for a given number of basis functions it captures the most energy. Mathematically, for a given number of modes, say N, the reconstruction of the signal $u(x,t)$ by the POD modes converges in energy faster compared to the basis functions obtained by any other linear decomposition. This indicates that the average least-squares truncation error,

$$\varepsilon_N = \left\langle \|u(x,t) - \sum_{i=1}^{N} a_i(t)\Phi_i(x)\|^2 \right\rangle, \tag{5.4}$$

is minimal if the basis functions are the POD modes [94]. The optimality condition of Eq. 5.4 is equivalent to Eq. 5.1 [94]. Therefore, it implies that the POD basis functions must be the $\varphi_i(x)$. Stated differently, the truncation error in Eq. 5.4 is minimum if $\Phi_i(x) = \varphi_i(x)$. It is shown in [105] that the diagonal representation of the autocorrelation tensor results in,

$$\langle a_j(t)a_k^*(t)\rangle = \delta_{jk}\lambda_j, \tag{5.5}$$

implying that the modal coefficients of the POD modes are uncorrelated, on average. If $u(x,t)$ is a velocity, the average specific kinetic energy is:

$$\int_D \langle u(x,t)u^*(x,t)\rangle \, dx = \sum_i \langle a_i(t)a_i^*(t)\rangle \, . \tag{5.6}$$

Equations 5.5, and 5.6 imply that the eigenvalues λ_i represent the averaged specific kinetic energy of mode i, and $\sum_{i=1}^{N} \lambda_i$ is the energy contained in the first N modes.

The most widely used method to find the POD modes, i.e., Eq. 5.2, is the method of snapshots proposed by Sirovich [106]. The main simplifying assumption used in this technique to calculate the eigenfunctions is that the data vector u_i and the eigenvectors φ_i span the same linear space [105], implying that the eigenvectors can be written as a linear combination of the data vectors; i.e.,

$$\varphi_k = \sum_{i=1}^{M} v_i^k \mathbf{u}_i, \tag{5.7}$$

where M is the number of observations or snapshots. Sirovich [106] approximated the autocorrelation tensor as

$$R(x,x') = \frac{1}{M}\sum_{i=1}^{M} \mathbf{u}^i(x,t)\mathbf{u}^i(x',t). \tag{5.8}$$

The constants v_i^k are found by introducing Eqs. 5.7 and 5.8 in Eq. 5.2, which yields:

$$\mathbf{C}\mathbf{v} = \lambda \mathbf{v}, \tag{5.9}$$

where $\mathbf{v}^k = (v_1^k, ..., v_M^k)$ is eigenvector k of Eq. 5.9, and $\mathbf{C}$ is a symmetric $M \times M$ matrix defined by $[C_{ij}] = (1/M)(\mathbf{u}_i, \mathbf{u}_j)$. The instantaneous flow field can be reconstructed using a finite number (N) of POD modes,

$$u(x,t) = \overline{u}\,(x) + \sum_{k=1}^{N} a_k(t)\varphi_k(x), \tag{5.10}$$

where $\overline{u}\,(x)$ represents the time-average $u(x,t)$. The temporal coefficients a_k can be determined using the orthonormality property of the eigenfunctions:

$$a_k(t) = \int_D u'(x,t).\varphi_k(x)dx, \tag{5.11}$$

where $u'(x,t) = u(x,t) - \overline{u}\,(x)$.

5.2.2 Vortex identification methodology

To investigate the instantaneous vortex dynamics corresponding to the particle meso-scale fluctuating motions, a vortex identification method is required. As discussed previously, in this study the swirling strength [101] criterion is used to identify the particle vortical structures. The swirling strength technique uses the imaginary part of the complex eigenvalue of the velocity gradient tensor λ_{ci} to identify vortices [102]. The strength of the local swirling motion inside the vortex is characterized by λ_{ci}. We note that whenever the iso-surface of λ_{ci} is plotted to visualize the vortical structures, an arbitrary threshold value is selected to ensure clarity of the structures.

5.3 Numerical simulation

The computational domain was taken to be a 3D thin fluidized bed with dimensions of 70 cm × 30 cm × 1.5 cm in the axial, longitudinal, and lateral directions, respectively. Here, the axial, longitudinal, and lateral directions are aligned with the y, x, and z axes, respectively. 3D simulations of a bubbling fluidized bed were performed using the TFM approach of Anderson and Jackson [7]. The Multiphase Flow with Interphase eXchanges (MFIX) [11] software was used to perform the simulations. Additional Fortran subroutines were developed and integrated into the MFIX code to implement the Jenkins–Louge boundary condition [72]. All simulations were performed in parallel using 60 cores on an architecture consisting of dual Hex Core Intel Xeon X5650 2.66 GHz with 12 GB of RAM each and running Red Hat Enterprise Linux Server 5.7. The first 100 seconds of the fluidization process were simulated to achieve statistically steady-state solutions. Detailed information on the flow configuration, numerical methodology, grid study, and CPU-hours of computing to produce the results are provided in our recent work [2]. Extensive 3D simulations were performed to obtain the model parameter values that yielded the most comparable results with the experimental data. For detailed information, readers are referred to our previous study [2]. Special Python subroutines were developed to perform the POD analysis and identify the particle vortex motions using the swirling strength method.

5.4 Results and discussion

The validity of the numerical results predicted by the TFM was assessed in our previous study [2] by comparing them with the limited experimental measurements of Laverman et al. [83]. In this work, the first 100 seconds of the fluidization process were simulated, and 3D POD analysis was performed on the last 5001 snapshots at an interval of 0.01 s corresponding to the last 50 s of the simulation.

5.4.1 Time-averaged particle flow fields

Before studying the instantaneous flow characteristics of the bubbling bed, it is helpful to review the time-averaged particle flow structure. Figures 5.1a and 5.1b show contours of time-averaged particle volume fraction and particle vorticity fields based on 5001 snapshots, superposed over the particle-volume-fraction-weighted time-averaged (referred to as "time-averaged" for brevity) particle velocity vectors at a plane located at $z = 0.375$ cm. Figure 5.1a shows the formation of high-concentration regions near the wall that may be considered as a typical characteristic of bubbling fluidized beds. The velocity vectors plotted in Figure 5.1 indicate that, on average, the interaction of bubbles with the particles creates two elongated vortices of opposite sign contributing to the overall particle mixing in the bed. Figure 5.1b represents the vorticity field corresponding to these two vortices. This figure indicates that overall the near-wall region ($x < 4$ cm and $x > 26$ cm and 15 cm $< y <$ 30 cm) does not contain particle-flow motion corresponding to significant vorticity

strength and hence does not effectively contribute to the particle mixing inside the bed. This confirms the result of our last study [21], where it is shown that the near-wall region does not significantly contribute to the energy exchange, and this in turn results in the formation of a low-mixing region. This indicates that, unlike single-phase turbulent flows, the physical wall is not a significant source of local vorticity generation in bubbling beds. This is partly due the particle partial-slip velocity boundary condition at the wall, compared to the no-slip boundary condition in the case of single-phase turbulent flow. However, the main reason is due to the migration of bubbles as the major source of vorticity production towards the central region as they rise.

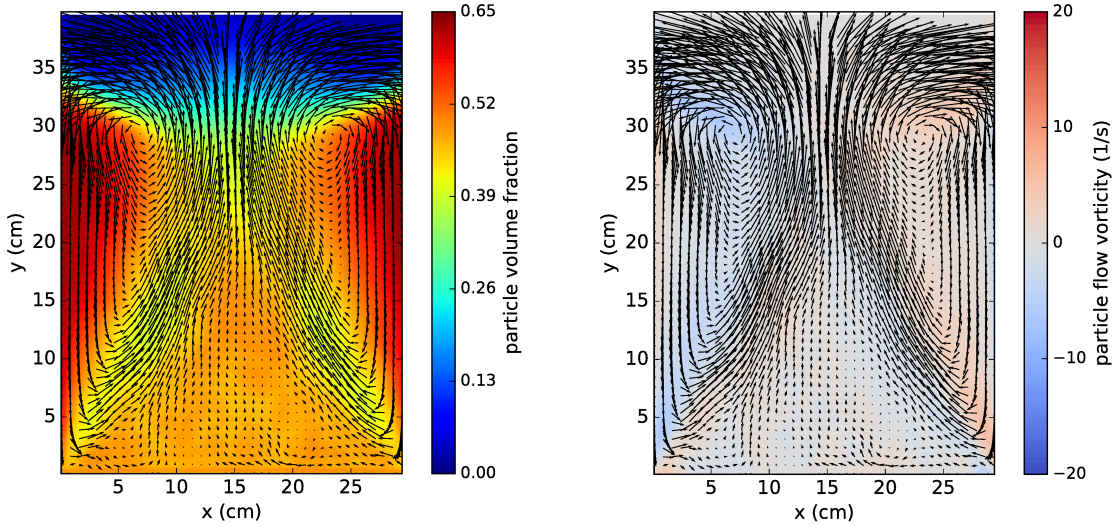

Figure 5.1: Contours of time-averaged (a) particle volume fraction, and (b) particle vorticity fields, superposed over the time-averaged particle velocity vectors at a plane located at $z = 0.375$ cm.

5.4.2 3D POD analysis of the particle volume fraction field

3D POD analysis is performed on the particle volume fraction fluctuation field to explore the main characteristic features of the dominant POD modes. Figure 5.2 shows the four dominant spatial modes of the particle volume fraction fluctuation. The time-averaged particle volume fraction field, which can be considered as the zeroth POD mode and was discussed in Figure 5.1a, is symmetric about the x-midplane. Figure 5.2a indicates that this reflective symmetry also appears in the first POD mode, even though none of the instantaneous snapshots are symmetric. This is in agreement with Dellnitz et al. [107], who observed that the symmetries of the attractors of partial differential equations in phase space manifest themselves as symmetry of the time-averaged solution. The second mode, i.e., Figure 5.2b shows an anti-symmetry of sorts, whereas the third and fourth modes show no symmetry. Overall, Figure 5.2 indicates that the dominant fluctuations in the particle volume fraction occur in the upper part of the bed (10 cm $< y <$ 30 cm), where the larger bubble structures form, due to coalescence of smaller bubble structures initially formed in the lower part of

the bed, and also at the bed surface (30 cm $< y <$ 35 cm), where the bubbles burst.

Figure 5.3 shows the instantaneous field and 3D POD reconstructions of the bubble structures represented by the iso-surface for a particle volume fraction of 0.2. Here, the first 50, 150, and 300 eigenmodes contain approximately 63%, 80%, and 88% of the total POD (energy), respectively. Figures 5.3b and 5.3c indicate that the reconstruction of the bubble structures based on the first 50 and 150 POD eigenmodes was successful in capturing the dominant features of the corresponding instantaneous field, i.e., larger structure bubbles. Increasing the number of POD modes to 300 resolves a number of smaller bubble structures near the distributor and hence results in a voidage field, as shown in Figure 5.3d, which is more similar to the original snapshot. Figure 5.3 illustrates the process of higher modes adding more detail. It appears that the structure and location of larger structure bubbles are captured by the first 50 modes and further addition of higher modes serves to refine the shape and size of the previously captured structures, in addition to detection of smaller structure bubbles.

Recall that the POD temporal coefficients, $a_k(t)$, modulate the contributions of the POD spatial modes in time to reproduce the actual flow field and represent the amplitude of the POD modes in the linear decomposition of the instantaneous fluctuation field. To gain deeper insight into the characteristics of and relations between POD modes, the temporal coefficients are investigated. Figure 5.4a shows the evolution of the first two eigenmodes associated with the particle volume fraction field in time, while Figures 5.4b and 5.4c present cross-plots of the same and a_1-a_3 temporal coefficients, respectively. If Figure 5.4a is considered as a dynamical system, its phase-space projection, i.e., Figure 5.4b, informs that the system evolves within a confined space, which might be indicative of an attractor. This is in agreement with Cizmas et al. [94], who suggested that the relatively closed nature of the resulting curves in a cross-plot of POD temporal coefficients indicates the existence of a low-dimensional attractor. We note that the cross correlation between a_1 and a_2, i.e., Figure 5.4b, has a distribution that is more concentrated in the first and fourth quarters of the state space, whereas Figure 5.4c shows a relatively more uniform distribution of a_1-a_3 in the state space. The variation of the POD temporal coefficients implies periodicity in the flow. However, the power spectral density of the POD temporal coefficients did not show a unique and well-defined dominant frequency but rather a plateau. This is in agreement with the results of our previous study [2], where the power spectral density of gas phase pressure fluctuations did not show a strong dominant frequency. These observations may suggest that the periodicity in the overall flow is irregular.

5.4.3 2D POD analysis of particle flow fields

To investigate the vortex generation by bubbles, the instantaneous particle velocity and volume fraction are considered as well as the vorticity field, i.e., the curl of velocity field. Figure 5.5a and 5.5b show the particle volume fraction and particle vorticity contours, respectively, superposed over the particle velocity vectors at the same plane as in Figure 5.1 at an arbitrary time of $t = 85$ s. Figure 5.5a qualitatively shows the presence of bubbles, i.e., regions of low particle volume fraction, inside the bed. Figure 5.5b indicates

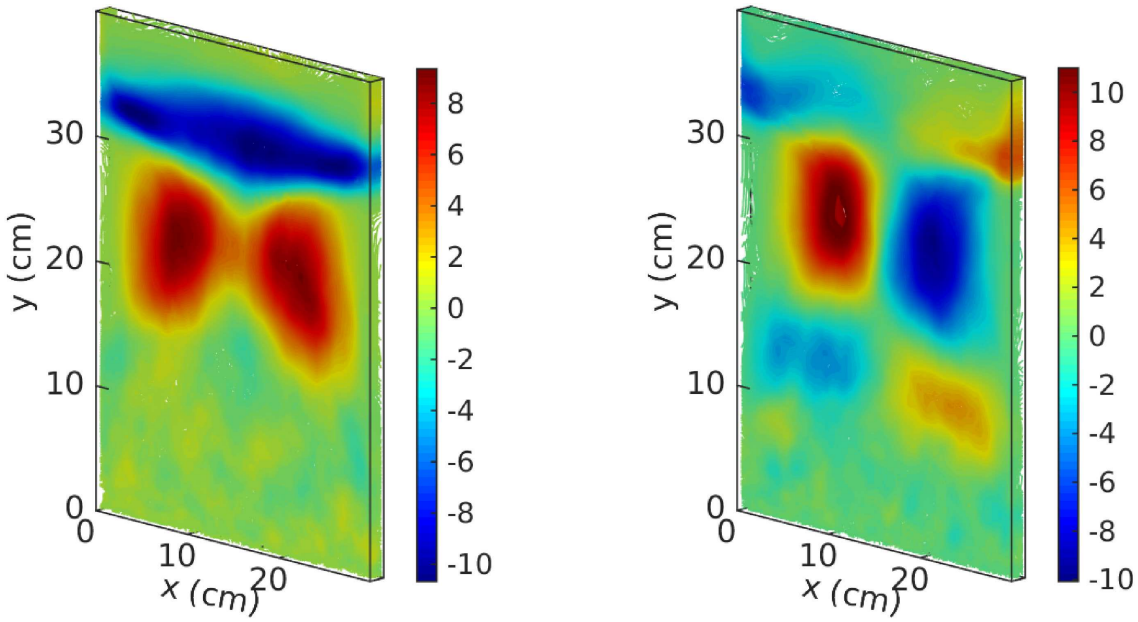

(a) First POD eigenmode

(b) Second POD eigenmode

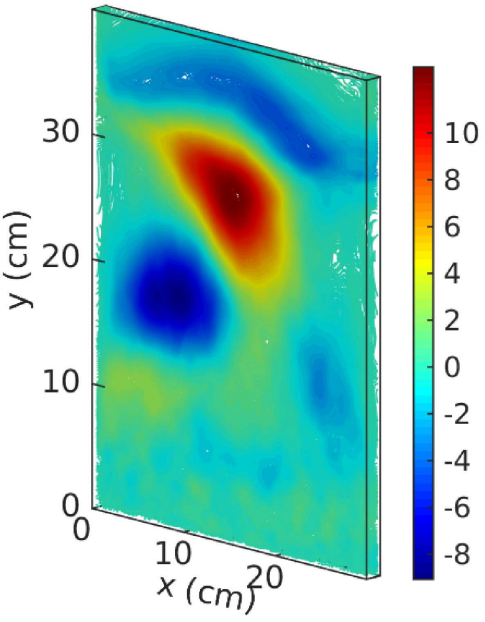

(c) Third POD eigenmode

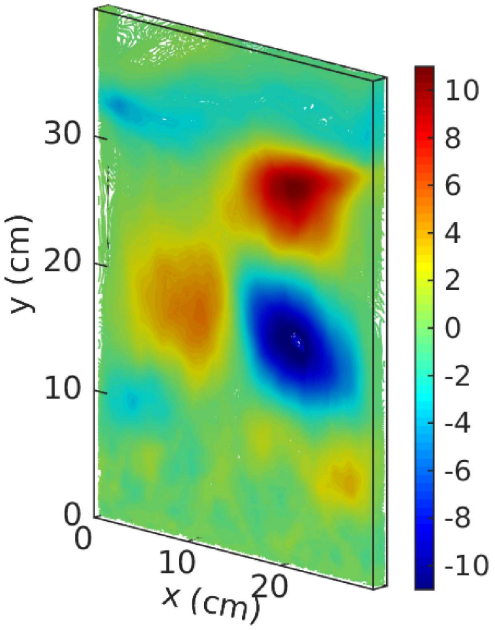

(d) Fourth POD eigenmode

Figure 5.2: First four dominant 3D POD modes of the particle volume fraction fluctuation field.

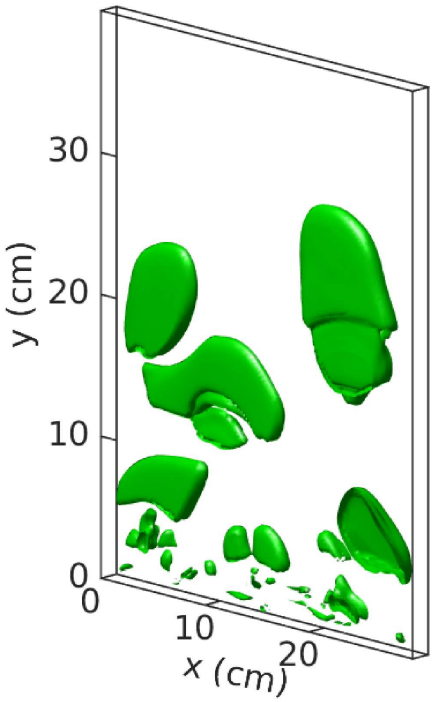

(a) Instantaneous bubble structure

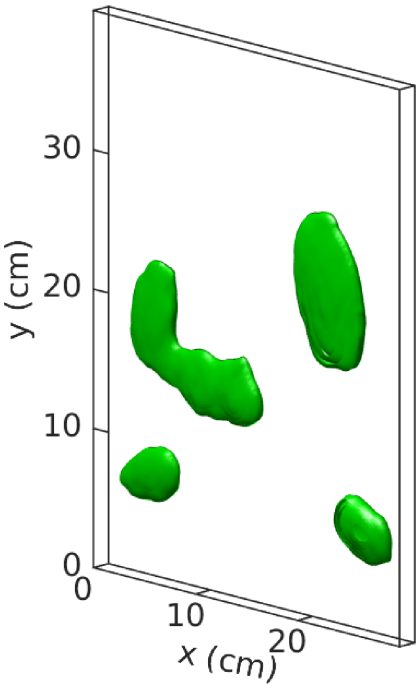

(b) POD reconstruction with 50 eigenmodes

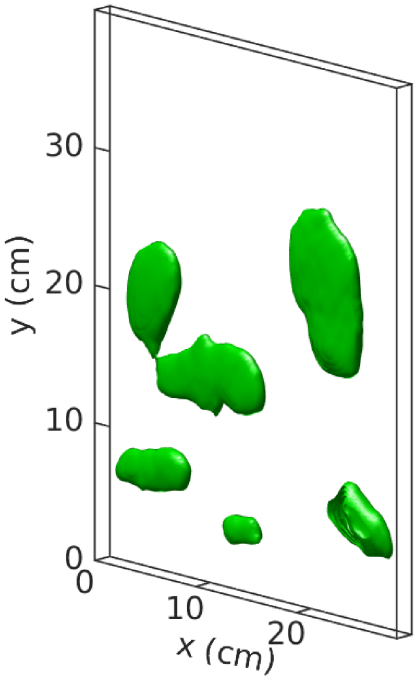

(c) POD reconstruction with 150 eigenmodes

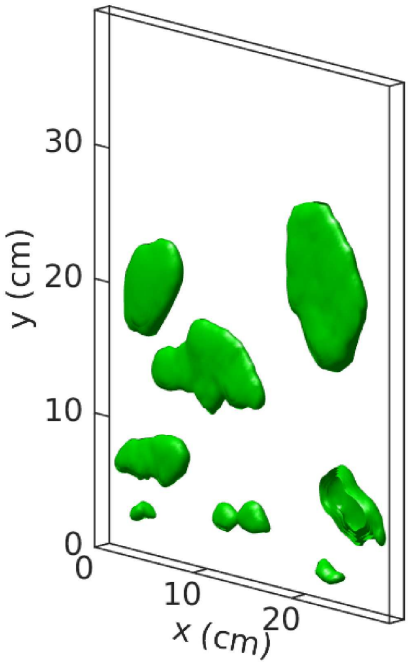

(d) POD reconstruction with 300 eigenmodes

Figure 5.3: (a) Instantaneous bubble structure at $t = 85$ s; 3D POD reconstruction of the instantaneous structures with (b) 50 eigenmodes (c), 150 eigenmodes, and (d) 300 eigenmodes, using iso-surfaces of particle volume fraction of 0.2.

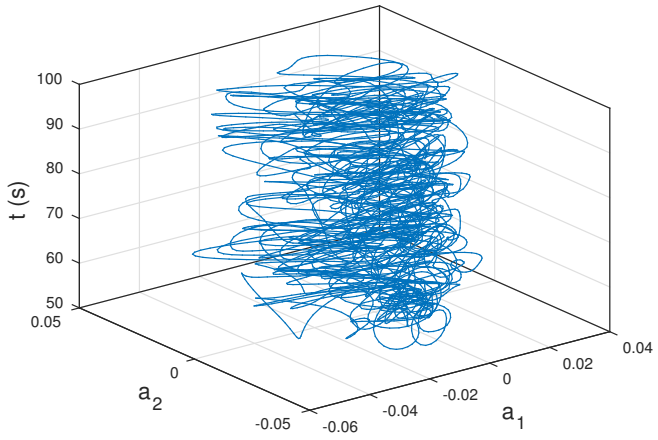

(a)

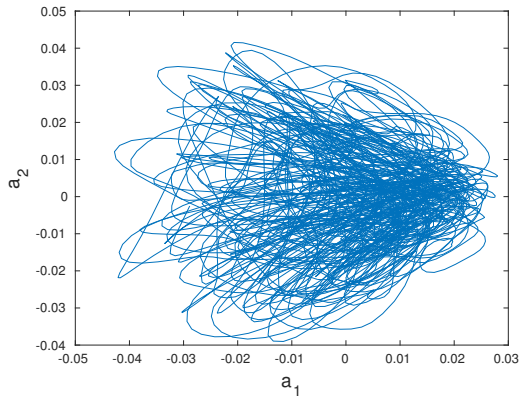

(b)

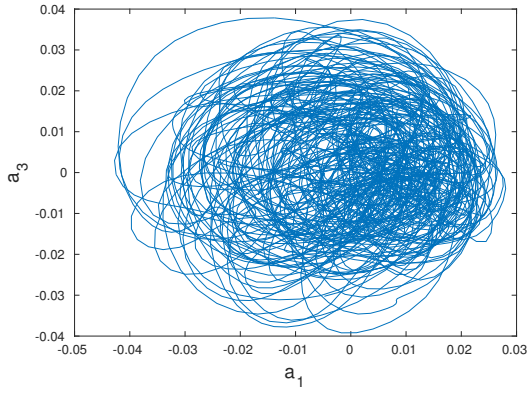

(c)

Figure 5.4: (a) time evolution of coefficients [a_1-a_2] (b) cross plot of coefficients [a_1-a_2] and (c) cross plot of coefficients [a_1-a_3].

that the instantaneous particle flow is characterized by the formation of high vorticity regions in the vicinity of the bubble boundaries with a relatively higher vorticity magnitude in the wake of the bubbles. This is in agreement with the well-established mechanism of particle mixing in bubbling beds. It is known that particles are entrained into the bubble wakes and carried upward [108]. To preserve continuity, particles rain down in the region surrounding the rising bubbles. Furthermore, particles are dispersed transversely from a vertically oriented motion by bubble burst at the bed surface. Finally, mixing is caused, to a lesser extent, by the lateral motion of bubbles due to interaction and coalescence of neighboring bubbles [109]. Each vorticity region detected in Figure 5.5b can be attributed to one of these particle mixing mechanisms. Figure 5.5c shows the particle velocity divergence superposed over the particle velocity vectors. It indicates that particle-flows are compressed and entrained into the wake region of bubbles, whereas they tend to expand at the region near the top of bubbles. In the context of the TFM, this is due to the compressibility of the particle phase.

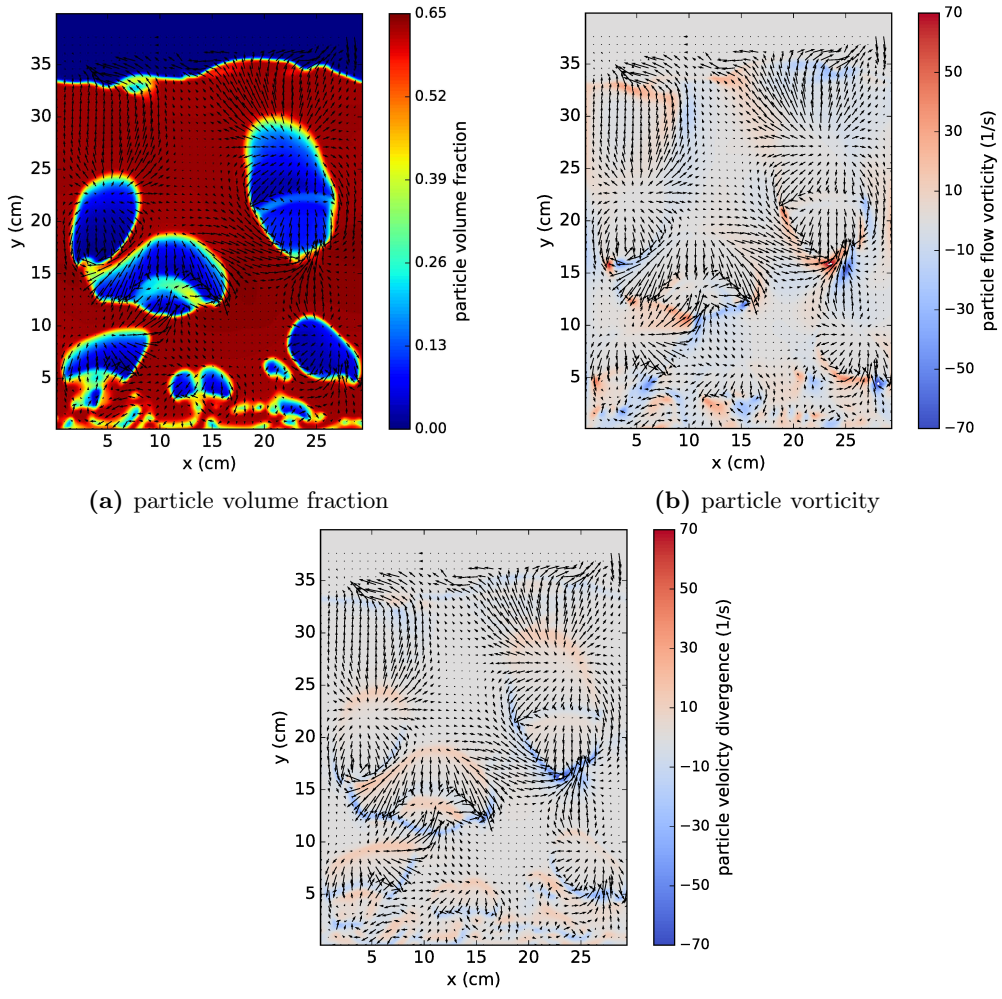

(a) particle volume fraction

(b) particle vorticity

(c) particle velocity divergence

Figure 5.5: Instantaneous (a) particle volume fraction (b) particle vorticity (c) particle divergence, superposed over the particle velocity field at $t = 85$ s.

Before studying the particle vortical structures captured by 3D POD, it is helpful to look at the dominant velocity patterns predicted by the 2D POD in the same plane as in Figure 5.1. Figure 5.6 shows the first four dominant spatial POD modes corresponding to the particle meso-scale fluctuating velocity field. These modes contain 17.7%, 5.3%, 4.9%, and 4.3% of the total energy, respectively. The most energetic POD mode indicates that the meso-scale fluctuating particle velocity field is strongest in the stream-wise (axial) direction with intense velocity fluctuations at the bed surface (30 cm $< y <$ 35 cm). This is consistent with the fact that the resolved-scale particle normal Reynolds stress, i.e., $\overline{u'_y u'_y}$, is greater than the the resolved-scale particle Reynolds shear stress, i.e., $\overline{u'_y u'_x}$ (for details see [2]). The dominant feature of the second mode is the presence of axially oriented velocity vectors in the region $y >$ 20 cm. In addition, the second mode is characterized by the presence of two pairs of source and sink-like velocity patterns at the heights of approximately 35 cm and 20 cm, respectively. The contribution of the lateral particle fluctuating velocity is more significant in the next pair of POD modes such that the topology of these two modes is quite different from the first two modes due to the formation of a number of vortices. In the third mode, there exist a larger vortex and two smaller vortices of opposite sign that tend to rotate the particles. In the fourth eigenmode, the two vortices of opposite sign draw the particle-flow from the bottom and direct it towards the wall. We observe that the flow pattern of the time-averaged particle velocity field is evident in the fourth POD mode. Overall, Figure 5.6 indicates that the dominant particle meso-scale fluctuating velocity patterns (POD modes 1 and 2) are principally aligned in the axial direction, corresponding to the particles being mixing by the bubble wakes, with a significant laterally directed fluctuating velocity vectors at the bed surface, corresponding to mixing caused by the bubbles bursting.

To assess the ability of 2D POD in reconstruction of the instantaneous particle flow field from the high-energy containing modes, the instantaneous particle vorticity and velocity fields of Figure 5.5b are considered. Figure 5.7 shows the POD reconstruction of the instantaneous particle vorticity field superimposed on the velocity field with 50 and 200 eigenmodes. We recall that POD modes provide an optimal decomposition for the fluctuating particle flow field in the sense that much of the flow topology can be captured by using a small number of modes. The first 50 and 200 eigenmodes capture approximately 74% and 90% of the total fluctuating energy, respectively. Comparing Figure 5.7a and Figure 5.5b indicates that the formation of vortex motions corresponding to the larger bubble structures is reproduced by the first 50 modes. In order to reconstruct the evolution of the vortices more accurately, a reconstruction based on additional spatial modes is presented in Figure 5.7b. This figure shows that 2D POD reconstruction based on 200 modes is similar enough to the selected snapshot to conclude that first 200 POD bases, among a total of 5001 modes, are sufficient to recover the major features of the particle flow field. We note that the reconstruction of the instantaneous field by POD modes in this figure results in a relatively smoother field compared to the actual flow, as expected.

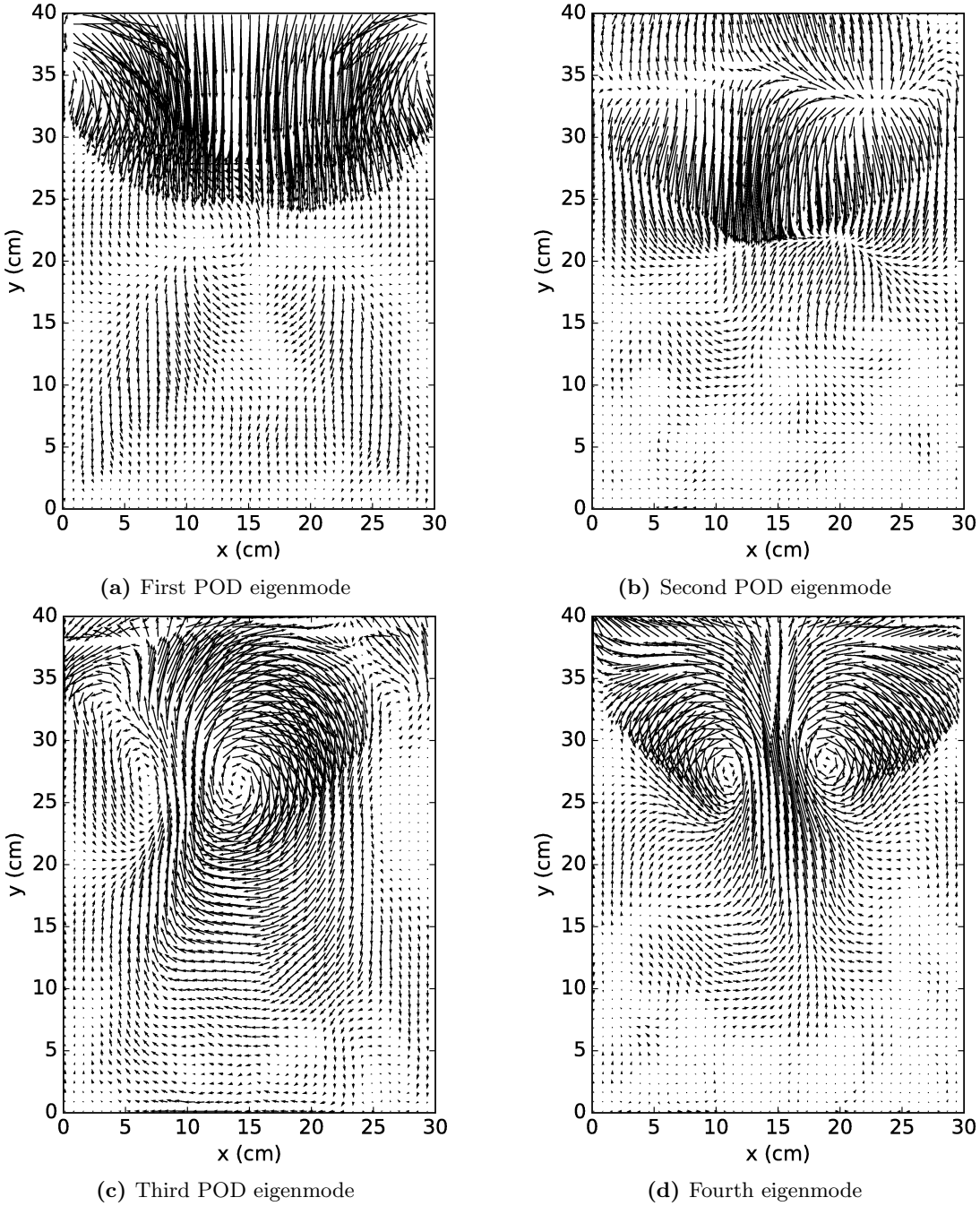

(a) First POD eigenmode

(b) Second POD eigenmode

(c) Third POD eigenmode

(d) Fourth eigenmode

Figure 5.6: The dominant four POD eigenmodes of the particle velocity field.

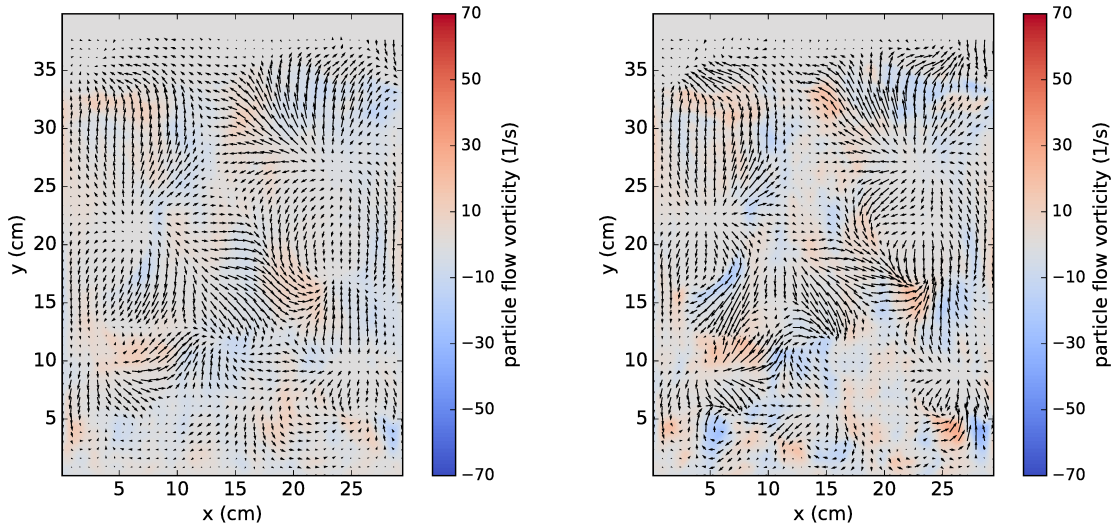

(a) reconstruction with 50 eigenmodes

(b) reconstruction with 200 eigenmodes

Figure 5.7: POD reconstruction of instantaneous particle vorticity field superimposed over the velocity field for the instantaneous field shown in Figure 5.5 using (a) 50 eigenmodes and (b) 200 eigenmodes.

5.4.4 3D POD analysis of the particle velocity field

The 3D POD was successful in capturing the dominant components of the particle meso-scale fluctuating velocity field with a small fraction of total modes as shown in Figure 5.8. The first energetic mode contains approximately 16% of the total energy, with the first 100 and 280 snapshots cumulatively capturing close to 80% and 90% of the total energy, respectively. Capturing 90% of the total energy with only 280 3D POD modes from a total of 5001 snapshots indicates the remarkable potential of POD-based ROM for predicting the essential features of a bubbling bed.

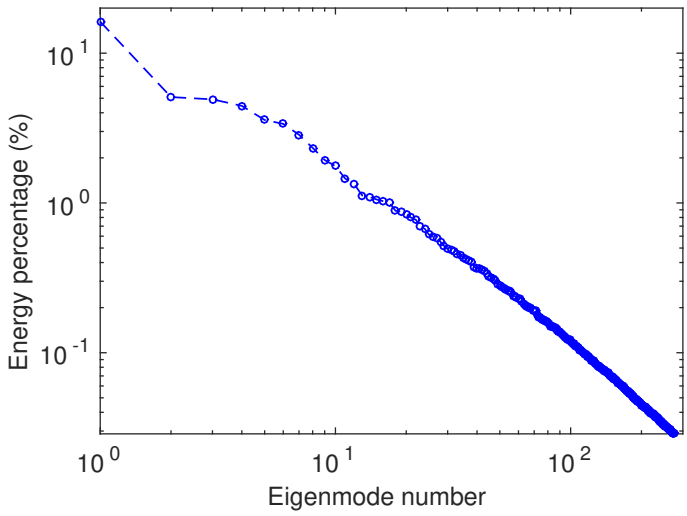

Figure 5.8: 3D POD energy distribution.

Figure 5.9 shows the particle vortical structures corresponding to the first four dominant POD eigenmodes as captured by the swirling strength criterion. There exist smaller ring-like vortex sheets in the lower part of the bed for all four modes. Also, all four modes show the formation of larger ribbon-like structures in the middle of the bed (10 cm $< y <$ 30 cm). Comparing Figures 5.6 and 5.9 indicates that these large ring-like structures in general correspond to the vortical motions in the first four planar POD modes, as shown in Figure 5.6. For example, the two large closed ribbon-structures in the region of 20 cm $< y <$ 30 cm in Figure 5.9d are associated with the two vortices of opposite sign in Figure 5.6d. The laterally oriented vortex sheet at the bed surface in the first eigenmode can be attributed to the bubble burst, as discussed above, directing particles transversely from an axially oriented flow towards the side walls. Overall, Figure 5.9 represents a set of dominant vortex filaments associated with the particle meso-scale velocity fluctuations that strongly contribute to the particle mixing in the bed. In this regard, the particle flow field in the bed can be characterized as a tangle of vortical structures that evolve in time, interact with one another, couple to the background gas phase, and govern the bed dynamics.

One striking feature of the vortex filaments shown in Figure 5.9 is their ribbon-like structure. This observation is unlike that observed in single-phase turbulent flows, where the dominant vortical structures are tubular. The presence of ribbon-like structures have also been observed in single-phase turbulent flow; see for example Moisy and Jimenez [110] and Orlandi [111]. In single-phase turbulent flows, it is believed that unstable ribbon-like vortex sheets appear at first and then roll up, due to shear instabilities, to form stable tubular structures [111, 112]. Orlandi [111] also concluded that, in single-phase turbulent flows, ribbon-like structures are generated due to inviscid interaction of vortical structures and indicated that, for inviscid turbulent flows, ribbon-like structures dominate over the tubular ones. We note that, in single-phase flows, the instabilities due to the interaction of viscous terms and nonlinear convective terms give rise to turbulence and hence vortical structures. Therefore, it may also be helpful to review the instabilities in particle systems to gain a deeper insight into the particle vortical structures. Fullmer and Hrenya [113] investigated the mechanisms that result in clustering, with an emphasis on kinetic theory-based continuum models. They critically reviewed the validation studies of kinetic theory-based models to explore their accuracy and limitations. Garzó [114] performed a linear stability analysis of the hydrodynamic equations for a granular (no interstitial fluid) system and showed that the instability is often driven by the transversal shear mode, i.e., velocity vortex instability. Mitrano et al. [115] determined the critical length scales, analogous to the critical Reynolds number in single-phase turbulent flows, associated with the onset of vortices and cluster instabilities. They demonstrated that the particle velocity vortex instability temporally precedes a clustering instability. Yin et al. [116] were the first to report particle velocity vortex instabilities in gas-particle systems. They observed instabilities similar to those previously observed in their granular (no fluid) counterparts. In bubbling beds, the bubble structures arise due to the collective effect of various types of instabilities occurring in the particulate phase [52]. Therefore, similar to single-phase turbulent flows, the appearance of ribbon-like vortex structures in Figure 5.9 may be attributed to the instabilities in the particle

phase that result in bubble formation. However, unlike single-phase turbulent flows, it appears that these flat vortex sheets are stable structures in bubbling beds. We note that in single-phase turbulent flows, the larger vortices break up into smaller vortices, and then into even smaller vortices. This continuous process whereby larger vortices break down to generate smaller vortices, which is due to shear instabilities, corresponds to the energy cascade from larger to smaller structures. However, in bubbling beds there is no continuous energy cascade from larger to smaller scales, i.e., the particle phase does not exhibit this characteristic of canonical turbulence.

Figure 5.10 shows the instantaneous particle vortical structures at $t = 85$ s and its 3D POD reconstruction based on 150 and 300 eigenmodes, capturing approximately 85% and 90% of the total energy, respectively. Figure 5.10b indicates that the reconstruction based on the first 150 POD modes has captured the dominant features of the instantaneous field. Addition of higher-order modes, as shown in Figure 5.10c, adds details but mostly to the previously captured structures reconstructed from 150 modes.

5.5 Conclusions

The particle flow fields, i.e., particle volume fraction and velocity fields, inside a bubbling bed exhibit strong unsteady flow patterns accompanied by intense meso-scale fluctuations induced by the motion of bubbles. State-of-the-art post-processing methodologies namely, POD and the swirling strength criterion, were applied to the particle flow fields predicted by a TFM of a bubbling bed to identify and analyze the dominant spatio-temporal patterns of the particulate phase. To the best of our knowledge, this is the first time that 3D POD was used to quantitatively explore the meso-scale fluctuating particle fields. Also, for the first time, the particle vortical structures in a bubbling bed were identified using the swirling strength criterion applied to the particle velocity gradient tensor.

3D POD analysis of the particle volume fraction fluctuation field indicated an approximate reflective symmetry in both the zeroth POD mode (time-averaged particle volume fraction field) and the first POD mode, even though none of the instantaneous snapshots were symmetric. It was observed that the dominant fluctuations in the particle volume fraction occur in the upper part of the bed, where the larger bubble structures form, and also at the bed surface where the bubbles burst. Although the variation of the POD temporal coefficients associated with the particle volume fraction field implied periodicity in the flow, their power spectral density did not show a well-defined dominant frequency, indicating the presence of an irregular periodicity in the flow. The temporal coefficient were used to plot the phase-space projections. Their relative closed nature suggested the presence of a low-dimensional attractor.

It was determined that the instantaneous particle flow is characterized by the formation of high vorticity regions in the vicinity of the bubble boundaries with a relatively higher vorticity magnitude in the wake regions of the bubbles. The dominant particle meso-scale fluctuating velocity patterns (i.e., the first two most energetic POD modes) are principally aligned in the axial direction, corresponding to the particle mixing by

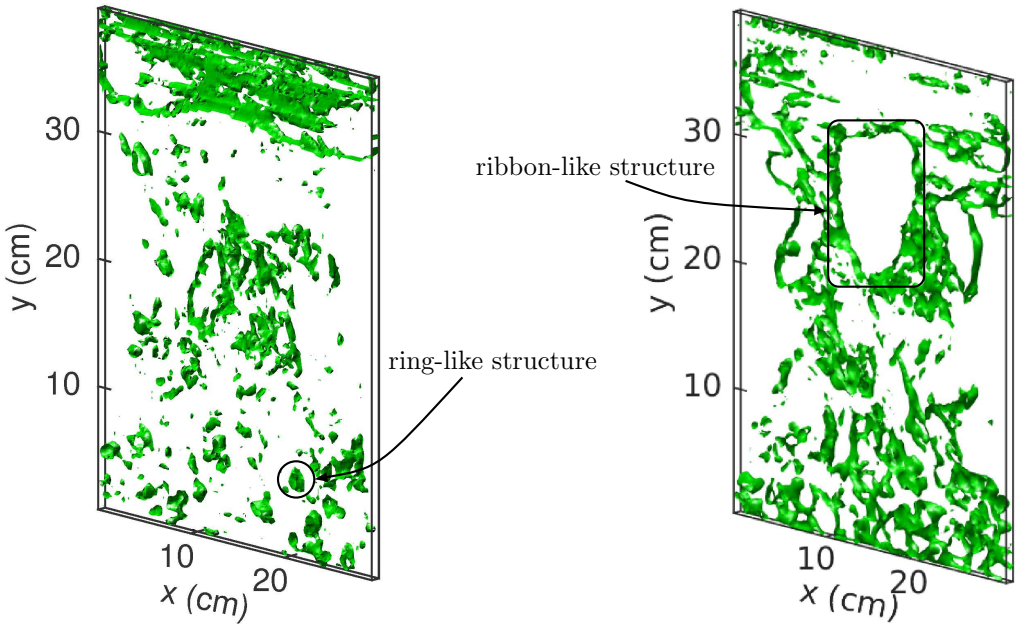

(a) First eigenmode

(b) Second eigenmode

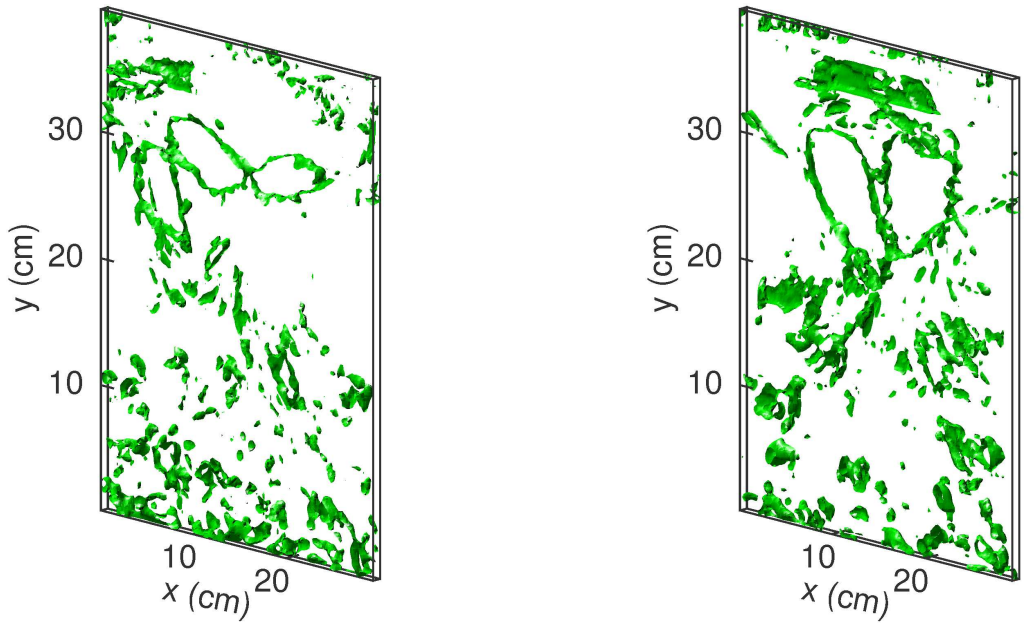

(c) Third eigenmode

(d) Fourth eigenmode

Figure 5.9: Particle vortical structures of: (a) first POD eigenmode, (b) second POD eigenmode, (c) third POD eigenmode, (d) fourth POD eigenmode, represented by iso-surfaces of $\lambda_{ci} = 30, 35, 40$ and 50, respectively.

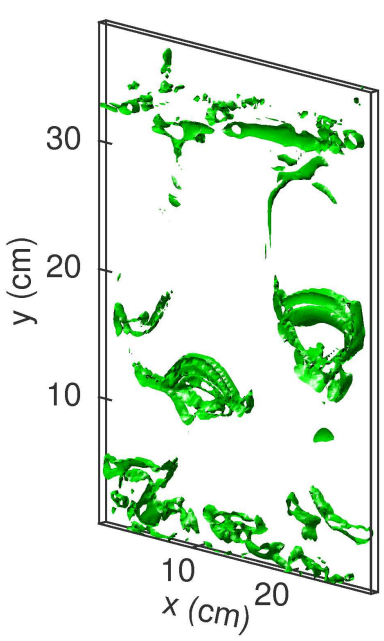

(a) Instantaneous vortical structures

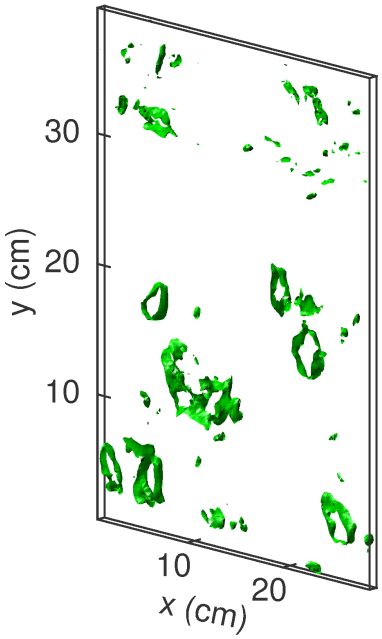

(b) POD reconstruction with 150 eigenmodes

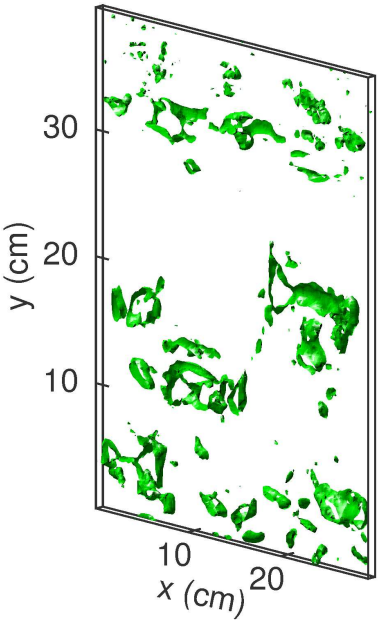

(c) POD reconstruction with 300 eigenmodes

Figure 5.10: (a) Instantaneous vortex structures at $t = 85$ s and $\lambda_{ci} = 30$; 3D POD reconstruction of the instantaneous structures with (b) 150 eigenmodes and (c) 300 eigenmodes using iso-surfaces of $\lambda_{ci} = 10$.

the bubble wakes, with a laterally directed fluctuating velocity vectors at the bed surface, corresponding to the mixing caused by the bubbles bursting. Applying the swirling strength criterion revealed the existence of smaller ring-like vortex sheets in the lower part of the bed, larger ribbon-like structures in the middle of the bed, and a laterally oriented vortex sheet at the bed surface. It was observed that the main characteristic feature of the particle vortical motions was their flat structure. The flat vortex sheets appear to be stable structures in bubbling beds, in stark contrast to the case of single-phase turbulent flows, that emerge due to the collective effect of instabilities occurring in the particulate phase.

A 3D POD was used to obtain a reduced-order reconstruction of the particle velocity and volume fraction fields using a subset of the high-energy containing modes. The ability of the POD eigenmodes to reproduce these instantaneous fields was systematically assessed.

Acknowledgement

The authors are grateful to the Natural Sciences and Engineering Research Council of Canada (NSERC) for providing financial assistance for this research project.

Chapter 6

Concluding remarks

6.1 Summary

Fluidized beds are widely employed in the energy, chemical, power-generation, and agricultural industries for processes involving drying, separation and mixing of particles, and chemical reactions [6]. Gas-particle fluidized beds have the distinct advantage of creating a highly suitable medium for heat and mass transfer and rapid mixing of particles. In order to be able to effectively design fluidized beds at the industrial scale, it is essential to have an understanding of the complex hydrodynamic behavior of the dense gas-particle flows inside them. This understanding is achieved through theoretical and numerical models and data collected from physical experiments.

The experimental study of inherently 3D flows inside fluidized beds can be difficult and costly in terms of flow visualization and measurements. However, advanced computational models that provide realistic predictions of the gas-particle flows could be used to provide similar information. Numerical simulations enable us to not only conduct a virtual experiment of the actual fluidized bed but also make detailed localized measurements that would be almost impossible in a physical experiment. The results of such numerical simulations are used to visualize the unsteady and complex motions that occur inside the fluidized bed. In this thesis the Eulerian–Eulerian TFM, based on the locally averaged equations derived by Anderson and Jackson [7], was used to simulate dense gas-particle flows inside two different 3D bubbling beds. The numerical code Multiphase Flow with Interphase eXchanges (MFIX) [11] was used to perform the simulations, using the Eulerian–Eulerian framework. Some additional FORTRAN subroutines were developed and integrated into the MFIX code to implement the particle-wall boundary conditions of Jenkins and Louge [72] and Schneiderbauer et al. [73]. The numerical model predicts such output properties as the particle volume fraction, gas pressure, the velocity components of each phase, and the granular temperature of the particle phase. Python subroutines were developed to post-process these properties and calculate spatially and time-averaged quantities of interest, such as the phasic velocity profiles, particle-flow patterns, 3D bubble characteristics, power spectral density of the gas pressure, and resolved-scale particle Reynolds stresses. Special Python subroutines were also developed to perform the energy budget analysis, POD analysis, and to identify the particle vortex motions using the swirling strength method. Extensive 3D simulations were performed to obtain the model parameter values that yielded the most comparable results with the experimental data. All simulations were

performed in parallel using 60 cores on an architecture consisting of dual Hex Core Intel Xeon X5650 2.66 GHz with 12 GB of RAM each and running Red Hat Enterprise Linux Server 5.7.

6.2 Conclusions and contributions

The first study case, Chapter 2, reports an in-depth study of two different models for the particle stress tensor in the elastic-inertial regime and assesses their ability to predict the hydrodynamics of a 3D cylindrical fluidized bed. Overall, this study demonstrated the significant role of the particle stress tensor in the prediction of dense gas-particle flows using a two-fluid model. A major objective was to gain insight into how these models modify the simulated flow behavior. To this end, a dimensionless inertial number was used to identify different flow regimes corresponding to different particle stress behaviors. It appears that this was the first time that contours of inertial number were used to visualize the flow properties. Analysis of the flow properties for a range of gas-particle regimes based on the inertial number enhances our insight into the flow behavior in such a complex multiphase system. The study quantitatively explained some important features of the mechanics of bubbling/slugging beds that have received relatively little attention in the literature. For example, the effects of two different stress models on the circulation patterns, velocity profiles, bubble characteristics, natural frequency of the bed, and "resolved-scale" particle Reynolds stress were investigated in detail. The results using the Princeton stress model were found to be closer to the experimental data for the axial particle velocity and flow circulation pattern than those based on the Schaeffer model. This was due to the fact that, unlike the Schaeffer model, the Princeton model differentiates between the rapid-flow regime and the intermediate elastic-inertia regime and applies different constitutive equations for each regime. Comparing the results of the two stress models indicated that the Schaeffer model predicted a larger particle Reynolds stress; this behavior was attributed to the prediction of more vigorous bubbles. We also note that the use of the Princeton model results in a faster algorithm that is less prone to divergence. Finally, the Schaeffer model was found to predict a higher level for the granular temperature that was explained on the basis of the enhanced level of the net production term in the transport equation.

In Chapter 3, a comprehensive study was performed to assess the effect of three different wall BCs on the structural characteristics of a dense gas-particle flow inside a 3D thin bubbling bed. The wall BCs considered in this study included the Johnson–Jackson model [25], the Jenkins–Louge model [72], and the model of Schneiderbauer et al. [73]. The results using the Jenkins–Louge model were found to be closer to the experimental data for the axial particle velocity and flow circulation pattern than those based on the models of Johnson–Jackson and Schneiderbauer et al. Although the difference in other flow characteristics predicted by the Jenkins–Louge and the Schneiderbauer et al. models were insignificant, it appeared that the Jenkins–Louge model required slightly less computational time to obtain results comparable to the measured data within the same time-averaging window. Overall, the flows predicted by all three wall models were structurally similar. However, some specific features differed in a systematic way that were tracked to the

effect of wall boundary condition on the bubble behavior. For example, the flow characteristics predicted by the Johnson–Jackson BC were in some ways different from those predicted by the other two models. The reason was attributed to the more vigorous bubbles predicted by the Johnson–Jackson wall model. The more energetic bubbles resulted in a lower level of granular temperature, a less-expanded bed, and more extensive mixing regions inside the bed. It was also found that in bubbling beds the mixing caused by the normal particle Reynolds stress is much stronger than the one caused by the shear particle Reynolds stress.

In Chapter 4, an in-depth systematic study that used a particle energy budget analysis was performed to investigate the dynamics of a 3D bubbling bed. An equation for the kinetic energy of the mean particle flow was rigorously derived in the context of the TFM approach, and the physical implications of the terms involved were discussed. The time-averaged spatial distribution of different terms appearing in the energy equation was visualized. The results of the energy analysis indicate that the mean particle-flow gains its kinetic energy from the mean kinetic energy of the gas phase through large-scale gas pressure gradient and drag terms. It was found that the role of each term was equally significant in the exchange of mean kinetic energy between the two phases which occurs in the central region of the bed. The conversion of particle fluctuating energy into internal energy of the gas phase was estimated to be negligible. The contributions to the energy cascade of both kinetic-collisional and frictional stresses were found to be comparable. The kinetic-collisional stress extracts mean kinetic energy to produce granular energy, whereas the frictional stress dissipates it into heat. It was also observed that the kinetic-collisional part of the particle pressure contributes substantially to the production of fluctuating energy by extracting energy from the mean particle-flow. It was determined that, among the terms involved in the energy cascade process, the minimum contribution corresponds to the production of granular energy due to the slip velocity between the two phases. It was observed that highly dense flow in the near-wall region did not contribute much to the energy cascade, and its role was limited to the conversion of particle mean kinetic energy to potential energy. In addition to the energy cascade that happens through particle-particle and particle-gas interactions, the energy cascade that occurs at the physical walls due to the wall-particle interaction was investigated. In this regard, three different wall boundary conditions for the particulate phase that account for the particle slip-velocity and the granular energy flux at the wall were assessed, and the wall contribution to the dissipation of mean particle kinetic energy and random particle fluctuating energy predicted by each BC was determined. The energy budget predicted by the Johnson–Jackson BC substantially diverges from those predicted by the other two wall BCs. For example, the wall contribution to the total dissipation of particle mean kinetic energy was found to be 36.8%, 8.2%, and 8.0% as predicted by the BCs of Johnson and Jackson, Jenkins and Louge, and Schneiderbauer et al., respectively. For the Johnson–Jackson BC, the contributions of both wall collisional and frictional stresses to the dissipation of the mean kinetic energy were highly overestimated. It was also found that the source terms, e.g., dissipation and production contributions, in the granular energy equation played a more significant role in the energy cascade compared to the convective and diffusive terms. The overall net granular energy (equal to net transport) produced inside the bed corresponding to the BCs

of Johnson–Jackson, Jenkins–Louge, and Schneiderbauer et al. were −1.21 kJ, −0.06 kJ, and −0.14 kJ, respectively. This indicates that on average the flow inside the bed as predicted by the Jenkins–Louge BC tends more toward local equilibrium than the flows predicted by the other two BCs.

In Chapter 5, state-of-the-art post-processing methodologies namely, POD and the swirling strength criterion were applied to the particle flow fields predicted by the TFM of the thin bubbling bed, discussed in Chapters 3 and 4, to identify and analyze the dominant spatio-temporal patterns of the particulate phase. To the best of our knowledge, this was the first time that 3D POD was used to quantitatively explore the meso-scale fluctuating particle flow fields. Also, for the first time, the particle vortical structures in a bubbling bed were identified using a swirling strength criterion applied to the particle velocity gradient tensor. 3D POD analysis of the particle volume fraction fluctuation field indicated an approximate reflective symmetry in both the zeroth POD mode (time-averaged particle volume fraction field) and the first POD mode, even though none of the instantaneous snapshots were symmetric. It was observed that the dominant fluctuations in the particle volume fraction occur in the upper part of the bed, where the larger bubble structures form, and also at the bed surface where the bubbles burst. Although the variation of the POD temporal coefficients associated with the particle volume fraction field implied periodicity in the flow, their power spectral density did not show a well-defined dominant frequency, indicating the presence of an irregular periodicity in the flow. The temporal coefficient were used to plot the phase-space projections. Their relative closed nature was attributed to the presence of a low-dimensional attractor. It was determined that the instantaneous particle flow is characterized by the formation of high vorticity regions in the vicinity of the bubble boundaries with a relatively higher vorticity magnitude in the wake region of bubbles. The dominant particle meso-scale fluctuating velocity patterns (first two energetic POD modes) are principally aligned in the axial direction, corresponding to the particle mixing by the bubble wakes, with laterally directed fluctuating velocity vectors at the bed surface, corresponding to mixing caused by the bubble bursting. Applying the swirling strength criterion revealed the existence of smaller ring-like vortex sheets in the lower part of the bed, larger ribbon-like structures in the middle of the bed, and a laterally-oriented vortex sheet at the bed surface. It was observed that a significant characteristic feature of the particle vortical motions was their flat structure. The flat vortex sheets appear to be stable structures in bubbling beds, unlike the case of single-phase turbulent flows, that emerge due to the collective effect of instabilities occurring in the particulate phase. 3D POD was used to obtain a reduced-order reconstruction of the particle velocity and volume fraction fields using a subset of the high-energy containing modes. The ability of the POD eigenmodes to reproduce these instantaneous fields was systematically assessed.

6.3 Future work

Looking forward, the results of Chapter 2 indicate that a particle stress model that uses an inertial number dependent rheology would be an especially promising approach for predicting the flow dynamics in bubbling

fluidized beds. Developing a particle stress model that is dependent on inertial number is still an ongoing research area. In this regard, Chialvo et al. [117] investigated the rheology of granular materials via molecular dynamics simulations of homogeneous, simple shear flows of soft, frictional spheres. They proposed a rheological model that blends the asymptotic relations in the three regimes, i.e., the rapid-flow, quasi-static and elastic-inertial regimes, to obtain a general description for these flows. Therefore, it is suggested to implement this particle stress model into the MFIX code and investigate its effect on the prediction of the bed dynamics.

Another important undertaking as an extension to this study is to perform an energy budget analysis on a moderately dense gas-particle flow in a circulating fluidized bed (CFB). The energy analysis performed in Chapter 4 dealt with a dense gas-particle flow inside a bubbling bed, where the effect of frictional stress is significant and the turbulence in the gas phase, if any, is damped by the inertia of particles. In gas-particle flows inside CFBs, in addition to the gas phase, the particulate phase might show turbulent behavior. The fluctuating kinetic energy associated with the organized motion of collections of particles was appreciated in the work of Dasgupta, Jackson, and Sundaresa [118]. The inertial instability in the particle phase can occur in a shear flow of a granular material [119], in the absence of any interstitial fluid, resulting in organized motion of collections of particles. Similar behavior was observed in the computer simulation of granular flows performed by Hopkins and Louge [120]. They observed that packets of particles traveled randomly and formed and broke up in a continuous manner, reminiscent of the motion of the eddies in single-phase turbulent flows. Consequently, a comprehensive model would be "turbulent gas-turbulent particle" in nature to allow for generation and dissipation of turbulence kinetic energy in both phases and exchange of this energy between them [118]. Dasgupta et al. [118] and Hrenya and Sinclair [121] were the first to model the effect of collective motion of particle packets in a dense gas-particle flow in a fully developed vertical pipe. In a seminal study, Fox [92] rigorously derived a Reynolds-average turbulence model for collisional fluid-particle flows. It is suggested to consider a turbulent gas-particle flow inside a CFB and perform an energy budget analysis to quantitatively determine the significance of various terms contributing to the energy cascade (or exchange) in CFBs.

Finally, another effort that would constitute advancement to this research is to perform a 3D POD on a gas-particle flow inside a CFB. It is important to identify and analyze the dominant spatio-temporal patterns in a CFB, where the effect of turbulence in both phase is significant. Moreover, it was observed in Chapter 5 that the particle vortical motions in bubbling beds are typically flat structures. However, in CFBs the particulate phase is expected to show turbulent behavior. Therefore, in CFBs the stable particle vortical structures might not be flat.

References

[1] W. Goossens, "Classification of fluidized particles by Archimedes number," *Powder Technol.*, vol. 98, pp. 48–53, 1998.

[2] M. R. Haghgoo, D. J. Bergstrom, and R. J. Spiteri, "A comprehensive assessment of different wall boundary conditions on the simulation of bubbling fluidized beds," *Int. J. Multiphase Flow*, vol. 99, pp. 500–511, 2018.

[3] D. Geldart, "Types of gas fluidization," *Powder Technol.*, vol. 7, pp. 285–292, 1973.

[4] L. Glicksman, "Scaling relationships for fluidized beds," *Chem. Eng. Sci.*, vol. 39, pp. 1373–1379, 1984.

[5] L. Glicksman, M. Hyre, and K. woloshun, "Simplified scaling relationships for fluidized beds," *Powder Technol.*, vol. 77, pp. 177–199, 1993.

[6] D. Kunii and O. Levenspiel, *Fluidization engineering (2nd edition).* Newton, MA: Butterworth-Heinemann, Inc., 1991.

[7] T. Anderson and R. Jackson, "A fluid mechanical description of fluidized beds. equations of motion," *Ind. Eng. Chem. Fundam.*, vol. 6, pp. 527–539, 1967.

[8] M. Ishii, *Thermo-fluid dynamic theory of two-Phase flow.* Direction des Etudes et Recherches dElectricite de France, Eyrolles, Paris, 1975.

[9] D. Drew, "Averaged field equations for two-phase media," *Stud. Appl. Math.*, vol. 50, pp. 133–166, 1971.

[10] D. Zhang and A. Prosperetti, "Averaged equations for inviscid disperse two-phase flow," *J. Fluid Mech.*, vol. 267, pp. 185–219, 1994.

[11] M. Syamlal, W. Rogers, and T. J. O'Brien, "MFIX documentation: Theory guide," Technical Note DOE/METC-94/1004,, Morgantown Energy Technology Centre, 1993.

[12] H. Enwald, E. Peirano, and A. E. Almstedt, "Eulerian two-phase flow theory applied to fluidization," *Int. J. Multiphase Flow*, vol. 22, pp. 21–66, 1996.

[13] M. J. V. Goldschmidt, R. Beetstra, and J. A. M. Kuipers, "Hydrodynamic modelling of dense gas-fluidised beds: comparison and validation of 3D discrete particle and continuum models," *Powder Technol.*, vol. 142, pp. 23–47, 2004.

[14] M. Chiesa, V. Mathiesen, J. A. Melheim, and B. Halvorsen, "Numerical simulation of particulate flow by the Eulerian–lagrangian and the Eulerian–Eulerian approach with application to a fluidized bed," *Comput. Chem. Eng.*, vol. 29, pp. 291–304, 2005.

[15] T. Li and Y. Zhang, "A new model for two-dimensional numerical simulation of pseudo-2D gas-solids fluidized beds," *Chem. Eng. Sci.*, vol. 102, pp. 246–256, 2013.

[16] S. Cloete, A. Zaabout, S. T. Johansen, M. van Sint Annaland, F. Gallucci, and S. Amini, "The generality of the standard 2D TFM approach in predicting bubbling fluidized bed hydrodynamics," *Powder Technol.*, vol. 235, pp. 735–746, 2013.

[17] F. Hernandez-Jimenez, S. Sanchez-Delgado, A. Gomez-Garcia, and A. Acosta-Iborra, "Comparison between two-fluid model simulations and particle image analysis and velocimetry (PIV) results for a two-dimensional gas solid fluidized bed," *Chem. Eng. Sci.*, vol. 66, pp. 3753–3772, 2011.

[18] N. Xie, F. Battaglia, and S. Pannala, "Effects of using two- versus three-dimensional computational modeling of fluidized beds: Part II, budget analysis," *Powder Technol.*, vol. 182, pp. 14–24, 2008.

[19] T. Asegehegn, M. Schreiber, and H. Krautz, "Influence of two- and three-dimensional simulations on bubble behavior in gas-solid fluidized beds with and without immersed horizontal tubes," *Powder Technol.*, vol. 219, pp. 9–19, 2008.

[20] M. R. Haghgoo, D. J. Bergstrom, and R. J. Spiteri, "Effect of particle stress tensor in simulations of dense gas-particle flows in fluidized beds," *Particuology, http://dx.doi.org/10.1016/j.partic.2017.04.010*, p. (to appear), 2017.

[21] M. R. Haghgoo, D. J. Bergstrom, and R. J. Spiteri, "Energy budget analysis of a dense gas-particle flow inside a fluidized bed," *Powder Technol., Under Review*, 2018.

[22] C. K. K. Lun, S. B. Savage, D. J. Jeffrey, and N. Chepurniy, "Kinetic theories for granular flow: inelastic particles in couette flow and slightly inelastic particles in a general flow field," *J. Fluid. Mech.*, vol. 140, pp. 223–256, 1984.

[23] S. Savage, "The mechanics of rapid granular flows," *Adv. Appl. Mech.*, vol. 24, pp. 289–366, 1984.

[24] B. Van Wachem, J. C. Schouten, C. M. van den Bleek, R. Krishna, and J. L. Sinclair, "Comparative analysis of CFD models of dense gas-solid systems," *AIChE J.*, vol. 47, pp. 1035–1051, 2001.

[25] P. C. Johnson and R. Jackson, "Frictional-collisional constitutive relations for granular materials with application to plane shearing," *J. Fluid Mech.*, vol. 176, pp. 67–93, 1987.

[26] A. Srivastava and S. Sundaresan, "Analysis of a frictional-kinetic model for gas-particle flow," *Powder Technol.*, vol. 129, pp. 72–85, 2003.

[27] D. G. Schaeffer, "Instability in the evolution equations describing incompressible granular flow," *J. Differ. Equations*, vol. 66, pp. 61–74, 1987.

[28] Y. Makkawi, P. Wright, and R. Ocone, "The effect of friction and inter-particle cohesive forces on the hydrodynamics of gas-solid flow: a comparative analysis of theoretical predictions and experiments," *Powder Technol.*, vol. 163, pp. 69–79, 2006.

[29] C. Campbell, "Granular shear flows at the elastic limit," *J. Fluid Mech.*, vol. 465, pp. 261–291, 2002.

[30] S. Schneiderbauer, A. Aigner, and S. Pirker, "A comprehensive frictional-kinetic model for gas-particle flows: Analysis of fluidized and moving bed regimes," *Chem. Eng. Sci.*, vol. 80, pp. 279–292, 2012.

[31] S. Benyahia, "Validation study of two continuum granular frictional flow theories," *Ind. Eng. Chem. Res.*, vol. 47, pp. 8926–8932, 2008.

[32] A. Passalacqua and L. Marmo, "A critical comparison of frictional stress models applied to the simulation of bubbling fluidized beds," *Chem. Eng. Sci.*, vol. 160, pp. 2795–2806, 2009.

[33] N. Reuge, L. Cadoret, C. Coufort-Saudejaud, S. Pannala, M. Syamlal, and B. Caussat, "Multifluid Eulerian modeling of dense gas-solids fluidized bed hydrodynamics: Influence of the dissipation parameters," *Chem. Eng. Sci.*, vol. 63, pp. 5540–5551, 2008.

[34] V. Verma, N. G. Deen, J. T. Padding, and J. A. M. Kuipers, "Two-fluid modeling of three-dimensional cylindrical gas-solid fluidized beds using the kinetic theory of granular flow," *Chem. Eng. Sci.*, vol. 102, pp. 227–245, 2013.

[35] J. Laverman, X. Fan, A. Ingram, M. van Sint Annaland, D. J. Parker, J. Seville, and J. Kuipers, "Experimental study on the influence of bed material on the scaling of solids circulation patterns in 3D bubbling gas-solid fluidized beds of glass and polyethylene using positron emission particle tracking," *Powder Technol.*, vol. 224, pp. 297–305, 2012.

[36] R. Beetstra, M. van der Hoef, and J. A. M. Kuipers, "Drag force of intermediate Reynolds number flow past mono- and bidisperse arrays of spheres," *AIChE J.*, vol. 53, pp. 489–501, 2007.

[37] D. Ma and G. Ahmadi, "A kinetic model for rapid granular flows of nearly elastic particles including interstitial fluid effects," *Powder Technol.*, vol. 56, pp. 191–207, 1988.

[38] D. Rangarajan, J. S. Curtis, S. Benyahia, and A. Mychkovsky, "Continuum model validation of gas jet plume injection into a gas-solid bubbling fluidized bed," *AIChE J.*, vol. 59, pp. 3247–3264, 2013.

[39] R. Ocone, S. Sundaresan, and R. Jackson, "Gas-particle flow in a duct of arbitrary inclination with particle-particle interactions," *AIChE J.*, vol. 39, pp. 1261–1271, 1993.

[40] D. Rangarajan, T. Shiozawa, Y. Shen, A. Yu, and J. Curtis, "Influence of operating parameters on raceway properties in a blast furnace using a two-fluid model," *I&EC Research*, vol. 53, pp. 4983–4990, 2014.

[41] A. Passalacqua and R. Fox, "Implementation of an iterative solution procedure for multi-fluid gas-particle flow models on unstructured grids," *Powder Technol.*, vol. 213, pp. 174–187, 2011.

[42] V. Vikas, C. Yuan, Z. Wang, and R. Fox, "Modeling of bubble-column flows with quadrature-based moment methods," *Chem. Eng. Sci.*, vol. 66, pp. 3058–3070, 2011.

[43] L. Huilin, H. Yurong, and D. Gidaspow, "Hydrodynamic modelling of binary mixture in a gas bubbling fluidized bed using the kinetic theory of granular flow," *Chem. Eng. Sci.*, vol. 58, pp. 1197–1205, 2003.

[44] N. Carnahan and K. Starling, "Equation of state for nonattracting rigid shperes," *J. Chem. Phys.*, vol. 51, pp. 635–636, 1969.

[45] T. Li, B. Grace, and X. Bi, "Study of wall boundary condition in numerical simulations of bubbling fluidized beds," *Powder Technol.*, vol. 203, pp. 447–457, 2010.

[46] C. Altantzis, R. Bates, and A. Ghoniem, "3D Eulerian modeling of thin rectangular gas-solid fluidized beds: Estimation of the specularity coefficient and its effects on bubbling dynamics and circulation times," *Powder Technol.*, vol. 270, pp. 256–270, 2015.

[47] A. Bakshi, C. Altantzis, R. Bates, and A. Ghoniem, "Eulerian-Eulerian simulation of dense solid-gas cylindrical fluidized beds: Impact of wall boundary condition and drag model on fluidization," *Powder Technol.*, vol. 277, pp. 47–62, 2015.

[48] T. Li and S. Benyahia, "Evaluation of wall boundary condition parameters for gas-solid fluidized bed simulations," *AIChE J.*, vol. 59, pp. 3624–3632, 2013.

[49] P. L. Roe, "Characteristic-based schemes for the Euler equations," *Annu. Rev. Fluid Mech.*, vol. 18, pp. 337–365, 1986.

[50] C. Guemther and M. Syamlal, "The effect of numerical diffusion on simulation of isolated bubbles in a gas-solid fluidized bed," *Powder Technol.*, vol. 116, pp. 142–154, 2001.

[51] S. Gelderbloom, D. Gidaspow, and R. Lyczkowski, "CFD simulations of bubbling/collapsing fluidized beds for three Geldart groups," *AIChE J.*, vol. 49, pp. 844–858, 2003.

[52] K. Agrawal, P. Loezos, M. Syamlal, and S. Sundaresan, "The role of meso-scale structures in rapid gas-solid flows," *J. Fluid Mech.*, vol. 445, pp. 151–185, 2001.

[53] A. Andrews IV, P. Loezos, and S. Sundaresan, "Coarse-grid simulation of gas-particle flows in vertical risers," *I&EC Research*, vol. 44, pp. 6022–6037, 2005.

[54] Y. Igci, A. Andrews IV, and S. Sundaresan, "Filtered two-fluid models for fluidized gas-particle suspensions," *AIChE J.*, vol. 54, pp. 1431–1448, 2008.

[55] J. Wang, "High-resolution Eulerian simulation of RMS of solid volume fraction fluctuation and particle clustering characteristics in a CFB riser," *Chem. Eng. Sci.*, vol. 63, pp. 3341–3347, 2008.

[56] J. Wang, "Length scale dependence of effective inter-phase slip velocity and heterogeneity in gas-solid suspensions," *Chem. Eng. Sci.*, vol. 63, pp. 2294–2298, 2008.

[57] F. da Cruz, S. Emam, M. Prochnow, J. Roux, and F. Chevoir, "Rheophysics of dense granular materials: discrete simulation of plane shear flows," *Phys. Rev. E*, vol. 72, pp. 021309:1–17, 2005.

[58] F. Taghipour, N. Ellis, and C. Wong, "Experimental and computational study of gas-solid fluidized bed hydrodynamics," *Chem. Eng. Sci.*, vol. 60, pp. 6857–6867, 2005.

[59] S. Chialvo and S. Sundaresan, "A modified kinetic theory for frictional granular flows in dense and dilute regimes," *Phys. Fluids*, vol. 25, pp. 070603:1–070603:20, 2013.

[60] A. Drescher and G. de Josselin de Jong, "Photoelastic verification of a mechanical model for the flow of a granular material," *J. Mech. Phys. Solids*, vol. 20, pp. 337–340, 1972.

[61] V. Verma, J. Padding, N. Deen, J. Kuipers, F. Barthel, M. Bieberle, M. Wagner, and U. Hampel, "Bubble dynamics in a 3-D gas-solid fluidized bed using ultrafast electron beam X-ray tomography and two-fluid model," *AIChE J.*, vol. 60, pp. 1632–1644, 2014.

[62] K. Hilligardt and J. Werther, "Local bubble gas hold-upand expansion of gas/solid fluidized beds," *Ger Chem Eng*, vol. 9, pp. 215–221, 1986.

[63] R. C. Darton, R. D. LaNauze, J. F. Davidson, and D. Harrison, "Bubble growth due to coalescence in fluidized beds," *Trans Inst Chem Eng*, vol. 55, pp. 274–280, 1977.

[64] P. Cai, M. Schiavetti, G. De Michele, G. Grazzini, and M. Miccio, "Quantitative estimation of bubble size in PFBC," *Powder Technol.*, vol. 80, pp. 99–109, 1994.

[65] A. Acosta-Iborra, C. Sobrino, F. Hernandez-Jimenez, and M. de Vega, "Experimental and computational study on the bubble behavior in a 3-D fluidized bed," *Chem. Eng. Sci.*, vol. 66, pp. 3499–3512, 2011.

[66] F. Johnsson, R. Zijerveld, J. Schouten, C. van den Bleek, and B. Leckner, "Characterization of fluidization regimes by time-series analysis of pressure fluctuations," *Int. J. Multiphase Flow*, vol. 26, pp. 663–715, 2000.

[67] D. Gidaspow, J. Jung, and R. Singh, "Hydrodynamics of fluidization using kinetic theory: an emerging paradigm: 2002 flour-daniel lecture," *Powder Technol.*, vol. 148, pp. 123–141, 2004.

[68] B. Lu, N. Zhang, W. Wang, J. Li, J. H. Chiu, and S. G. Kang, "3-D full-loop simulation of an industrial-scale circulating fluidized-bed boiler," *AIChE J.*, vol. 59, pp. 1108–1117, 2013.

[69] A. Bahramian, M. Olazar, and G. Ahmadi, "Effect of slip boundary conditions on the simulation of micro-particle velocity fields in a conical fluidized bed," *AIChE J.*, vol. 59, pp. 4502–4518, 2013.

[70] T. Li and S. Benyahia, "Revisiting Johnson and Jackson boundary condition for granular flows," *AIChE J.*, vol. 58, pp. 2058–2068, 2012.

[71] J. Jenkins, "Boundary conditions for rapid granular flows," *Appl. Mech.*, vol. 59, pp. 120–127, 1992.

[72] J. Jenkins and M. Louge, "On the flux of fluctuation energy in a collisional grain flow at a flat, frictional wall," *Phys. Fluids*, vol. 9, pp. 2835–2840, 1997.

[73] S. Schneiderbauer, D. Schellander, A. Loderer, and S. Pirker, "Non-steady state boundary conditions for collisional granular flows at flat frictional moving walls," *Int. J. Multiphase Flow*, vol. 43, pp. 149–156, 2012.

[74] Y. Zhao, Y. Zhong, Y. He, , and H. I. Schlaberg, "Boundary conditions for collisional granular flows of frictional and rotational particles at flat walls," *AIChE J.*, vol. 60, pp. 4065–4075, 2014.

[75] L. Yang, J. T. Padding, and J. A. M. Kuipers, "Partial slip boundary conditions for collisional granular flows at flat frictional walls," *AIChE J.*, vol. 63, pp. 1853–1871, 2017.

[76] P. Fede, O. Simonin, and A. Ingram, "3D numerical simulation of a lab-scale pressurized dense fluidized bed focussing on the effect of the particle-particle restitution coefficient and particle-wall boundary conditions," *Chem. Eng. Sci.*, vol. 142, pp. 215–235, 2016.

[77] Y. Igci and S. Sundaresan, "Verification of filtered two-fluid models for gas-particle flows in risers," *AIChE J.*, vol. 57, pp. 2692–2707, 2010.

[78] A. Passalacqua and R. Fox, "Advanced continuum modelling of gas-particle flows beyond the hydrodynamic limit," *Appl. Math. Modell.*, vol. 35, pp. 1616–1627, 2011.

[79] Y. Zhao, T. Ding, L. Zhu, and Y. Zhong, "A specularity coefficient model and its application to dense particulate flow simulations," *I&EC Research*, vol. 55, pp. 1439–1448, 2016.

[80] M. Louge, "Computer simulations of rapid granular flows of spheres interacting with a flat, frictional boundary," *Phys. Fluids*, vol. 6, pp. 2253–2269, 1994.

[81] A. Soleimani, S. Schneiderbauer, and S. Pirker, "A comparison for different wall-boundary conditions for kinetic theory based two-fluid models," *Int. J. Multiphase Flow*, vol. 71, pp. 94–97, 2015.

[82] J. Cloete, S. Cloete, S. Radl, and S. Amini, "Evaluation of wall friction models for riser flow," *Powder Technol.*, vol. 303, pp. 156–167, 2016.

[83] J. Laverman, I. Roghair, M. van Sint Annaland, and J. Kuipers, "Investigation into the hydrodynamics of gas-solid fluidized beds using particle image velocimetry coupled with digital image analysis," *Can. J. Chem. Eng.*, vol. 86, pp. 523–535, 2008.

[84] D. Gidaspow, *Multiphase flows and fluidization.* Academic Press, 1994.

[85] M. Syamlal, "MFIX documentation: Numerical technique," Technical Note DOE/MC31346-5824,, Morgantown Energy Technology Centre, 1998.

[86] D. B. Spalding, "Numerical computation of multi-phase fluid flow and heat transfer," *in Recent Advances in Numerical Methods in Fluids*, pp. 139–167, 1980.

[87] J. Parmentier, O. Simonin, and O. Delsart, "A numerical study of fluidization behavior of Geldart B, A/B and A particles using an Eulerian multifluid modeling approach," *In: Proc. of the 9th Int. Conference on Circulating Fluidized Beds.*, vol. Circulating Fluidized Bed Technology IX, pp. 331–336, 2008.

[88] A. Bakshi, C. Altantzis, R. B. Bates, and A. F. Ghoniem, "Multiphase-flow statistics using 3D detection and tracking algorithm (MS3DATA): methodology and application to large-scale fluidized beds," *Chem. Eng. J.*, vol. 293, pp. 335–364, 2016.

[89] K. Anderson, S. Sundaresan, and R. Jackson, "Instabilities and the formation of bubbles in fluidized beds," *J. Fluid. Mech.*, vol. 303, pp. 327–366, 1995.

[90] J. Li and J. Kuipers, "Effect of competition between particle-particle and gas-particle interactions on flow patterns in dense gas-fluidized beds," *Chem. Eng. Sci.*, vol. 62, pp. 3429–3442, 2007.

[91] J. O. Hinze, *Turbulence (second edition).* McGraw-Hill series in mechanical engineering, 1975.

[92] R. O. Fox, "On multiphase turbulenc models for collisional fluid-particle flows," *J. Fluid Mech.*, vol. 742, pp. 368–424, 2014.

[93] J. L. Lumley, *The structure of inhomogeneous turbulence.* Nauka, Moscow: In: A. M. Yaglom and V. I. Tatarski, Eds., Atmospheric Turbulence and Wave Propagation, 1967.

[94] P. G. Cizmas, A. Palacios, T. O'Brien, and M. Syamlal, "Proper-orthogonal decomposition of spatio-temporal patterns in fluidized beds," *Chem. Eng. Sci.*, vol. 58, pp. 4417–4427, 2003.

[95] A. Palacios, C. Finney, P. Cizmas, S. Daw, and T. O'Brien, "Experimental analysis and visualization of spatiotemporal patterns in spouted fluidized beds," *Chaos*, vol. 14, pp. 499–509, 2004.

[96] P. G. Cizmas, B. Richardson, T. Brennerand, T. O'Brien, M. Syamlal, and R. Breault, "Acceleration techniques for reduced-order models based on proper orthogonal decomposition," *J. Comput. Phys.*, vol. 228, pp. 7791–7812, 2008.

[97] M. Hossain, D. J. Bergstrom, and X. Chen, "Visualisation and analysis of large-scale vortex structures in three-dimensional turbulent lid-driven cavity flow," *J. Turbul.*, vol. 16, pp. 901–924, 2015.

[98] J. Hunt, A. Wary, and P. Moin, "Eddies, stream, and convergence zones in turbulent flows," cent. turbulence Res. Rep., CTR-S88:193–208., 1988.

[99] M. Chong, A. Perry, and B. Cantwell, "A general classification of three-dimensional flow fields," *Phys. Fluids*, vol. 2, pp. 765–777, 1990.

[100] J. Jeong and F. Hussain, "On the identification of a vortex," *J. Fluid Mech.*, vol. 285, pp. 69–94, 1995.

[101] J. Zhou, R. Adrian, S. Balachandar, and T. Kendall, "Mechanisms for generating coherent packets of hairpin vortices in channel flow," *J. Fluid Mech.*, vol. 387, pp. 353–396, 1999.

[102] H. Chen, R. Adrian, Q. Zhong, and X. Wang, "Analytic solutions for three dimensional swirling strength in compressible and incompressible flows," *Phys. Fluids*, vol. 26, pp. 081701:1–6, 2014.

[103] P. Chakraborty, S. Balachandar, and R. Adrian, "On the relationships between local vortex identification schemes," *J. Fluid Mech.*, vol. 535, pp. 189–214, 2005.

[104] G. Berkooz, P. Holmes, and J. Lumley, "The proper orthogonal decomposition in the analysis of turbulent flows," *Annu. Rev. Fluid Mech.*, vol. 25, pp. 539–575, 1993.

[105] P. Holmes, J. Lumley, and G. Berkooz, *Turbulence, coherent structures, dynamical systems, and symmetry.* Cambridge University Press, 1996.

[106] L. Sirovich, "Turbulence and the dynamics of coherent structures," *Quart. Appl. Math.*, vol. 5, pp. 561–590, 1987.

[107] M. Dellnitz, M. Golubitsky, and I. Melbourne, *Mechanisms of Symmetry Creation.* Birkhuser Verlag Basel: In: Bifurcation and Symmetry (E. Allgower, K. Bohmer, and M. Golubitsky eds.), 1992.

[108] P. Rowe, B. Partridge, A. Cheney, G. Henwood, and E. Lyall, "The mechanisms of solids mixing in fluidised beds," *Transact. Instit. Chem. Eng.*, vol. 43, pp. 271–286, 1965.

[109] M. Rhodes, X. Wang, M. Nguyen, P. Stewart, and K. Liffman, "Study of mixing in gas-fluidized beds using a DEM model," *Chem. Eng. Sci.*, vol. 56, pp. 2859–2866, 2001.

[110] F. Moisy and J. Jimenenz, "Geometry and clustering of intense structures in isotropic turbulence," *J. Fluid Mech.*, vol. 513, pp. 111–133, 2004.

[111] P. Orlandi, "Energy spectra power laws and structures," *J. Fluid Mech.*, vol. 623, pp. 353–374, 2009.

[112] A. Vincent and M. Meneguzzi, "The dynamics of vorticity tubes in homogeneous turbulence," *J. Fluid Mech.*, vol. 258, pp. 245–254, 1994.

[113] W. Fullmer and C. Hrenya, "The clustering instability in rapid granular and gas-solid flows," *Annu. Rev. Fluid Mech.*, vol. 49, pp. 485–510, 2017.

[114] V. Garzo, "Instabilities in a free granular fluid described by the Enskog equation," *Phys. Rev. E*, vol. 72, p. 021106, 2005.

[115] P. Mitrano, V. Garzo, A. Hilger, C. Ewasko, and C. Hrenya, "Assessing a hydrodynamic description for instabilities in highly dissipative, freely cooling granular gases," *Phys. Rev. E*, vol. 85, p. 041303, 2012.

[116] X. Yin, J. Zenk, P. Mitrano, and C. Hrenya, "Impact of collisional versus viscous dissipation on flow instabilities in gas-solid systems," *J. Fluid Mech.*, vol. 727, pp. R2:1–12, 2013.

[117] S. Chialvo, J. Sun, and S. Sundaresan, "Bridging the rheology of granular flows in three regimes," *Phys. Rev. E*, vol. 85, pp. 021305:1–8, 2012.

[118] S. Dasgupta, R. Jackson, and S. Sundaresan, "Turbulent gas-particle flow in vertical risers," *AIChE J.*, vol. 40, pp. 215–228, 1994.

[119] S. Savage, "Instability of unbounded uniform granular shear flow," *J. Fluid Mech.*, vol. 241, pp. 109–123, 1992.

[120] M. Hopkins and M. Louge, "Inelastic microstructure in rapid granular flows of smooth disks," *Phys. Fluids A*, vol. 3, pp. 47–57, 1991.

[121] C. Hrenya and J. Sinclair, "Effects of particle-phase turbulence in gas-solid flows," *AIChE J.*, vol. 43, pp. 853–869, 1997.